

Predicted and Observed Active Damping Performance  
of Macro-Micro Manipulators

by

Christopher John Van Vliet  
B.Sc., University of Alberta, 1995

A Thesis Submitted in Partial Fulfillment of the  
Requirements for the Degree of

MASTER OF APPLIED SCIENCE

in the Department of Mechanical Engineering.

We accept this thesis as conforming  
to the required standard



---

Dr. I. Sharf, Supervisor (Dept. of Mechanical Engineering)



---

Dr. R. Podhorodeski, Department Member (Dept. of Mechanical Engineering)



---

Dr. V. King, Outside Member (Dept. of Computer Science)



---

Dr. W.S. Lu, External Examiner (Dept. of Electrical and Computer Engineering)

© CHRISTOPHER JOHN VAN VLIET, 1998  
University of Victoria

All rights reserved. This thesis may not be reproduced in whole or in part, by photocopy  
or other means, without permission of the author.

Supervisor: Dr. I Sharf


# Abstract

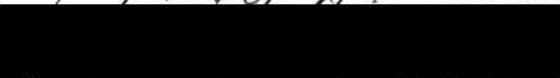
Macro-micro manipulators are used where a long, lightweight manipulator with fine end-effector control is required. The large, flexible macro-manipulator deploys the small, rigid micro-manipulator to a work site, where the fine dexterous control of the micro-manipulator is utilized to perform a specific task. Residual vibration in the macro-manipulator can be actively damped by the micro-manipulator.


Two algorithms for active damping are investigated. Each method is simulated on several simple manipulators and implemented experimentally on a macro-micro manipulator test-bed at the University of Victoria. Active damping performance is dependent not only on the choice of active damping algorithm, but also on the nominal micro-manipulator configuration. Three tools for predicting the optimal micro-manipulator configurations are evaluated against the two active damping algorithms. Little previous research effort has been directed towards making such predictions.


The University of Victoria macro-micro manipulator was developed specifically for the active damping experiments. Design, modelling, and control details of this manipulator are presented.

Examiners:

  
Dr. I. Sharf, Supervisor (Dept. of Mechanical Engineering)

  
Dr. R. Podhorodeski, Department Member (Dept. of Mechanical Engineering)

  
Dr. V. King, Outside Member (Dept. of Computer Science)

  
Dr. W.S. Lu, External Examiner (Dept. of Electrical and Computer Engineering)

# Table of Contents

Abstract	ii
Table of Contents	iii
List of Figures	vi
List of Tables	ix
<b>1 Introduction</b>	<b>1</b>
1.1 Macro-Micro Manipulators	1
1.2 Active Damping	2
1.3 Review of Active Damping Literature	4
1.4 Thesis Organization	7
<b>2 Experimental Facility</b>	<b>8</b>
2.1 Macro-Manipulator (LAURA)	8
2.2 Micro-Manipulator (SARA)	9
2.2.1 Motors and Amplifiers	10
2.2.2 Joint Design	12
2.2.3 Geometry and Flotation	13
2.3 LAURA-SARA Manipulator Model	13
2.3.1 LAURA Manipulator	14
2.3.2 SARA Manipulator	16
2.3.3 Assembled Model	17
2.4 Frequency Domain Model Validation	20
2.4.1 Impact Experiments	20
2.4.2 Experimental Data Analysis	21
2.4.3 Predicted Frequencies	22
2.4.4 Discussion	22
2.5 Control System	24
2.5.1 Software	25
2.5.2 Instrumentation and Data Acquisition	26

<b>3</b>	<b>Active Damping Techniques</b>	<b>28</b>
3.1	General Manipulator Model for Active Damping . . . . .	28
3.2	Cartesian Space vs Joint Space Derivative Control . . . . .	30
3.3	Pseudo-Passive Energy Dissipation . . . . .	32
3.3.1	Model . . . . .	32
3.3.2	Model Reduction to Component Systems . . . . .	33
3.3.3	P-PED Joint Gains . . . . .	36
3.3.4	Implementation . . . . .	38
3.4	Impedance Matching . . . . .	41
3.4.1	Derivation . . . . .	42
3.4.2	Implementation . . . . .	45
<b>4</b>	<b>Damping Performance Prediction and Evaluation Tools</b>	<b>48</b>
4.1	Coupling Map . . . . .	49
4.1.1	Derivation . . . . .	49
4.1.2	Discussion . . . . .	52
4.2	Accelerative Damping Map . . . . .	54
4.2.1	Derivation . . . . .	55
4.2.2	Discussion . . . . .	56
4.3	Modal Inertia Map . . . . .	56
4.3.1	Concept . . . . .	56
4.3.2	Derivation . . . . .	57
4.3.3	Discussion . . . . .	58
4.4	Damping Performance Evaluation . . . . .	59
<b>5</b>	<b>Simulation Results</b>	<b>60</b>
5.1	Very Simple Manipulators . . . . .	61
5.1.1	System Models . . . . .	61
5.1.2	Damping Performance . . . . .	62
5.1.3	Performance Predictions . . . . .	65
5.2	SARA on a Single Flexible Link . . . . .	69
5.2.1	System Model . . . . .	70
5.2.2	Damping Performance . . . . .	71
5.2.3	Performance Predictions . . . . .	75
5.3	Summary . . . . .	78
<b>6</b>	<b>Experimental Results</b>	<b>80</b>
6.1	Procedure . . . . .	80
6.2	Damping Performance . . . . .	82
6.2.1	Pseudo-Passive Energy Dissipation . . . . .	83
6.2.2	Impedance Matching . . . . .	86

6.3	Performance Predictions . . . . .	88
6.3.1	Prediction Maps . . . . .	88
6.3.2	Correlations . . . . .	90
6.4	Summary . . . . .	91
<b>7</b>	<b>Conclusions</b>	<b>93</b>
	<b>References</b>	<b>97</b>
<b>A</b>	<b>SARA Mechanical Design Drawings</b>	<b>99</b>
<b>B</b>	<b>Optimal Gains for Mass-Spring-Damper Systems</b>	<b>119</b>
B.1	Introduction . . . . .	119
B.2	System Definition . . . . .	120
B.3	Optimum Gains . . . . .	120
<b>C</b>	<b>Guyan Reduction</b>	<b>122</b>
C.1	Theoretical Development . . . . .	122
C.1.1	Statics . . . . .	122
C.1.2	Dynamics . . . . .	123
C.2	LAURA-SARA Results . . . . .	124
C.2.1	First Modal Frequency . . . . .	125
C.2.2	Second Modal Frequency . . . . .	126

# List of Figures

1.1	<i>Two Examples of Macro-Micro Manipulators: Light Duty Utility Arm and SSRMS/SPDM</i> . . . . .	3
2.1	<i>University of Victoria's Experimental Macro-Micro Manipulator (LAURA-SARA)</i>	9
2.2	<i>Small Articulated Rigid Arm (SARA)</i> . . . . .	10
2.3	<i>Cutaway Views of SARA Joints</i> . . . . .	12
2.4	<i>Model of Harmonic Drive Joints</i> . . . . .	14
2.5	<i>Four Component Bodies of the SARA Model</i> . . . . .	17
2.6	<i>Complete LAURA-SARA Manipulator Model</i> . . . . .	18
2.7	<i>LAURA-SARA Manipulator Configurations for Impact Experiments</i> . . . . .	21
2.8	<i>Representative Plot of Strain Gauge Response to Impact Experiment</i> . . . . .	22
2.9	<i>Sample Data and Decaying Sinusoid Curve Fit</i> . . . . .	23
2.10	<i>Instrumentation and Control Components for the LAURA-SARA Manipulator</i>	25
3.1	<i>General Manipulator Model for Development of Active Damping Algorithms</i>	29
3.2	<i>Manipulator Reduction to Mass-Spring-Damper Component Systems for P-PED Gains Calculation</i> . . . . .	34
3.3	<i>Simple Planar Macro-Micro Manipulator for Derivation of Impedance Matching</i>	42
3.4	<i>Objective Function <math>g(\mu, \zeta)</math> for Calculating Optimum Impedance Matching Joint Gains</i> . . . . .	44
5.1	<i>Very Simple (VS) Manipulators</i> . . . . .	61
5.2	<i>Observed Damping Performance for VS Manipulators Using P-PED<sub>A</sub>, P-PED<sub>B</sub>, and Impedance Matching</i> . . . . .	63
5.3	<i>Change in Dominant (First) Modal Frequency of VS Manipulators when IM Compliance is Introduced to Micro-Manipulator</i> . . . . .	66
5.4	<i>Damping Performance Predictions for VS Manipulators Using Coupling Map, Accelerative Damping Map, and Modal Inertia Map</i> . . . . .	67
5.5	<i>Contribution of CM, ADM, MIM in Predicting the P-PED<sub>A</sub>, P-PED<sub>B</sub>, and IM Damping Performance for VS Manipulators</i> . . . . .	67
5.6	<i>Change in Shape of Dominant (First) Mode of VS Manipulators when IM Compliance is Introduced to Micro-Manipulator</i> . . . . .	69

5.7	<i>One Link plus SARA (OLS) Manipulator</i>	70
5.8	<i>Observed Damping Performance for OLS Manipulator Using P-PED<sub>A</sub></i>	72
5.9	<i>Observed Damping Performance for OLS Manipulator Using P-PED<sub>B</sub></i>	72
5.10	<i>Observed Damping Performance for OLS Manipulator Using Impedance Matching</i>	74
5.11	<i>Change in Dominant (First) Modal Frequency of OLS Manipulator when IM Compliance is Introduced to SARA</i>	74
5.12	<i>Contribution of CM, ADM, and MIM in Predicting the P-PED<sub>A</sub>, P-PED<sub>B</sub>, and Impedance Matching Damping Performance for OLS Manipulator</i>	75
5.13	<i>Coupling Map Performance Predictions for OLS Manipulator</i>	76
5.14	<i>Accelerative Damping Map Performance Predictions for OLS Manipulator</i>	77
5.15	<i>Modal Inertia Map Performance Predictions for OLS Manipulator</i>	77
5.16	<i>Change in Shape of Dominant (First) Mode of OLS Manipulator when IM Compliance is Introduced to SARA</i>	78
6.1	<i>Deployment Maneuvers and LAURA Configurations for Experiments with LAURA-SARA Manipulator</i>	81
6.2	<i>Representative SARA Base Elastic Deflections and Response of SARA Joints</i>	82
6.3	<i>Representative Strain Energy Plots Demonstrating the Range of Damping Performance Observed on the LAURA-SARA Manipulator</i>	83
6.4	<i>Measured Damping Performance on LAURA-SARA Manipulator Using P-PED</i>	85
6.5	<i>Measured Damping Performance on LAURA-SARA Manipulator Using Impedance Matching</i>	87
6.6	<i>Change in Frequency of Dominant Mode of LAURA-SARA Manipulator when IM Compliance is Introduced to SARA</i>	87
6.7	<i>Normalized Coupling Maps for LAURA-SARA Manipulator</i>	89
6.8	<i>Normalized Accelerative Damping Maps for LAURA-SARA Manipulator</i>	89
6.9	<i>Normalized Modal Inertia Maps for LAURA-SARA Manipulator</i>	90
6.10	<i>Contribution of CM, ADM, and MIM towards Predicting the P-PED and IM Damping Performance on the LAURA-SARA Manipulator</i>	91
A.1	<i>Assembled Small Articulated Rigid Arm (SARA)</i>	100
A.2	<i>Assembled SARA Shoulder Joint</i>	101
A.3	<i>SARA Shoulder Joint: Stator Housing</i>	102
A.4	<i>SARA Shoulder Joint: Stator Housing Cover</i>	103
A.5	<i>SARA Shoulder Joint: Rotor Shaft</i>	104
A.6	<i>Assembled SARA Elbow/Wrist Joint</i>	105
A.7	<i>SARA Elbow/Wrist Joint: Stator Housing</i>	106
A.8	<i>SARA Elbow/Wrist Joint: Stator Housing Mounting Bolt Patterns</i>	107
A.9	<i>SARA Elbow/Wrist Joint: Stator Housing Cover</i>	108

A.10 SARA <i>Elbow/Wrist Joint: Rotor Shaft</i> . . . . .	109
A.11 <i>Assembled SARA Base Assembly</i> . . . . .	110
A.12 SARA <i>Base Assembly: Main Base Support</i> . . . . .	111
A.13 SARA <i>Base Assembly: Flotation Arm</i> . . . . .	112
A.14 SARA <i>Base Assembly: Input Coupler</i> . . . . .	113
A.15 SARA <i>Base Assembly: Macro-Manipulator Link Adapter</i> . . . . .	114
A.16 SARA <i>Shoulder Output Link</i> . . . . .	115
A.17 SARA <i>Elbow/Wrist Output Link</i> . . . . .	116
A.18 SARA <i>Link Couplers</i> . . . . .	117
A.19 SARA <i>Internal Joint Spacers</i> . . . . .	118
C.1 <i>First Modal Frequencies for Exact and Reduced Systems with <math>\theta_{L2} = 0^\circ</math></i> . . .	125
C.2 <i>First Modal Frequencies for Exact and Reduced Systems with <math>\theta_{L2} = 45^\circ</math></i> . . .	125
C.3 <i>Second Modal Frequencies for Exact and Reduced Systems with <math>\theta_{L2} = 0^\circ</math></i> . . .	126
C.4 <i>Second Modal Frequencies for Exact and Reduced Systems with <math>\theta_{L2} = 45^\circ</math></i> . . .	127
C.5 <i>Second Modal Frequencies for Exact and Reduced Systems with <math>\theta_{S1} = \theta_{S2} = 0^\circ</math> through a Range of <math>\theta_{L2}</math> Angles</i> . . . . .	127

# List of Tables

2.1	<i>Mechanical and Electrical Characteristics of SARA Direct-Drive Brushed DC Motors</i> . . . . .	11
2.2	<i>Lengths of Rigid Extensions Appended to Flexible Links</i> . . . . .	16
2.3	<i>LAURA-SARA Manipulator Degrees of Freedom</i> . . . . .	19
2.4	<i>Inertial and Geometric Properties of LAURA-SARA Manipulator Rigid Bodies</i> . . . . .	19
2.5	<i>Measured Natural Frequencies of the LAURA-SARA Manipulator</i> . . . . .	23
2.6	<i>Numerically Predicted Frequencies vs Average Measured Frequencies for LAURA-SARA Manipulator</i> . . . . .	24
3.1	<i>Modal Analysis of Complete and Reduced Models of LAURA Manipulator and SARA Base: Frequencies and Mode Shapes</i> . . . . .	38
5.1	<i>Geometric and Inertial Properties of the VS Manipulators</i> . . . . .	61
6.1	<i>LAURA Deployment Details for LAURA-SARA Experiments</i> . . . . .	81
6.2	<i>First Mode Shape of LAURA-SARA Manipulator with SARA Locked in Straight-Out Configuration</i> . . . . .	88

to Rachelle, of course

# Chapter 1

## Introduction

### 1.1 Macro-Micro Manipulators

Robots have been traditionally constructed with rigid, or at least very stiff, links and joints. This type of robot has seen wide use on factory floors and is very well suited to that environment. In recent years, as robotics has moved into new environments, new classes of manipulators have arisen. One specialized class is characterized by light weight construction and a large work space, with the inevitable result of a very flexible manipulator. In this work, all such large, flexible manipulators will be called *macro*-manipulators.

The Shuttle Remote Manipulator System, or CanadArm as it is more commonly known, is a good example of a macro-manipulator. When it was conceived for use on the American Space Shuttles, the design and operational constraints were very different from those for traditional manipulators. Although rigidity would be beneficial, light weight was the dominant concern due to the prohibitive cost of placing a heavy arm in orbit. As with any manipulator, accurate end- effector position and force control is essential for performing tasks with the CanadArm. As such, the lightweight flexible links pose a control problem. To minimize vibrations, the arm must be moved very slowly and trajectories must be carefully planned. Even with these restrictions, operational time is wasted while residual vibrations decay.

The addition of a small, rigid *micro*-manipulator to the tip of the macro-manipulator

has been proposed as a solution to the competing design constraints of light weight, large work space, and accurate tip control. In practice, the large macro-manipulator is used to deploy the micro-manipulator to the vicinity of a work site. The particular task is then completed by taking advantage of the fine dexterous control of the micro-manipulator.

Two prominent examples of such *macro-micro* manipulators are illustrated in Figure 1.1. The Light Duty Utility Arm will be used for nuclear waste remediation at various United States Department of Energy sites. A Vertical Positioning Mast, 39' in length, is used to insert the seven degree-of-freedom arm in the tank through 12" diameter risers. Mast flexibility here is the result of geometric, rather than mass, restrictions. The Space Station Remote Manipulator System / Special Purpose dexterous Manipulator (SSRMS/SPDM) combination will be used in the construction of the International Space Station. Both the SSRMS/SPDM and the LDUA are under development by Spar Aerospace Ltd., in Ontario, Canada.

A planar macro-micro manipulator, the LAURA-SARA manipulator, was developed at the University of Victoria for experimental work. LAURA and SARA are acronyms for 'Long Articulated Uvic Robotic Arm' and 'Small Articulated Rigid Arm' respectively. Details of this manipulator are presented in Chapter 2.

## 1.2 Active Damping

Without special control techniques, the rigidity of the micro-manipulator is of little use when its base, the tip of the macro-manipulator, is vibrating. Macro-manipulator tip vibration can be reduced in two ways without adding additional hardware. First, *path-planning* aims to plan joint trajectories which minimize the magnitude of vibrations excited in the macro-manipulator. A micro-manipulator is not required for path-planning algorithms, but the extra degrees-of-freedom can be beneficial. The second option is to use the micro-manipulator to damp any residual macro-manipulator vibrations. Bandwidth considerations generally preclude the use of the macro-manipulator for such *active damping*.

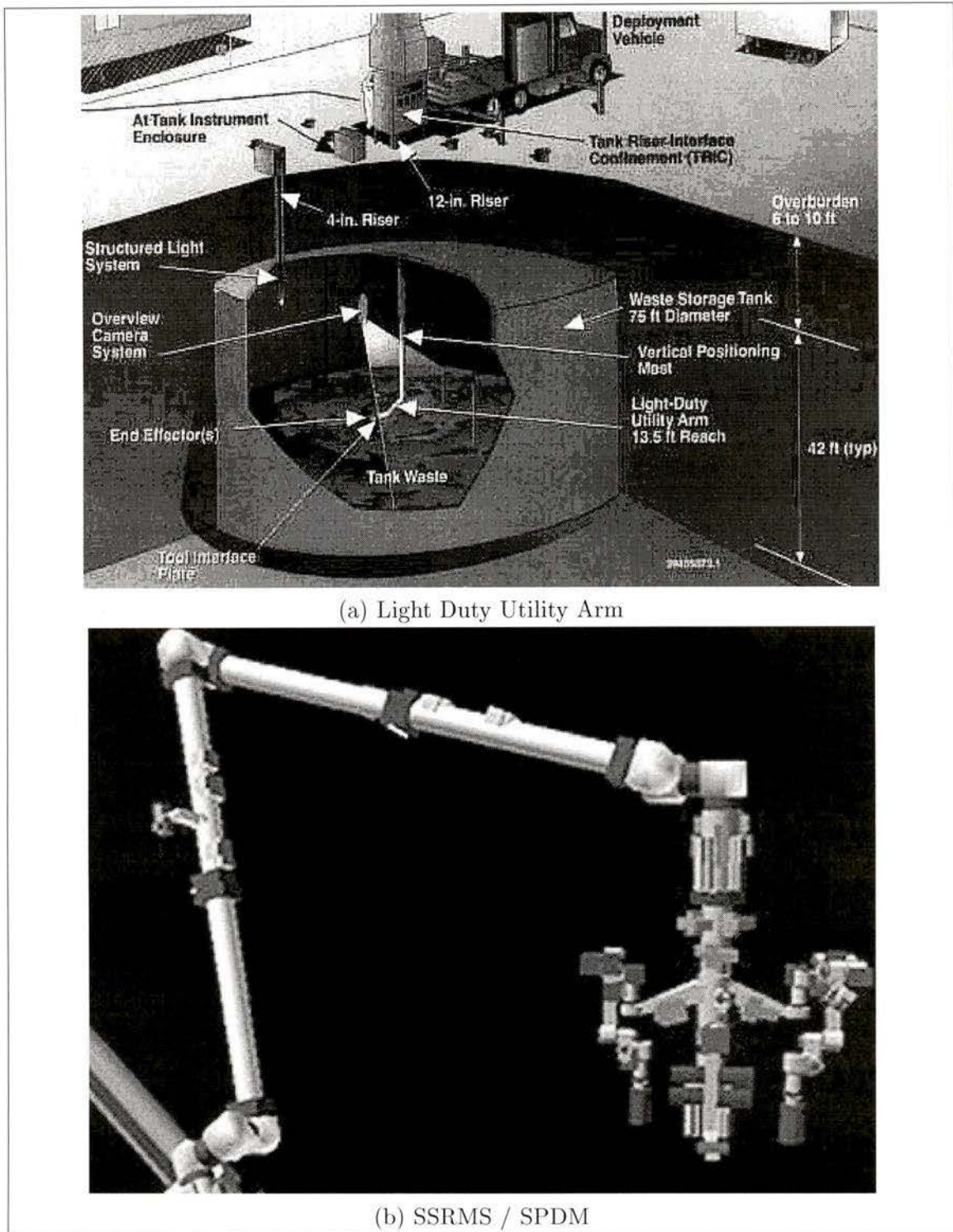


Figure 1.1: Two Examples of Macro-Micro Manipulators: Light Duty Utility Arm and SSRMS/SPDM

Path-planning and active damping are complementary strategies. The former is used to minimize the magnitude of the residual vibrations, but the inevitable remaining vibrations are dissipated by the latter.

The focus of this thesis is active damping using the micro-manipulator. Two active damping algorithms and three tools for predicting the optimal micro-manipulator configurations for active damping are tested. The algorithms and prediction tools are developed in Chapters 3 and 4 respectively. Simulation and experimental results are then presented in Chapters 5 and 6.

### 1.3 Review of Active Damping Literature

Prior to 1990, most active damping research was applied to the macro-manipulator alone, as macro-micro manipulators were virtually unknown. The limited bandwidth of the macro-manipulator actuators generally hinders the performance of this approach. With the advent of macro-micro manipulators, the research focus shifted to using the micro-manipulator for active damping. As this is also the goal of the present work, only micro-manipulator active damping research is summarized below.

A dual time scale approach to active damping was presented by Book [1]. A ‘slow’ controller is used for the rigid coordinates, while a ‘fast’ controller simultaneously dissipates elastic vibrations. The macro-manipulator model was simplified by locking the macro-manipulator joints and modelling elastic deflections with a single assumed mode. Micro-manipulator joint torques were calculated as a sum of the slow and fast controller commands. Only a theoretical presentation of the dual time scale algorithm was given, with no simulation or experimental results.

In a follow-up paper, Lee [9] extended the original theory for a micro-manipulator with any number of actuators, although the macro-manipulator joints were again assumed locked. Other changes increased the efficiency of the algorithm for real-time implementation. The slow (rigid) controller gains were calculated to give critical micro-manipulator damping,

with an upper bound placed on the proportional gains due to the required separation between the closed-loop rigid (slow) frequencies and the elastic (fast) frequencies. The micro-manipulator joint torques from the slow controller were augmented with fast controller torques calculated from elastic deflection measurements. The fast controller gains were chosen with classical root-locus techniques to give highly damped poles for the elastic system.

Experimental results on the Georgia Institute of Technology's experimental macro-micro manipulator were also presented by Lee [9]. The acronyms RALF and SAM, for 'Robotic Arm, Long and Flexible' and 'Small Articulated Manipulator', identify the macro- and micro-manipulators respectively. For the active damping experiments, all RALF joints were locked, and a single SAM joint was also locked so that all motion was co-planar. Excellent damping performance was obtained.

Further experimental work and implementation details were presented by Lee [8]. Additionally, a simple lumped parameter model of the RALF-SAM manipulator was used to decide on the best configurations for active damping. Very specific RALF and SAM configurations were required to avoid phase-lag problems because the strain gauge sensors and SAM joints were not collocated.

Trudnowski [24] proposed a second approach to active damping, called inertial damping. Again the macro-manipulator joints were assumed locked and only the first elastic mode was used in the controller design. The micro-manipulator joint torques computed using traditional, stiff PD gains were augmented with torques calculated from elastic state feedback. Since the elastic state feedback is separate from the rigid state feedback, the control architecture is versatile and simple to implement.

Experimental validations of the inertial damping method were performed on the large test facility at the Pacific National Laboratory (PNL) in Richland, Washington [10, 11]. A linearized model of the manipulator was developed and stiff joint PD gains were chosen for the rigid feedback loop. The elastic state feedback gains were calculated, using classical

root-locus procedures, to dissipate first elastic mode vibration while limiting the bandwidth to avoid exciting higher elastic modes.

Further experimental work at PNL [2, 3] and with the SAM manipulator [3] investigated the use of inertial damping in conjunction with command filtering techniques. Command filtering is a method of local path-planning and is not discussed further. However, it was noted that damping performance (using inertial damping) was dependent on the micro-manipulator configuration. No significant attempt at determining the optimum micro-manipulator configurations was made.

Sharf [15, 16] presented an alternative active damping algorithm, where the macro- and micro-manipulators were considered separately. A desired instantaneous macro-manipulator tip wrench for active damping was calculated, and micro-manipulator joint motions which would apply this desired wrench were found. There was, however, no provision for micro-manipulator position or velocity control and large joint rates would often result.

The above active damping methods all rely on the availability of elastic state measurements. In Chapter 3, such methods are termed Cartesian Space Derivative (CSD) control. Joint Space Derivative (JSD) control methods, such as the Pseudo-Passive Energy Dissipation (P-PED) algorithm developed by Torres [21, 23], are fundamentally different. Rather than sensing the elastic state, it is observed indirectly through the motions induced in the micro-manipulator by macro-manipulator vibrations. (See Chapter 3 for a more thorough explanation of CSD and JSD control methods).

P-PED sought to approximate the micro-manipulator as a combination of simple mass-spring-damper systems. Each mass-spring-damper was tuned to dissipate linear macro-manipulator tip motion in a specific direction. Consistent with the above methods, the macro-manipulator joints were assumed locked.

Experimental validations of P-PED were performed on two manipulators; the Martin Marietta Harmonic Drive Manipulator [21, 23] and the Massachusetts Institute of Technology Elastic Beam Manipulator [23]. The damping under P-PED control was considerably

better than with stiff PD gains. Optimal Harmonic Drive Manipulator configurations for P-PED experimentation were found using the Coupling Map [21, 22], which was originally presented as a path-planning tool.

## 1.4 Thesis Organization

In Chapter 1, the motivation for macro-micro manipulators and the problem of macro-manipulator vibration were introduced. The problem can be addressed by using path planning and/or active damping. Actively damping macro-manipulator vibrations with the micro-manipulator, and predicting the best micro-manipulator configurations for doing so, are the goals of this work. Previous research in these areas was summarized.

The University of Victoria's LAURA-SARA manipulator is discussed in Chapter 2. Mechanical design of the manipulator, the development of a numerical model, model validation, and control system details are described.

All theory and derivations are presented in Chapters 3 and 4. In Chapter 3, the two active damping methods that form the basis of simulation and experimental work, Pseudo-Passive Energy Dissipation and Impedance Matching, are derived. Implementation details for the simulations and experiments are also discussed. The Coupling Map (CM), Accelerative Damping Map (ADM), and Modal Inertia Map (MIM) are introduced in Chapter 4 as tools for predicting the optimal micro-manipulator configurations for active damping. Such tools have received little attention in previous work.

Chapters 5 and 6 are dedicated to the presentation and discussion of results. Simulation results for four very simple macro-micro manipulators and a simplified LAURA-SARA manipulator are presented in Chapter 5. Experimental results on the LAURA-SARA manipulator are presented in Chapter 6. In each case, the performance predictions from CM, ADM, and MIM are shown and compared to the simulation/experimental results.

Conclusions, thesis contributions, and future research opportunities are discussed in Chapter 7.

## Chapter 2

# Experimental Facility

The planar robotics test facility at the University of Victoria is versatile and well suited to a range of experimental studies [17, 18, 19, 26]. A large glass table supports up to three NSK direct-drive joints, three Harmonic Drive joints, and a newly constructed micro-manipulator. Air bearings under each joint minimize friction with the table.

For this work the facility is configured as a macro-micro manipulator called the LAURA-SARA manipulator. LAURA is an acronym for Long Articulated UVic Robotic Arm, and SARA for Small Articulated Rigid Arm. A photograph of the assembled manipulator is shown in Figure 2.1.

This chapter is composed of five sections. In the first two, the mechanical details of LAURA and SARA are given. A numerical model of the complete manipulator is developed in §2.3 and validated experimentally in §2.4. Finally, control system details are presented in §2.5.

### 2.1 Macro-Manipulator (LAURA)

The components of LAURA have been discussed extensively in previous work, and therefore are only summarized here. A general description of the complete facility, prior to the addition of SARA, is available in [13].

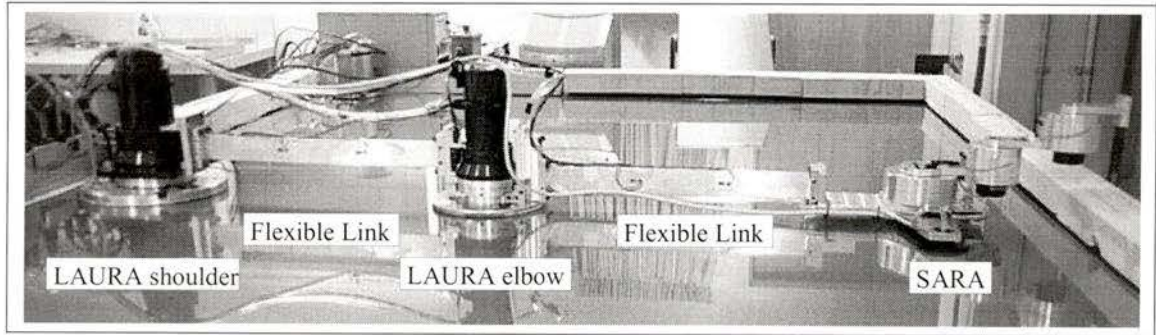


Figure 2.1: *University of Victoria's Experimental Macro-Micro Manipulator (LAURA-SARA)*

Two Harmonic Drive (HD) motors actuate the macro-manipulator. Models RFS-32-6030 and RFS-25-6018 are used at the shoulder and elbow respectively, delivering peak torques of 215 Nm and 100 Nm. Harmonic drive gearboxes do not suffer from the backlash associated with conventional gearboxes, but do have more flexibility and generally higher friction. Wright describes the structure and operation of the LAURA HD motors in an investigation of control schemes for flexible joint manipulators [26].

Stanway [19] modelled the flexible links as part of his validation of a flexible manipulator simulation on this facility. Each link is made from a 500mm length of aluminum with a  $50 \times 6.35$ mm cross-section.

## 2.2 Micro-Manipulator (SARA)

The SARA manipulator was designed and constructed specifically for this work. Machining drawings for the complete manipulator are available in Appendix A. The mechanical design was driven by two types of constraints. First, SARA had to integrate into the existing facility, including the existing (macro-) joints and links, air system (for the air-bearings), control hardware and overall control architecture. These requirements dictated a design with the following main features:

- it is a planar, three-DOF robot, approximately 1/4 the length and mass of LAURA;
- it uses an air-bearing flotation system for support on the existing test-bed table;
- it has unlimited joint rotation.

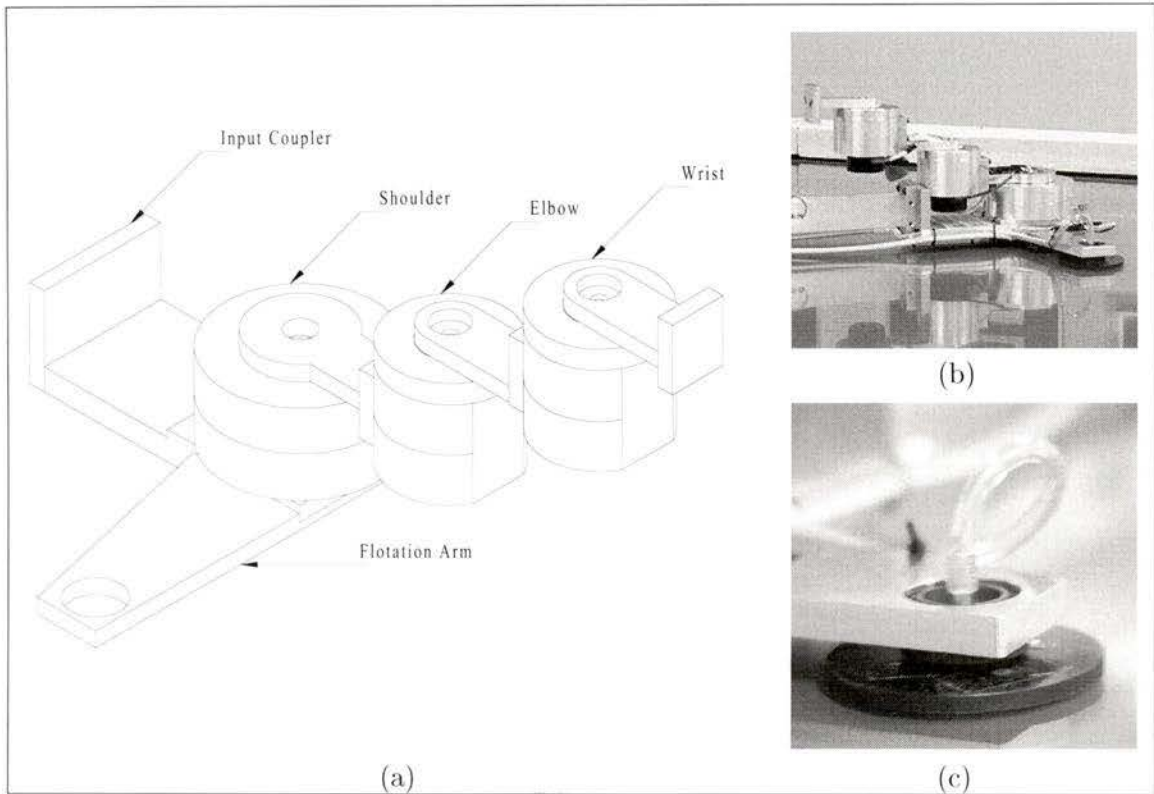


Figure 2.2: *Small Articulated Rigid Arm (SARA)*

The second type of constraint stemmed from SARA's intended use, which was for dexterous tasks, and for active damping in particular. The overall shape of SARA is shown in the drawing and photos of Figure 2.2. Detailed descriptions of SARA's construction, actuation, and flotation follow.

### 2.2.1 Motors and Amplifiers

The micro-manipulator has been designed around three direct-drive brushed DC motors from Inland Motor. Direct-drive motors were chosen based on an analysis of the required micro-manipulator motion for active damping, which revealed requirements for high bandwidth operation and rapid starts and stops. The following joint characteristics are thus desirable:

- low static and viscous friction for efficient operation;
- stiff output to avoid structural resonances;
- high torque-to-inertia ratio at the output for rapid acceleration.

Gearboxes tend to add both friction and compliance to the output, so direct-drive motors are the obvious preference to satisfy the first two requirements. The third seems to favour a geared motor, since the maximum torque output from a given motor increases linearly with the gear ratio. However, the effective rotor inertia increases with the *square* of the gear ratio, so the torque-to-inertia ratio of a given motor in *isolation* actually *decreases* as the gear ratio is increased. (The advantage of direct-drive motors does however decrease with a large inertial load at the output). Neither type of motor therefore offers a definitive advantage for rapid acceleration. Since direct-drive motors are the clear choice for two out of three requirements, they were chosen to actuate SARA.

The particular choice to use DC *brushed* motors was based on previous experience with NSK brushless direct-drive motors, which were found to be highly non-linear and difficult to control. Brushed motors have a very linear relationship between the current input and torque output, so that calibration and accurate torque control are simplified.

The final motor specification was based on size limits and the torque-to-mass ratio. Table 2.1 summarizes the selected motors, which are designed to deliver high torques at low speeds and have small electrical time constants for fast response [7]. The motors are frameless, meaning that the brush ring, stator, and rotor were supplied as separate pieces. The motor mass properties in Table 2.1 do not include the joint housings. Mass properties for the complete joints are given in §2.3.

Table 2.1: *Mechanical and Electrical Characteristics of SARA Direct-Drive Brushed DC Motors*

	Shoulder (T-3910)	Elbow/Wrist (T-2171)
Max torque (Nm)	1.36	0.85
Max speed (rad/s)	36	57
Outside diam (mm)	115.9	71.4
Inside diam (mm)	74.6	25.4
Mass (g)	499	383
Time Constant (ms)	0.84	1.5

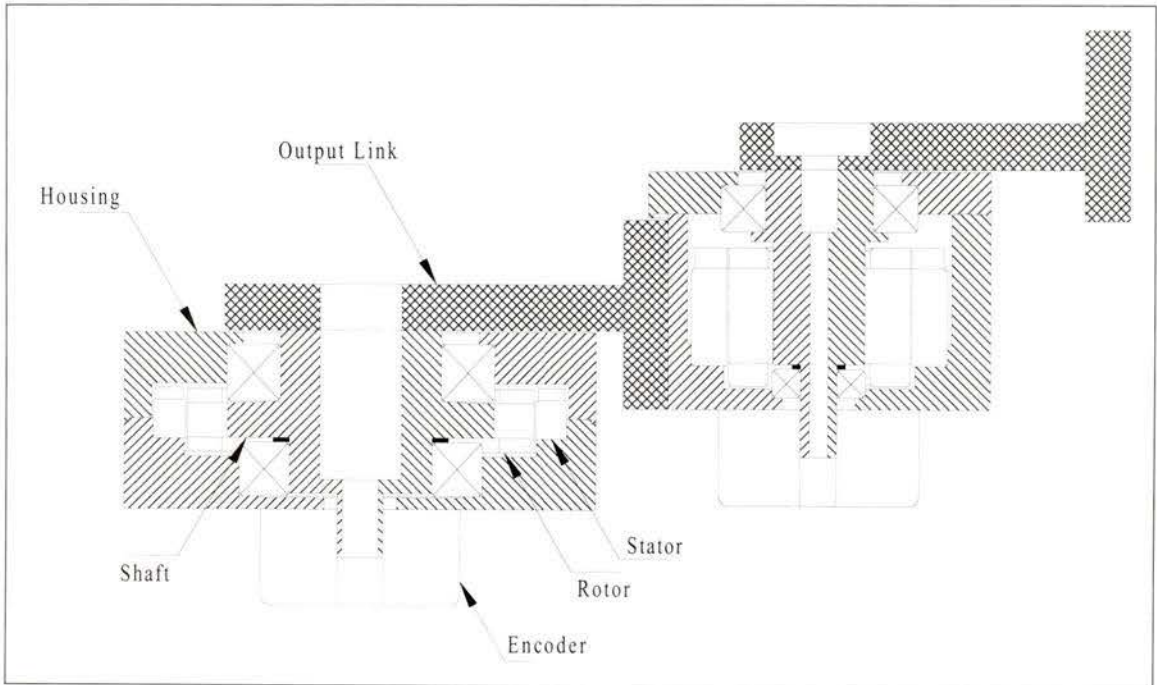


Figure 2.3: *Cutaway Views of SARA Joints*

The Precision Micro Dynamics BT-28V-6A linear amplifier was selected for its linear output, configuration options, low price, and local availability. Conventional Pulse Width Modulation (PWM) amplifiers are electrically noisy at the pulsing frequency. Their use in the vicinity of analog sensors, such as the strain gauges used in this facility, is therefore problematic. Linear amplifiers produce a DC current output proportional to the instantaneous commanded torque, and thereby avoid the electrical noise problem.

### 2.2.2 Joint Design

Since the T-3910 and T-2171 motors are frameless, a housing design for each joint was required. The internal structure of the joints is shown in Figure 2.3. The elbow and wrist joints are identical except for minor differences in the mounting bolt patterns on the input couplers. Initially, slip rings were specified for each joint to allow truly unlimited joint rotations, but the large number of additional electrical connections proved difficult to maintain. Braided wires now run through each joint, allowing for two to three complete revolutions.

### 2.2.3 Geometry and Flotation

The cantilevered, offset construction of SARA allows each joint to turn through a complete revolution without interference. In Figure 2.2b, the SARA shoulder joint is shown rotated 180°. The elbow joint passes through the open space between the shoulder joint and its input coupler. There is also no contact between the SARA wrist joint and the second macro-manipulator link as the former swings over the latter.

The air-bearings under each joint are capable of supporting large vertical loads, but only small out-of-plane moments. The LAURA design minimizes the out-of-plane moments by aligning the joint centres of mass in a plane parallel to the table. It was not possible to similarly align the SARA centres of mass because of its cantilevered construction. Instead, a *flotation arm* with two air pads was required, as shown in Figures 2.2b and 2.2c. Spherical bearings at each pad ensure that no moments are applied to the pads, and allow them to float over small irregularities in the table. Together with the air-bearing under the LAURA elbow joint, the two SARA air pads form a stable tripod against all out-of-plane loads.

A single air line supplies both SARA air pads by way of a T-fitting. On each arm of the T, the tubing is severely restricted to present a large resistance to air flow. Without these restrictions, unequal loads on the pads would result in collapse of the heavily loaded air-bearing.

## 2.3 LAURA-SARA Manipulator Model

An accurate model of the macro-micro manipulator is required for the active damping calculations described in Chapters 3 and 4. In this section, a complete inertial and stiffness model is described.

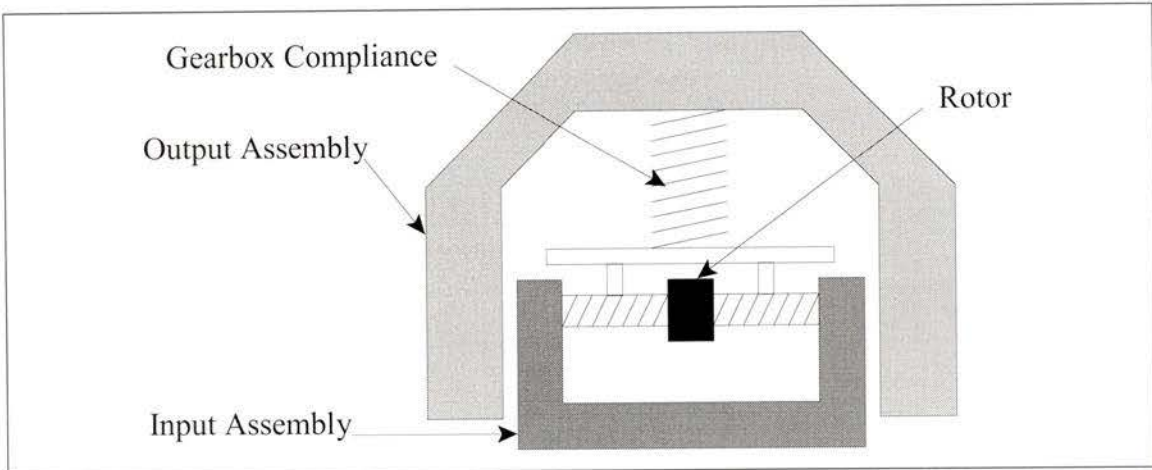


Figure 2.4: *Model of Harmonic Drive Joints*

### 2.3.1 LAURA Manipulator

#### Joints

The HD motor model developed by Wright [26] includes inertial properties for every motor component, and a gearbox model comprising stiffness, linear viscous friction, and static friction. The model presented here is based on Wright's work. For the purposes of frequency domain validation, closed-loop proportional gains are incorporated into the joint models. The friction terms have however been dropped as their effect on the system is masked by the closed-loop control.

Figure 2.4 illustrates the HD joint model used to develop the joint stiffness and inertia characteristics. Each joint is represented by three bodies, namely the input assembly, the rotor, and the output assembly. The harmonic drive gearbox is represented by a planetary geartrain for simplicity. Gearbox compliance is modelled by a torsional spring between the rotor and the output assembly. The experimentally determined spring constants [26] are 18000 and 10000 Nm/rad for the LAURA shoulder and elbow respectively. For convenience, the rotor angle is measured at the output of the gear reduction, just before the torsional spring.

The effective inertia of the rotor,  $I_{r,e}$ , is dependent on the relative motion between the rotor and the input assembly. When the two bodies rotate together, the effective rotor

inertia is equal to its actual inertia,  $I_{r,e} = I_r$ . However, for relative motion between these bodies, the actual inertia is multiplied by the square of the gear ratio,  $N$ , to arrive at the effective inertia,  $I_{r,e} = N^2 I_r$ . The gear ratio is 51 for the LAURA shoulder and 50 for the elbow.

The rotary dynamics of a single harmonic drive joint can be described as follows:

$$\mathbf{I}\ddot{\boldsymbol{\theta}} + \mathbf{K}_g\boldsymbol{\theta} = \boldsymbol{\tau} \quad (2.1)$$

where  $\mathbf{I}$  and  $\mathbf{K}_g$  are the joint inertia and gearbox stiffness matrices defined as

$$\mathbf{I} = \begin{bmatrix} I_i + I_r(\frac{1}{4} + N^2) & I_r(\frac{1}{4} - N^2) & 0 \\ I_r(\frac{1}{4} - N^2) & I_r(\frac{1}{4} + N^2) & 0 \\ 0 & 0 & I_o \end{bmatrix}, \quad \mathbf{K}_g = \begin{bmatrix} 0 & 0 & 0 \\ 0 & k_g & -k_g \\ 0 & -k_g & k_g \end{bmatrix}, \quad (2.2)$$

$\boldsymbol{\theta} = [\theta_i, \theta_r, \theta_o]^T$ , and  $\boldsymbol{\tau} = [-\tau_r, \tau_r, 0]^T$ . The  $-\tau_r$  term is a reaction torque which acts against the input assembly.

For the frequency domain validation experiments, the macro-manipulator joints are ‘locked’ in a nominal configuration by applying control torques proportional to the joint position errors. To model this, the gearbox stiffness matrix in equation (2.1) is augmented with the rotor stiffness matrix due to the proportional gain,

$$\mathbf{P} = \begin{bmatrix} P & -P & 0 \\ -P & P & 0 \\ 0 & 0 & 0 \end{bmatrix} \quad (2.3)$$

The traditional model where the rotor is rigidly attached to the input assembly is approximated with a very high proportional gain,  $P$ . In §2.4, numerical frequencies are calculated for this *rigid* case using  $P = 10^9$  Nm/rad. A *compliant* case is also investigated, where  $P$  for each joint is set equal to the actual proportional gain used experimentally. These gains

are 8000 and 4000 Nm/rad for the LAURA shoulder and elbow respectively.

## Links

The two flexible links are modelled as cantilevered beams discretized with a single beam element. Accordingly, each link has three local (elemental) degrees of freedom; two tip displacements and a tip rotation.

The links are connected to the joints via standard input and output couplers. Each coupler, and the corresponding link end-point, is offset radially from the joint axis of rotation. To avoid introducing additional coordinate frames, the link models are appended with rigid, massless extensions equal in length to the appropriate radial offset. The link coordinate frames are thus identical to the joint input or output frames. The extension lengths for each link are given in Table 2.2.

Table 2.2: *Lengths of Rigid Extensions Appended to Flexible Links*

	Proximal (m)	Distal (m)
First Link	0.115	0.095
Second Link	0.120	0.200

### 2.3.2 SARA Manipulator

The direct-drive joints of SARA are much simpler to model than the harmonic drive macro-manipulator joints. The complete micro-manipulator is represented by four rigid bodies: the base, shoulder output, elbow output, and wrist output. Isometric drawings of these four bodies are shown in Figure 2.5.

Since the micro-manipulator was designed and built in-house, the dimensions and material properties of all component pieces are accurately known. Only the bearings and encoders required modelling assumptions. The bearings are approximated with two concentric homogeneous hollow cylinders whose total mass matches that of the actual bearing. The inner cylinder rotates with the joint rotor while the outer is fixed to the housing. The encoders are modelled as solid, homogeneous cylinders attached to the joint housing.

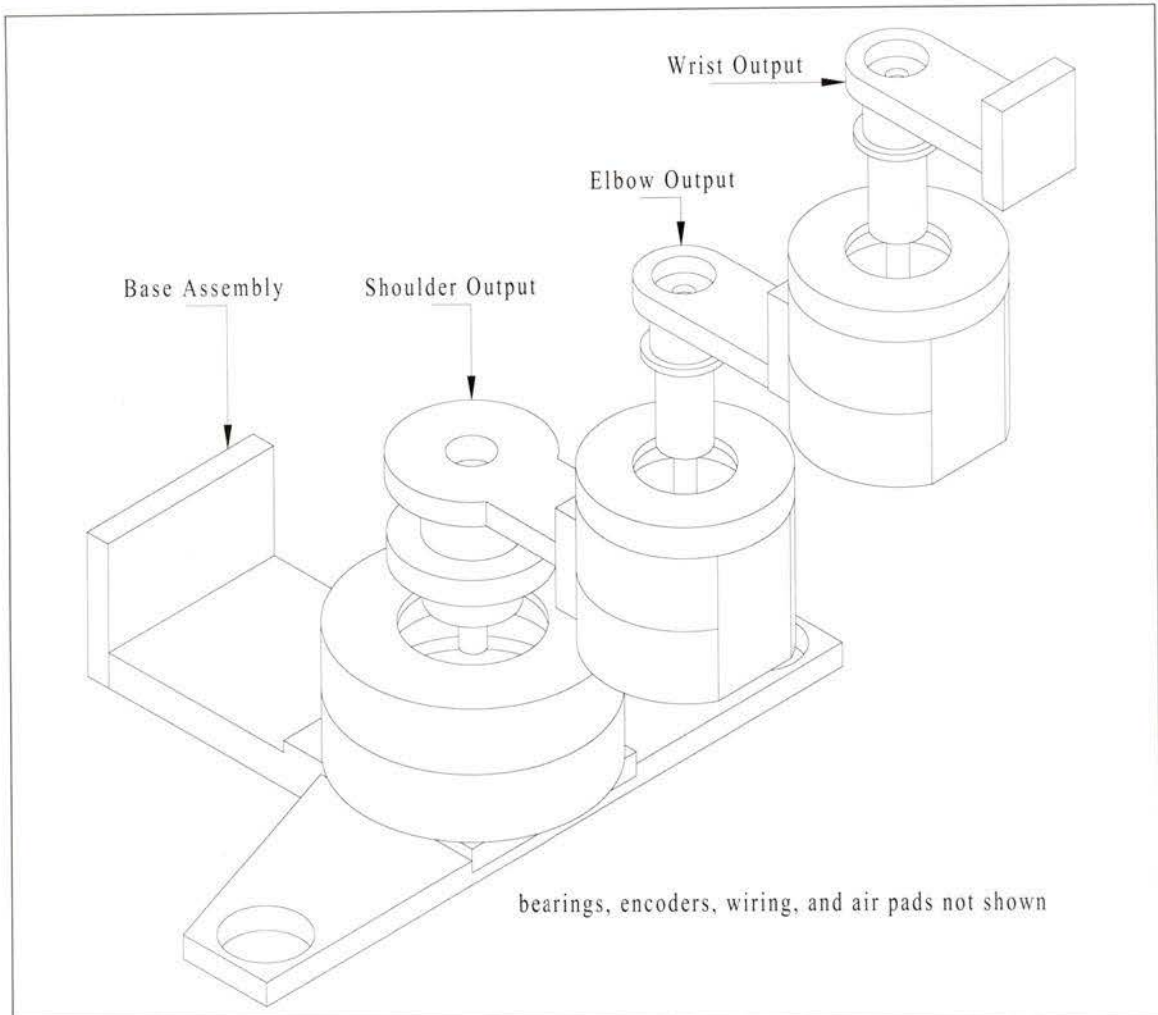


Figure 2.5: *Four Component Bodies of the SARA Model*

### 2.3.3 Assembled Model

The complete macro-micro manipulator model is illustrated in Figure 2.6, with a total of nine rigid bodies, two flexible links, and 13 degrees of freedom. The global coordinate frame for this work has its origin located at the LAURA shoulder axis of rotation, and is oriented with the global  $X$ -axis parallel to the LAURA elbow output in its nominal configuration. This is an unusual frame orientation suitable only for work in which the LAURA joints do not rotate, such as modal analysis or active damping with the LAURA joints locked. It does however allow for easy interpretation of all results in terms of their effect on SARA.

Symbols for each degree of freedom and the body-fixed coordinate frames are introduced

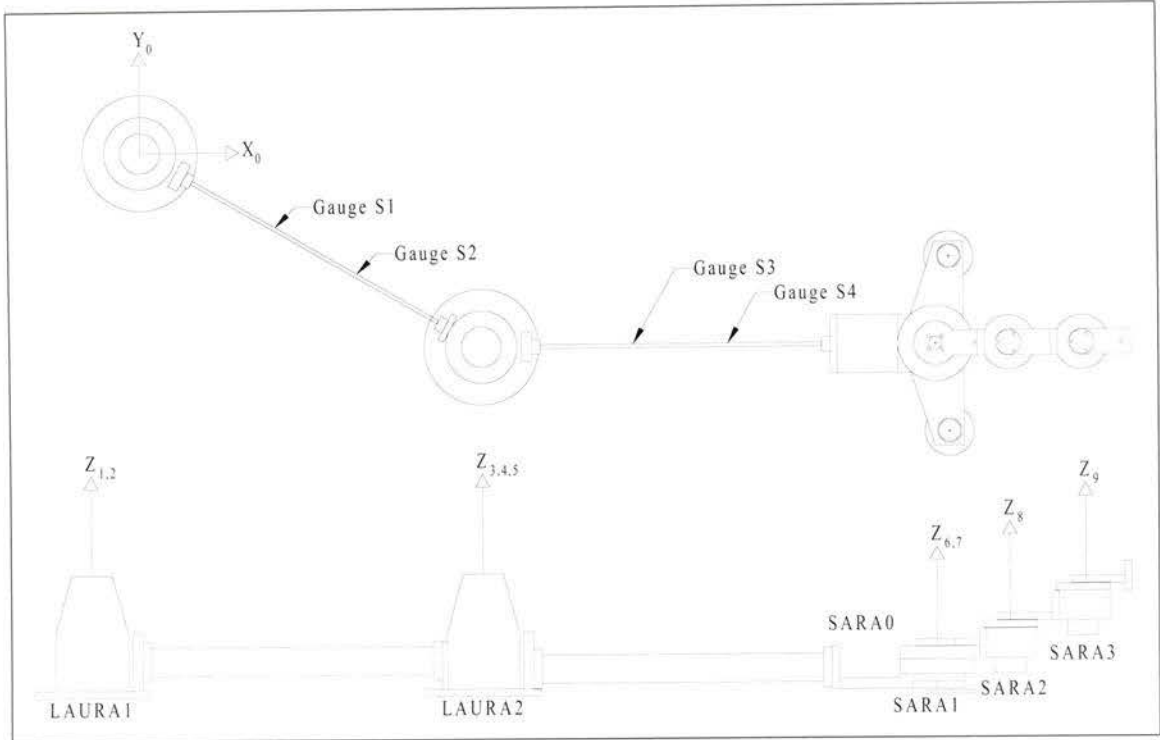


Figure 2.6: *Complete LAURA-SARA Manipulator Model*

in Table 2.3. The symbol  $\theta_{L2}$  is often used throughout this thesis to represent the LAURA elbow angle. It is interpreted as the difference between the input and output angles of the joint,  $\theta_{L2} = \theta_{L2o} - \theta_{L2i}$ .

The inertial and geometric properties of the rigid bodies are presented in Table 2.4. Here,  $r_{cg}$  is the distance from the origin of the body's coordinate frame to the body's centre of mass, and  $L$  is a similar quantity measured to the origin of the next body coordinate frame.

The global motion equations for the LAURA-SARA manipulator can be derived by applying the Lagrangian technique. For the modal analysis presented in §2.4 and for the active damping theory presented in Chapters 3 and 4, only the linearized dynamics are required. The linearized equations of motion take the form:

$$\mathbf{M}(\bar{\mathbf{q}})\ddot{\mathbf{q}} + (\mathbf{K}(\bar{\mathbf{q}}) + \mathbf{P})\mathbf{q} = \mathbf{0} \quad (2.4)$$

Table 2.3: LAURA-SARA Manipulator Degrees of Freedom

Frame	Description	Symbol
1	LAURA1 rotor angle	$\theta_{L1r}$
2	LAURA1 output angle	$\theta_{L1o}$
3	LAURA2 X-translation	$x_{L2}$
3	LAURA2 Y-translation	$y_{L2}$
3	LAURA2 input angle	$\theta_{L2i}$
4	LAURA2 rotor angle	$\theta_{L2r}$
5	LAURA2 output angle	$\theta_{L2o}$
6	SARA0 X-translation	$x_{S0}$
6	SARA0 Y-translation	$y_{S0}$
6	SARA0 angle	$\theta_{S0}$
7	SARA1 output angle	$\theta_{S1}$
8	SARA2 output angle	$\theta_{S2}$
9	SARA3 output angle	$\theta_{S3}$

Table 2.4: Inertial and Geometric Properties of LAURA-SARA Manipulator Rigid Bodies

Frame	Body	mass (kg)	$r_{cg}$ (m)	$I_{cg}$ (kg m <sup>2</sup> )	$L$ (m)
1	LAURA1 rotor	<sup>a</sup> .	.	1.17e-3	0.000
2	LAURA1 output	<sup>a</sup> .	.	1.42e-1 <sup>d</sup>	0.710
3	LAURA2 input	<sup>b</sup> .	0.0 <sup>c</sup>	8.13e-3	0.000
4	LAURA2 rotor	7.558	0.0	4.30e-4	0.000
5	LAURA2 output	<sup>b</sup> .	0.0 <sup>c</sup>	6.52e-3	0.820
6	SARA0	3.946	-0.0262	3.85e-2	0.000
7	SARA1 output	2.062	0.0704	1.03e-2	0.128
8	SARA2 output	1.788	0.0817	7.88e-3	0.128
9	SARA3 output	0.731	0.0144	8.01e-4	.

Notes:

- a) not required
- b) stated rotor mass is the complete joint mass
- c) approximated to zero to simplify model
- d)  $I$  is about axis of rotation, not cg

where  $\mathbf{q}$  contains the 13 degrees of freedom for the system, and  $\mathbf{M}(\bar{\mathbf{q}})$  and  $\mathbf{K}(\bar{\mathbf{q}})$  are the manipulator mass and stiffness matrices at a nominal configuration  $\bar{\mathbf{q}}$ . For the modal analysis, the natural frequencies are obtained by solving the eigenproblem for the above model where, as discussed earlier, the matrix  $\mathbf{P}$  accounts for the effect of closed-loop proportional gains on the HD joint compliance.

## 2.4 Frequency Domain Model Validation

### 2.4.1 Impact Experiments

The constrained natural frequencies of the assembled macro-micro manipulator were determined by a series of impact experiments. Tests were performed at four manipulator configurations defined by the nominal LAURA elbow and SARA shoulder joint angles,  $\bar{\theta}_{L2}$  and  $\bar{\theta}_{S1}$ :

- I** LAURA elbow straight, SARA shoulder straight ( $\bar{\theta}_{L2} = 0^\circ$ ,  $\bar{\theta}_{S1} = 0^\circ$ )
- II** LAURA elbow straight, SARA shoulder rotated ( $\bar{\theta}_{L2} = 0^\circ$ ,  $\bar{\theta}_{S1} = 180^\circ$ )
- III** LAURA elbow bent, SARA shoulder straight ( $\bar{\theta}_{L2} = 45^\circ$ ,  $\bar{\theta}_{S1} = 0^\circ$ )
- IV** LAURA elbow bent, SARA shoulder rotated ( $\bar{\theta}_{L2} = 45^\circ$ ,  $\bar{\theta}_{S1} = 180^\circ$ )

The above configurations are illustrated in Figure 2.7. In all tests, the micro-manipulator joints were mechanically locked to avoid large joint movements and/or torque saturation from the impact. Proportional gains of 8000 and 4000 Nm/rad were used for LAURA1 and LAURA2 respectively to hold the joints in their nominal configurations. Higher gains were found to lead to instability due to unmodelled non-linearities, such as electrical rise time and encoder discretization. No derivative gain was applied since joint friction alone provides sufficient damping of the response.

Each test consisted of a sharp impact applied to the macro-manipulator elbow joint. Strain gauge data was collected from the four strain gauges labelled in Figure 2.6 and stored at 100 Hz for 10 seconds following the impact.

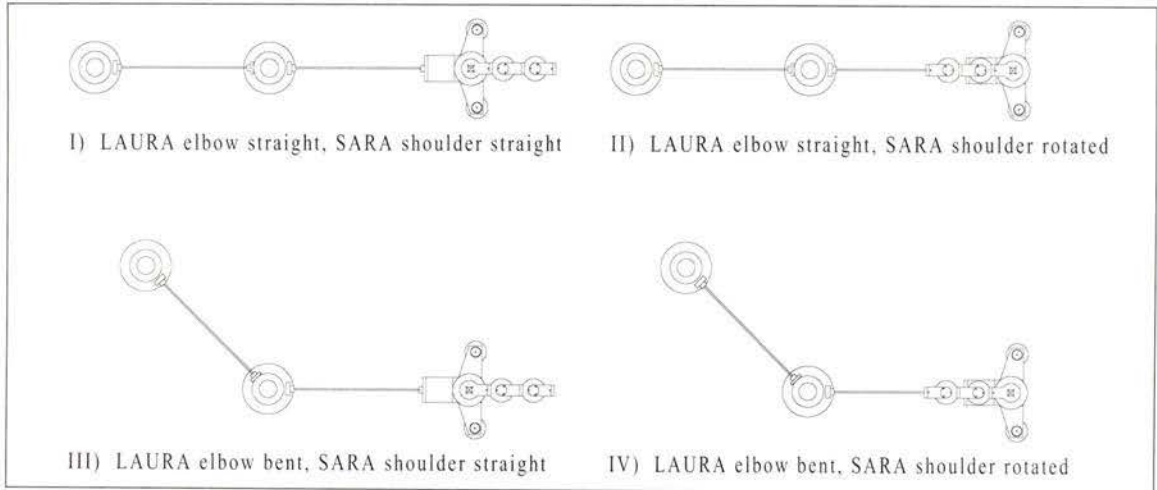


Figure 2.7: LAURA-SARA Manipulator Configurations for Impact Experiments

## 2.4.2 Experimental Data Analysis

Figure 2.8 is a representative plot of strain response from gauge S3 in manipulator configuration **IV**. Two modes of vibration are clearly visible in the time domain plot. The Discrete Fourier Transform (DFT) plot of the same data reveals three response peaks at 0.5, 2.8, and 10.9 Hz.

More accurate modal frequency estimates were obtained by fitting a sum of two decaying sinusoids to the experimental data. A non-linear curve fit of the form

$$g(t) = A_1 e^{-k_1 t} \sin(\omega_1 t + \phi_1) + A_2 e^{-k_2 t} \sin(\omega_2 t + \phi_2) \quad (2.5)$$

was used with initial parameter estimates taken from the DFT analysis. The MATLAB function **fmins** was used for the curve fit.

Figure 2.9 demonstrates the excellent fit of data ( $r^2 = 0.985$ ) obtained from equation (2.5). This is typical of the results from the other strain gauges and manipulator configurations. For this particular experiment and gauge, the first and second modal frequencies were 0.52 Hz and 2.82 Hz. Table 2.5 summarizes the measured frequencies for all strain gauges and macro-micro manipulator configurations. The observed damping ratios,  $\zeta$ , were less than 0.06 for the first mode and 0.01 for the second mode.

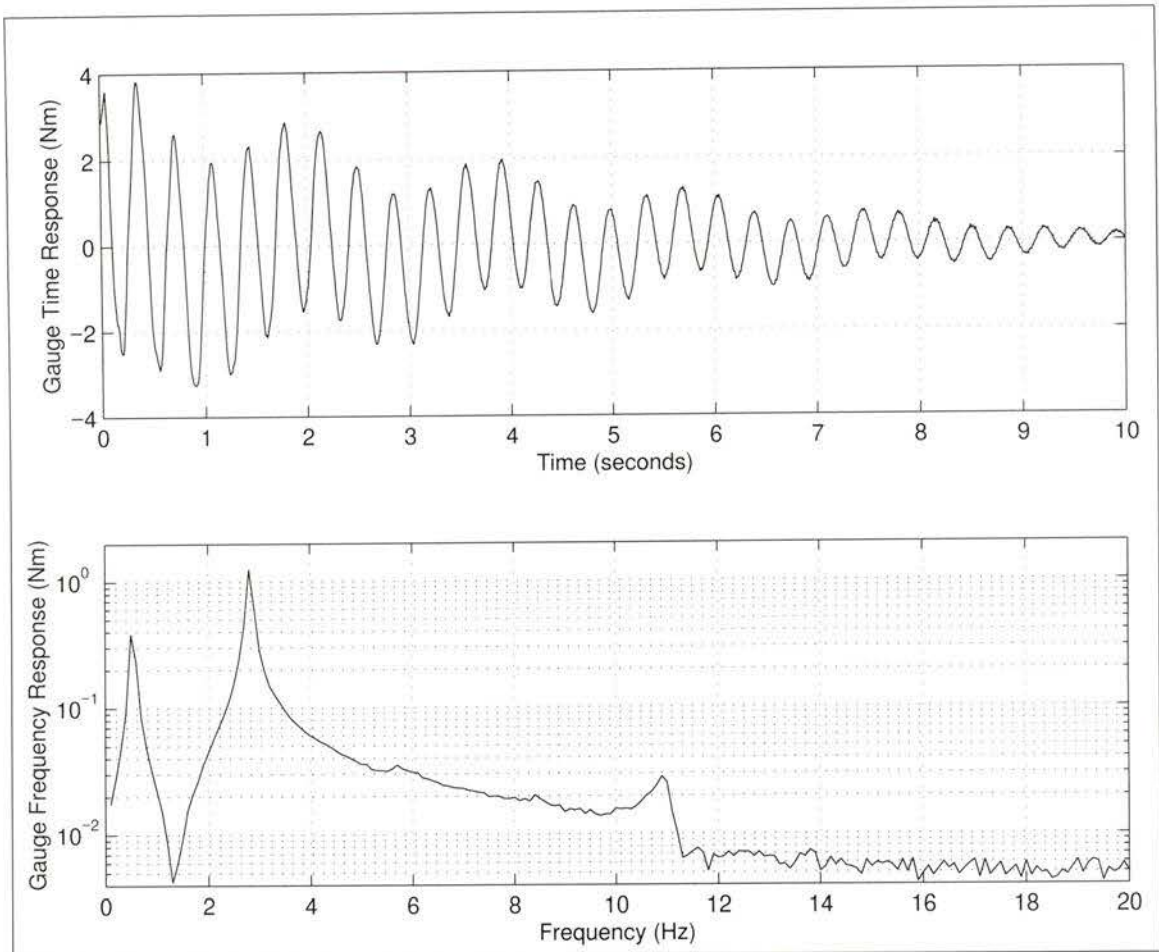


Figure 2.8: *Representative Plot of Strain Gauge Response to Impact Experiment*

### 2.4.3 Predicted Frequencies

The numerical natural frequencies are calculated from the model developed in §2.3, equation (2.4). The SARA degrees of freedom are dropped from the model since its joints were mechanically locked in the experiments. Numerical frequencies were calculated for rigid and compliant HD joint models to ascertain the effects of joint compliance. See §2.3.1 for an explanation of these models. The numerical results are shown versus the measured experimental frequencies in Table 2.6.

### 2.4.4 Discussion

The results in Table 2.6 demonstrate a very good agreement between the model and measured response in the frequency domain. Using the compliant joint model, the largest

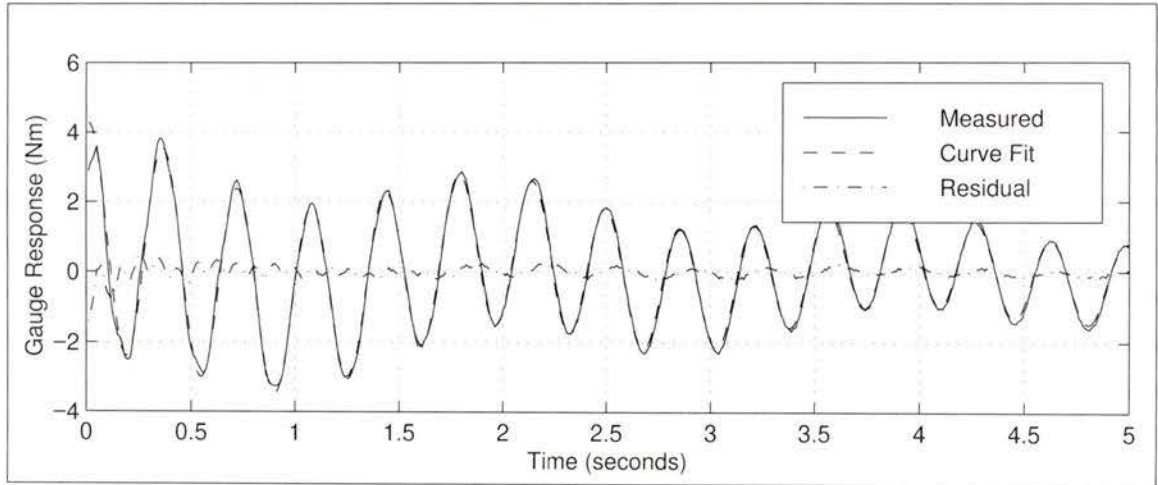


Figure 2.9: Sample Data and Decaying Sinusoid Curve Fit

Table 2.5: Measured Natural Frequencies of the LAURA-SARA Manipulator

Configuration	Gauge	Mode 1	Mode 2
		Frequency (Hz)	Frequency (Hz)
<b>I</b> LAURA2 straight, SARAI straight	S1	0.43	3.12
	S2	0.43	3.12
	S3	0.43	3.12
	S4	0.43	3.12
	avg	0.43	3.12
<b>II</b> LAURA2 straight, SARAI rotated	S1	0.50	3.50
	S2	0.50	3.51
	S3	0.50	3.50
	S4	0.50	3.50
	avg	0.50	3.50
<b>III</b> LAURA2 bent, SARAI straight	S1	0.45	2.55
	S2	0.45	2.55
	S3	0.45	2.55
	S4	0.45	2.55
	avg	0.45	2.55
<b>IV</b> LAURA2 bent, SARAI rotated	S1	0.53	2.82
	S2	0.53	2.81
	S3	0.52	2.82
	S4	0.52	2.82
	avg	0.52	2.82

Table 2.6: *Numerically Predicted Frequencies vs Average Measured Frequencies for LAURA-SARA Manipulator*

	Mode 1 Frequency (Hz)					Mode 2 Frequency (Hz)				
	Meas	Rigid		Compliant		Meas	Rigid		Compliant	
	Freq	Freq	Error	Freq	Error	Freq	Freq	Error	Freq	Error
<b>I</b>	0.43	0.47	8.4%	0.46	6.3%	3.12	3.57	14.5%	3.39	8.6%
<b>II</b>	0.50	0.55	9.0%	0.53	6.6%	3.50	4.01	16.1%	3.82	9.2%
<b>III</b>	0.45	0.49	9.3%	0.48	7.1%	2.55	2.84	11.5%	2.70	5.6%
<b>IV</b>	0.52	0.58	11.3%	0.57	8.8%	2.82	3.23	14.6%	3.04	7.7%

errors in the first and second modes are 8.8% and 9.2% respectively. Corresponding average errors over the four configurations are 7.2% and 7.8%. The rigid joint model errors are approximately 30% larger in the first mode, and 80% larger in the second mode. In all cases, the numerical model over-estimates the experimental frequencies. This is expected as there is unmodelled compliance in many bodies of the physical system. In particular, the cantilevered link assumption is suspect. However, as stated above, the agreement between predicted and measured results is very good.

The remaining error in the predicted frequencies can potentially be attributed to a number of factors. The data in Table 2.6 unfortunately does not help to isolate the cause of the errors. Differences between the errors with LAURA2 at  $0^\circ$  and LAURA2 at  $45^\circ$  (configurations I and II vs configurations III and IV) indicate problems with the LAURA model. Similarly, discrepancies between the errors of configurations I and III vs those of configurations II and IV indicate a problem with the SARA mass model.

## 2.5 Control System

The hardware and software used to control the LAURA-SARA manipulator can be divided into three categories: data processing, interface, and instrumentation. A diagram of the different components is shown in Figure 2.10. For clarity, the joint amplifiers and motors have not been included. Also excluded are the special purpose interface boards which perform several ‘mundane’ tasks for the macro-manipulator joints.

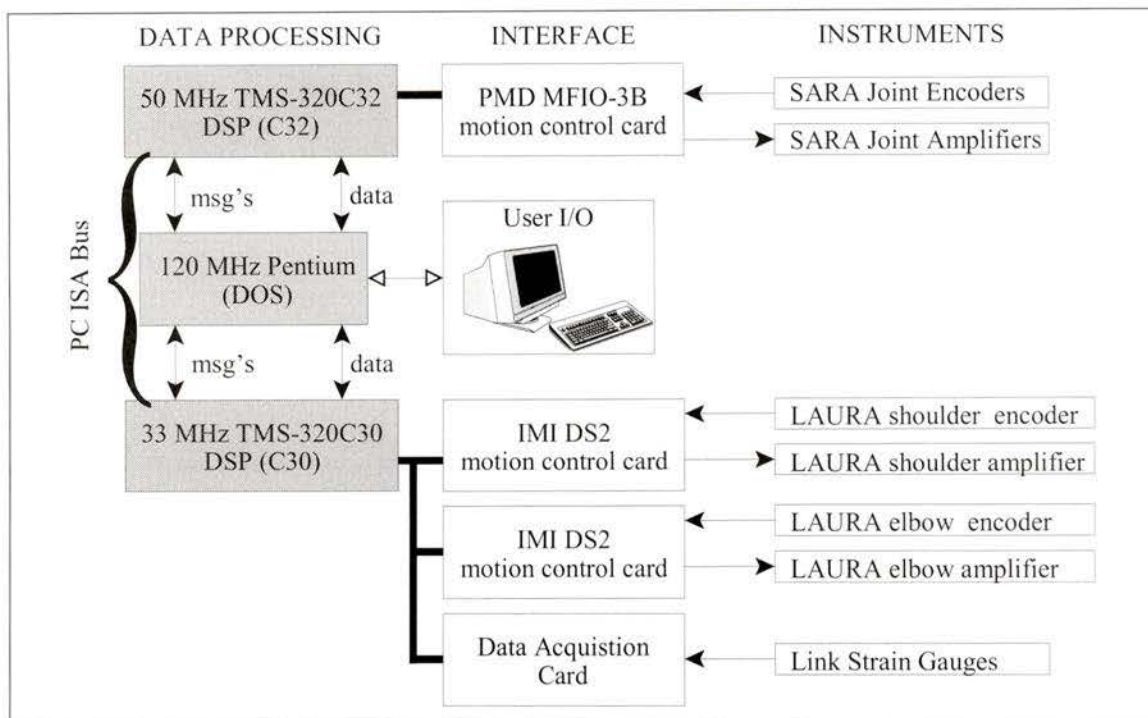


Figure 2.10: *Instrumentation and Control Components for the LAURA-SARA Manipulator*

The data-processing hardware includes a 120 MHz Pentium hosting two DSP boards: a 33 MHz TMS320-C30 system board and a 50 MHz TMS320-C32 processor board, both from Spectrum Signal Processing. All control calculations are performed on the DSP's, while the PC is responsible for the user interface, data archiving and DSP coordination.

Three motion control cards and one A/D conversion card form the interface hardware and are connected to the two DSP's through a dedicated bus called DSP-Link. Joint positions are measured with encoders on each joint and input to the DSP's through the motion control cards. The commanded torques are output to the joint amplifiers through these same cards. The flexible link deflections are measured from strain gauge bridges mounted on the links and acquired through the data acquisition card.

### 2.5.1 Software

Both the PC and DSP software is written in C, compiled, and stored on the PC. A dedicated Texas Instruments compiler is used to compile the DSP code, which is copied at runtime to

the DSP's. The user interface software runs under DOS. High level C libraries for control, data transfer, and DSP coordination tasks were written for the PC and DSP's, with special care to maintain easy portability between processors. Care was also taken to keep the number of functions which directly access the hardware to a minimum. These precautions will simplify the task of porting the code to new operating systems in the future.

PC-DSP coordination and timing is achieved through a message-based system. The message 'language' includes messages to coordinate initialization, provide status information, request data transfers, and post error messages. Although message based systems are generally less efficient than interrupts, benchmark tests have shown that the message overhead on the DSP's is less than 0.015ms per control cycle using the above mentioned libraries. Furthermore, since programs for the Windows family of operating systems (95, NT, CE) are also message based, the present control software will simplify porting from DOS to Windows in the future.

A double-buffered system is used for data transfers from the DSP to the PC. When a buffer is filled with experimental data, the DSP sends a message to the PC requesting that it copy the buffer. Meanwhile, the DSP writes data to the second buffer. Block data transfers, and the associated overhead, are thus less frequent than if data was passed with each sample period.

Benchmark tests have shown that full-matrix PD control law can be evaluated on each DSP in under 0.25ms, including data I/O and block transfers to the PC. PD control of the LAURA-SARA manipulator was therefore executed at a frequency of 4000 Hz.

### **2.5.2 Instrumentation and Data Acquisition**

Each joint is equipped with an incremental encoder to measure its position. For the HD joints of LAURA, the encoder resolution is 214400 pulses per revolution of the gearbox output, but the measurement is actually made at the motor. The effective resolution is therefore reduced by gearbox flexibility and, to a lesser extent, backlash. The SARA shoulder

encoder has a resolution of 8000 pulses/revolution, while the elbow and wrist joint positions are known to an accuracy of 10 000 pulses/revolution. Since these joints are direct-drive, the quoted values represent the true encoder resolution.

There is no direct method of measuring the joint rates. Instead, the rate is calculated by using the finite difference scheme:  $\dot{\theta} = (\theta_n - \theta_{n-1}) / (t_n - t_{n-1})$ . As commonly known, this simple method results in very noisy rate approximations. FIR and IIR filter functions have been written to smooth the calculated velocity. The above mentioned 4000 Hz sample rate can be maintained with a 50<sup>th</sup> order FIR filter, with significantly improved rate estimates.

The elastic deflections of the macro-manipulator links are measured with two strain gauge bridges on each link. In the frequency domain validation experiments discussed previously, the bridges are sampled at 4000 Hz and the data is averaged online by the DSP, typically down to 100 Hz. Oversampling of the strain gauges reduces the high frequency electrical noise in the strain gauge signals.

## Chapter 3

# Active Damping Techniques

The concept of active damping was introduced in Chapter 1 as a method of alleviating some of the difficulties of controlling flexible macro-manipulators. It is possible to use the joints of the macro-manipulator itself to perform this damping, but doing so would require high bandwidth operation, which is not often available. The micro-manipulator is, however, ideal for the task as it is designed to be small, rigid, and fast. The theory and practical implementation of two micro-manipulator active damping techniques are discussed in this chapter.

### 3.1 General Manipulator Model for Active Damping

Figure 3.1 illustrates a general model of a macro-micro manipulator used to develop the active damping schemes. The model is based on two simplifying assumptions:

1. the macro-manipulator is rigidly mounted to a fixed, or very massive, structure;
2. macro-manipulator rigid degrees of freedom are locked during active damping.

The first assumption is valid for the manipulators currently under consideration, namely the LDUA, SSRMS/SPDM, and the University of Victoria's LAURA-SARA manipulator. The second assumption is a reasonable limitation consistent with the deploy-lock-damp procedure anticipated for current macro-micro manipulators, and is also consistent with

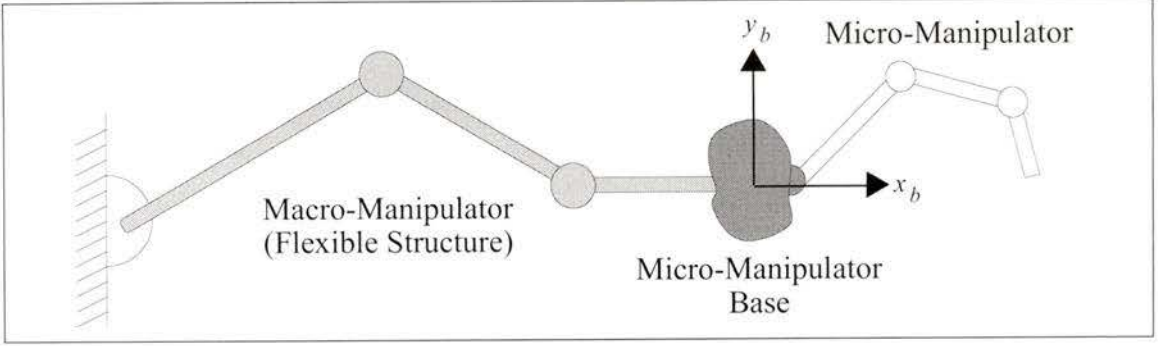


Figure 3.1: *General Manipulator Model for Development of Active Damping Algorithms*

previous research in this field (see §1.3). With its joints locked, the macro-manipulator is more aptly called a *flexible structure*.

To develop a model of a general macro-micro manipulator, the coordinates are first partitioned into elastic and rigid terms. Since the macro-manipulator joints are locked, the only rigid terms are those associated with the micro-manipulator. The elastic coordinates describe the elastic deformations of the flexible structure (macro-manipulator with joints locked) including those at intermediate nodes. A vector of generalized coordinates,  $\mathbf{q} = [\mathbf{q}_e^T, \mathbf{q}_r^T]^T$ , defines the elastic deformations ( $\mathbf{q}_e$ ) and rigid joint displacements ( $\mathbf{q}_r$ ), and  $\boldsymbol{\tau} = [\boldsymbol{\tau}_e^T, \boldsymbol{\tau}_r^T]^T$  is the corresponding vector of generalized forces. No external forces are applied to the system, so  $\boldsymbol{\tau}_e$  is always equal to  $\mathbf{0}$ .

The full non-linear equations of motion for a general macro-micro manipulator can be derived using the Lagrangian approach. Throughout this work  $\mathbf{q}$  and  $\dot{\mathbf{q}}$  are assumed small, so the equations are linearized by dropping the centrifugal and Coriolis terms. The resulting linear equations of motion are

$$\mathbf{M}(\bar{\mathbf{q}})\ddot{\mathbf{q}} + \mathbf{K}\mathbf{q} = \boldsymbol{\tau}, \quad (3.1)$$

where  $\mathbf{M}(\bar{\mathbf{q}})$  is the manipulator mass matrix at a nominal configuration  $\bar{\mathbf{q}}$ , and  $\mathbf{K}$  is the stiffness matrix of the flexible structure, which are partitioned as:

$$\mathbf{M}(\mathbf{q}) = \begin{bmatrix} \mathbf{M}_{ee} & \mathbf{M}_{er} \\ \mathbf{M}_{er}^T & \mathbf{M}_{rr} \end{bmatrix} \quad \text{and} \quad \mathbf{K} = \begin{bmatrix} \mathbf{K}_{ee} & \mathbf{0} \\ \mathbf{0} & \mathbf{0} \end{bmatrix} \quad (3.2)$$

There are two differences between equation (3.1) above and equation (2.4) in §2.3.3. First, the  $\mathbf{P}\mathbf{q}$  term from the left hand side of equation (2.4) is incorporated into  $\boldsymbol{\tau}$  on the right hand side of equation (3.1). Second, since the macro-manipulator joints are locked and the micro-manipulator structure is rigid,  $\mathbf{K}$  in equation (3.1) is not a function of the coordinate vector  $\bar{\mathbf{q}}$ .

After macro-manipulator deployment is complete, the only control inputs to the system are the micro-manipulator joint torques,  $\boldsymbol{\tau}_r$ . The goal of active damping, then, is to control the micro-manipulator motion through  $\boldsymbol{\tau}_r$  in an effort to reduce the elastic vibrations as defined by  $\mathbf{q}_e$  and  $\dot{\mathbf{q}}_e$ .

### 3.2 Cartesian Space vs Joint Space Derivative Control

The concept of active damping can perhaps best be explained as an extension of the passive frictional damping inherent to all physical systems. Frictional forces always oppose the motion of the point of application. Since the applied power  $P$  is defined as the inner product of force  $\mathbf{f}$  and velocity  $\mathbf{v}$ , the frictional forces by definition dissipate energy. That is,  $P = \mathbf{f} \cdot \mathbf{v} < 0$ . At any time  $T$ , the total work done by the frictional forces on a vibrating system is

$$W = \int_0^T P(t) dt = \int_0^T \mathbf{f}(t) \cdot \mathbf{v}(t) dt < 0 \forall T, \quad (3.3)$$

thus demonstrating that friction removes energy from the elastic system, or damps the vibration.

With active damping, the rate of energy dissipation may be increased, but the principle is the same. Negative work is done on the system by applying forces via the micro-manipulator joint torques,  $\boldsymbol{\tau}_r$ , to resist the motion of the point of application. The instantaneous power input to the manipulator is

$$P = \mathbf{f} \cdot \mathbf{v} = \boldsymbol{\tau} \cdot \dot{\mathbf{q}} = \boldsymbol{\tau}_r \cdot \dot{\mathbf{q}}_r, \quad (3.4)$$

since  $\boldsymbol{\tau}_e = \mathbf{0}$ . The micro-manipulator joint torques,  $\boldsymbol{\tau}_r$ , are actively controlled and can be functions of any of the generalized coordinates and their derivatives, or any other useful parameter.

*Cartesian space derivative* (CSD) control and *joint space derivative* (JSD) control are defined by the variables used to calculate  $\boldsymbol{\tau}_r$ . In the former, the only arguments are the state of the flexible structure,  $\mathbf{q}_e$ , and in the latter only the state of the micro-manipulator joints,  $\mathbf{q}_r$ , is used:

$$\begin{aligned} \text{Cartesian space derivative control: } \boldsymbol{\tau}_r &= \boldsymbol{\tau}_r(\mathbf{q}_e, \dot{\mathbf{q}}_e, \ddot{\mathbf{q}}_e, \dots) \\ \text{Joint space derivative control: } \boldsymbol{\tau}_r &= \boldsymbol{\tau}_r(\mathbf{q}_r, \dot{\mathbf{q}}_r, \ddot{\mathbf{q}}_r, \dots) \end{aligned} \tag{3.5}$$

The term ‘joint space’ is self explanatory, but ‘cartesian space’ requires some explanation. The elastic state of the macro-manipulator affects the micro-manipulator by moving its base in Cartesian space. With the right joint torques, the micro-manipulator can apply a wrench to its base which resists this motion. Alternatively, with joint space derivative control, the torque at each joint is applied to resist the motion of that joint directly. In both cases, the term *derivative* is used since the rate of energy dissipation is a function of the first derivative of the generalized coordinates.

JSD control typically requires only position and rate sensors on the micro-manipulator joints. If rate sensors are not available, they can be approximated with an observer implemented in the control software [4, 5]. This is a distinct advantage over CSD control, which requires additional sensing for the elastic state of the flexible structure. The disadvantage of JSD control is that damping is possible only when the vibrations are sufficiently large to overcome joint friction and excite motions in the micro-manipulator [2].

Both active damping techniques investigated in this work, Pseudo-Passive Energy Dissipation and Impedance Matching, are examples of JSD control. Furthermore, PD control is used for both methods, so that the only difference in implementation is the off-line calculation of the gain matrices used in the control law. Examples of CSD and hybrid

control methods are found in the works of Sharf [15, 16], the Pacific Northwest Laboratory group led by Trudnowski [10, 11, 24], and the Georgia Institute of Technology group led by Book [1, 2, 3, 9].

### 3.3 Pseudo-Passive Energy Dissipation

Pseudo-Passive Energy Dissipation, or P-PED, was introduced as an active damping method by Torres in his Ph.D. thesis [21]. The method was not originally intended for macro-micro manipulators, but rather for ‘long reach space manipulators’ with negligible mass and no internal degrees of freedom. In the original work and an additional paper [23], the performance of the algorithm is demonstrated experimentally on a simple consisting of a single flexible link with a two-DOF rigid planar micro-manipulator. Numerical simulation results on a more complex system are also presented in the latter.

#### 3.3.1 Model

The model used to develop P-PED is a simplified case of the general model of §3.1 with negligible macro-manipulator mass. This is a troublesome simplification for macro-micro manipulators. As implied by the name, the flexible macro-manipulator is considerably larger and more massive than the micro-manipulator. Extensions to the original theory were therefore required for experimental studies and are discussed in §3.3.4.

Neglecting the mass of the flexible structure and any internal degrees of freedom, the linear equations of motion used to develop P-PED are:

$$\mathbf{M}(\bar{\mathbf{q}})\ddot{\mathbf{q}} + \mathbf{K}\mathbf{q} = \boldsymbol{\tau}, \quad (3.6)$$

where the vector  $\mathbf{q} = [\mathbf{q}_b^T, \mathbf{q}_r^T]^T$  here includes only the elastic deflections of the micro-manipulator base and the micro-manipulator joint displacements. In the general model,  $\mathbf{q}$  also included elastic deflections at internal nodes of the flexible structure. The mass and

stiffness matrices are partitioned as:

$$M(\bar{q}) = \begin{bmatrix} M_b & M_{br} \\ M_{br}^T & M_{rr} \end{bmatrix} \quad \text{and} \quad K = \begin{bmatrix} K_b & \mathbf{0} \\ \mathbf{0} & \mathbf{0} \end{bmatrix} \quad (3.7)$$

Here, the submatrices  $M_b$  and  $K_b$  are the mass and stiffness matrices associated with the micro-manipulator base degrees of freedom,  $q_b$ . These are special cases of the more general  $M_{ee}$  and  $K_{ee}$  matrices from §3.1.

### 3.3.2 Model Reduction to Component Systems

The first step in calculating the P-PED joint gains is to reduce the system to a combination of very simple mass-spring-damper systems. This process is illustrated in Figure 3.2 for a planar manipulator. Optimal gains are then calculated for the mass-spring-damper systems and converted back to joint gains for the complete micro-manipulator. This procedure is described in more detail below.

Using the virtual manipulator concept introduced by Vafa [25], the micro-manipulator is reduced to a massless kinematic chain with a discrete mass at its tip. However, the virtual manipulator concept was originally developed for free-floating manipulators, so care must be taken when applying this technique to a fixed-base system. In particular, the stiffness of the flexible structure (macro-manipulator) must be low and the mass of the manipulator,  $m_r$ , must be large relative to the mass of its base,  $m_b$ .

The above mentioned discrete tip mass is equal to the total mass of the real manipulator and is located at the real manipulator's centre of mass. All virtual manipulator links have constant length and are parallel to the corresponding links of the real manipulator. For the planar 3-DOF example in Figure 3.2, the lengths of the virtual manipulator links are:

$$L_{v1} = \frac{m_1 r_1 + (m_2 + m_3)L_1}{m_1 + m_2 + m_3} \quad (3.8)$$

$$L_{v2} = \frac{m_2 r_2 + m_3 L_2}{m_1 + m_2 + m_3} \quad (3.9)$$

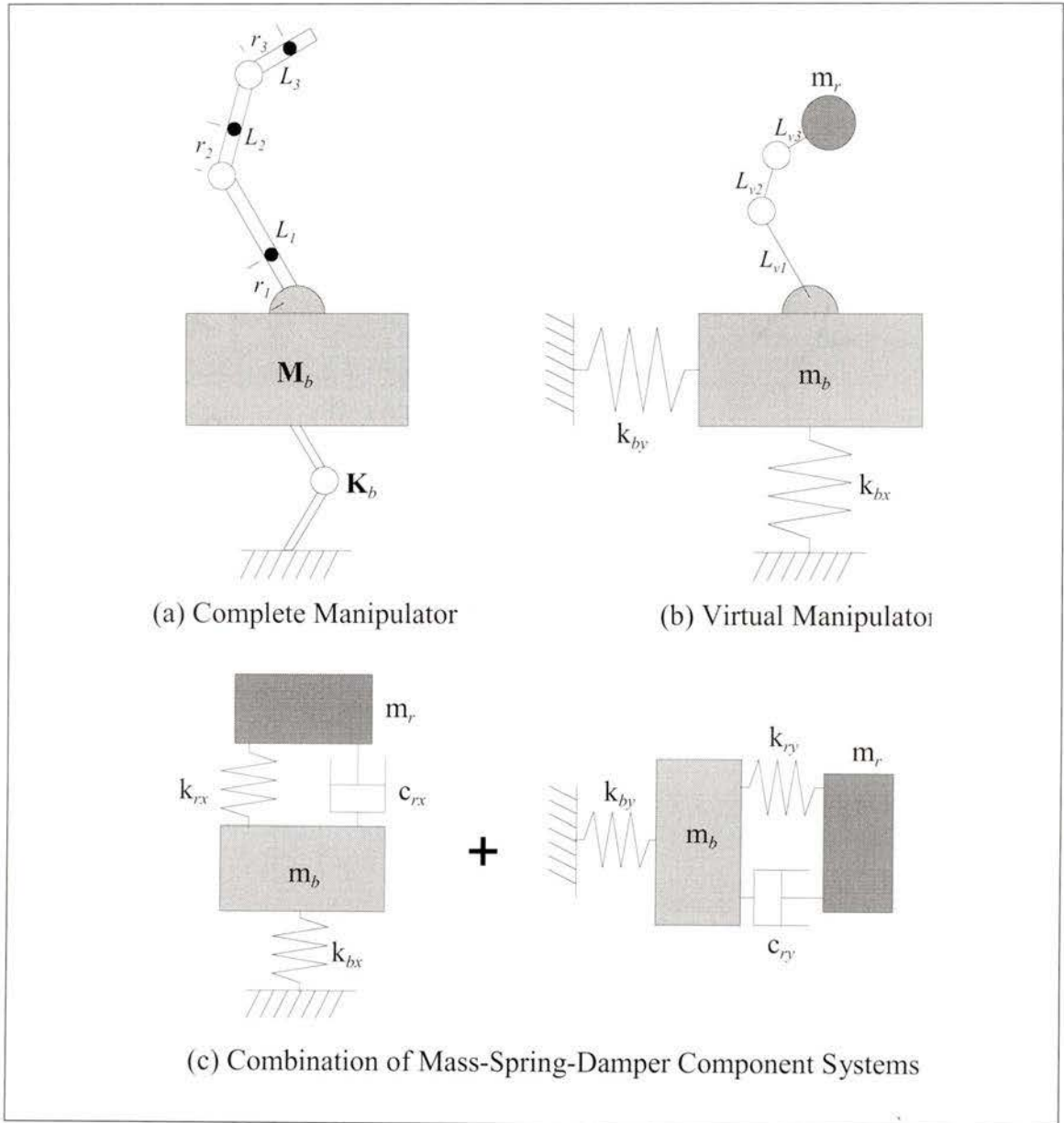


Figure 3.2: Manipulator Reduction to Mass-Spring-Damper Component Systems for P-PED Gains Calculation

$$L_{v3} = \frac{m_3 r_3}{m_1 + m_2 + m_3} \quad (3.10)$$

where  $m_i$  is the mass of the  $i^{\text{th}}$  body of the micro-manipulator,  $r_i$  is the length of a vector from the  $i^{\text{th}}$  body coordinate frame origin to its centre of mass, and  $L_i$  is the length of a vector between body coordinate frames  $i$  and  $i + 1$ . It is assumed that the  $i^{\text{th}}$  body centre of mass lies on a plane defined by the axes of rotation of bodies  $i$  and  $i + 1$ .

The virtual manipulator Jacobian is identical in form to that of the real manipulator, with virtual link lengths substituted for the real link lengths. The virtual manipulator Jacobian for the planar example of Figure 3.2b is

$$\mathbf{J}_{cm} = \left[ \begin{array}{cc} \left( \begin{array}{c} -L_{v1} \sin(\theta_1) - L_{v2} \sin(\theta_{12}) \\ -L_{v3} \sin(\theta_{123}) \end{array} \right) & \left( \begin{array}{c} -L_{v2} \sin(\theta_{12}) \\ -L_{v3} \sin(\theta_{123}) \end{array} \right) & -L_{v3} \sin(\theta_{123}) \\ \left( \begin{array}{c} L_{v1} \cos(\theta_1) + L_{v2} \cos(\theta_{12}) \\ +L_{v3} \cos(\theta_{123}) \end{array} \right) & \left( \begin{array}{c} L_{v2} \cos(\theta_{12}) \\ +L_{v3} \cos(\theta_{123}) \end{array} \right) & L_{v3} \cos(\theta_{123}) \end{array} \right] \quad (3.11)$$

with  $\theta_{ij}$  is the sum of the angles of micro-manipulator joints  $i$  and  $j$ . That is,  $\theta_{ij} = \theta_i + \theta_j$ .

For any manipulator, the tip Jacobian matrix or its transpose relates the tip wrench to the joint forces and torques, and the joint rates to the tip velocity. In the limiting case of small joint motions about a nominal configuration, the Jacobian also relates the infinitesimal joint rotations to the infinitesimal tip displacement. The virtual manipulator is no exception, but the ‘tip’ of the virtual manipulator is the centre of mass of the real manipulator. The virtual manipulator Jacobian is therefore denoted by  $\mathbf{J}_{cm}$ . Equations (3.12) through (3.14) define the pertinent relationships for the virtual manipulator, with  $\mathbf{X}$  defined as the displacement of the centre of mass from a nominal position.

$$\boldsymbol{\tau}_r = \mathbf{J}_{cm}^T \mathbf{F}_{cm} \quad (3.12)$$

$$\dot{\mathbf{X}}_{cm} = \mathbf{J}_{cm} \dot{\mathbf{q}}_r \quad (3.13)$$

$$\delta \mathbf{X}_{cm} = \mathbf{J}_{cm} \delta \mathbf{q}_r \quad (3.14)$$

Consistent with Torres’ presentation and the limitations of the virtual manipulator, the *torques* acting on the centre of mass are not considered. Equation (3.12) relates only the linear forces at the micro-manipulator centre of mass to the micro-manipulator joint torques.

If the translational degrees of freedom of the flexible structure are decoupled, and ro-

tation is neglected, the virtual manipulator is easily replaced by a combination of two-DOF mass-spring-damper systems, as shown in Figure 3.2c. When the translational terms are not decoupled, the general method of decoupling them presented in §3.3.4 must be employed.

### 3.3.3 P-PED Joint Gains

For each mass-spring-damper system of Figure 3.2, optimal spring and damper gains must be calculated. The symbols  $k_{rx}$  and  $k_{ry}$  denote the spring gains for the two systems, and  $c_{rx}$  and  $c_{ry}$  are the corresponding damper gains. The mass-spring-damper systems are identical to damped dynamic vibration absorbers, which are often used to remove resonance peaks from rotating machinery [14]. However, the excitation of the two systems is very different. Rotating machinery is subject to continuous forcing at a fixed frequency, whereas the micro-manipulator base vibrates freely after an initial disturbance. The well established theory of damped dynamic vibration absorbers is therefore not applicable.

Torres developed an iterative root-locus procedure for computing the optimal spring and damper gains, which was found to converge very rapidly. Each mass-spring-damper system is considered separately when calculating the gains. As part of this research, a direct analytical solution was derived, and is presented in Appendix B. The analytical solution has revealed that each mass-spring-damper can be critically damped when  $m_r = 4m_b$ . If  $m_r < 4m_b$  the system is under-damped, and when  $m_r > 4m_b$  the system is over-damped.

Finally, the joint gain matrices are calculated from the  $k_r, c_r$  pairs for each translational direction. In the general spatial case, the forces acting on the micro-manipulator centre of mass are:

$$\begin{aligned} f_{x,cm} &= k_{rx}x_{e,cm} + c_{rx}\dot{x}_{e,cm} \\ f_{y,cm} &= k_{ry}y_{e,cm} + c_{ry}\dot{y}_{e,cm} \\ f_{z,cm} &= k_{rz}z_{e,cm} + c_{rz}\dot{z}_{e,cm} \end{aligned} \tag{3.15}$$

In the above,  $x_{e,cm} = x_{eq,cm} - x_{cm}$  is the deviation of the mass  $m_r$  from its equilibrium position in the  $x$ -direction, and  $\dot{x}_{e,cm} = -\dot{x}_{cm}$ . Equivalent equations apply for the  $y$ - and

$z$ - directions. Rewriting in matrix form gives:

$$\mathbf{F}_{cm} = \mathbf{K}_r \mathbf{X}_{e,cm} + \mathbf{C}_r \dot{\mathbf{X}}_{e,cm}, \quad (3.16)$$

where

$$\mathbf{K}_r = \begin{bmatrix} k_{rx} & 0 & 0 \\ 0 & k_{ry} & 0 \\ 0 & 0 & k_{rz} \end{bmatrix} \quad (3.17)$$

$$\mathbf{C}_r = \begin{bmatrix} c_{rx} & 0 & 0 \\ 0 & c_{ry} & 0 \\ 0 & 0 & c_{rz} \end{bmatrix}$$

Combining equations (3.12) and (3.16) yields

$$\boldsymbol{\tau}_r = \mathbf{J}_{cm}^T (\mathbf{K}_r \mathbf{X}_{e,cm} + \mathbf{C}_r \dot{\mathbf{X}}_{e,cm}) \quad (3.18)$$

Finally, the micro-manipulator joint torques are found as functions of the micro-manipulator joint state by combining equations (3.18), (3.13), and (3.14):

$$\boldsymbol{\tau}_r = \mathbf{P}_{P-PED} \mathbf{q}_r + \mathbf{D}_{P-PED} \dot{\mathbf{q}}_r, \quad (3.19)$$

where,

$$\mathbf{P}_{P-PED} = \mathbf{J}_{cm}^T \mathbf{K}_r \mathbf{J}_{cm} \quad (3.20)$$

$$\mathbf{D}_{P-PED} = \mathbf{J}_{cm}^T \mathbf{C}_r \mathbf{J}_{cm}$$

In general,  $\mathbf{P}_{P-PED}$  and  $\mathbf{D}_{P-PED}$  are full matrices and hence, the method can not be properly implemented on manipulators with only local PD control. Torres states that for such manipulators, the diagonal elements of  $\mathbf{P}_{P-PED}$  and  $\mathbf{D}_{P-PED}$  can be used with good results.

### 3.3.4 Implementation

Unfortunately, a number of problems arise when attempting to implement P-PED experimentally. This section is devoted to the discussion and resolution of foreseen problems. Most of these problems arose during the experimental work presented in Chapter 6.

#### Significant Macro-Manipulator Mass

When the P-PED method was derived, it was assumed that the mass of the flexible supporting structure, or the macro-manipulator in this work, was small relative to the mass of the micro-manipulator and its base. This is rarely the case in practice, and is certainly not true for the macro-micro manipulator examples discussed in Chapter 1, or the LAURA-SARA manipulator presented in Chapter 2.

To overcome this limitation, Guyan reduction [6] has been used to lump the mass of the macro-manipulator with that of the micro-manipulator base. The method is described in Appendix C with detailed results for reductions of the complete LAURA-SARA manipulator. However, only the micro-manipulator base is included in the P-PED Guyan reduction to calculate  $m_{bx}$  and  $m_{by}$  and ultimately the spring and damper gains. The micro-manipulator itself is considered separately. Table 3.1 summarizes the numerical modes of the LAURA manipulator with the SARA base at its distal end, expressed in the SARA base frame. It is clear from these results that little error is introduced by applying Guyan reduction.

Table 3.1: *Modal Analysis of Complete and Reduced Models of LAURA Manipulator and SARA Base: Frequencies and Mode Shapes*

Mode	Model	LAURA2 at -15 degrees				LAURA2 at 60 degrees			
		Freq (Hz)	$x_{S0}$	$y_{S0}$	$\theta_{S0}$	Freq (Hz)	$x_{S0}$	$y_{S0}$	$\theta_{S0}$
1	Complete	0.7073	-0.0516	0.7142	0.6981	0.7744	0.1794	0.6519	0.7368
	Reduced	0.7073	-0.0516	0.7142	0.6981	0.7744	0.1794	0.6519	0.7368
2	Complete	3.8734	-0.0673	0.1782	0.9817	3.1197	-0.2353	0.2651	0.9351
	Reduced	3.8912	-0.0671	0.1774	0.9818	3.1239	-0.2350	0.2648	0.9352

### Coupled Translational Degrees of Freedom

In §3.3.2, the flexible supporting structure was simplified by dropping the rotational degrees of freedom and representing the translational dynamics as a combination of orthogonal mass-spring-damper systems. For a simple flexible structure, such as a cantilevered flexible link, this process is straight forward because the translational motions are decoupled. In the general case, however, the translational motions are coupled and additional calculations are required, as described below.

The unforced system dynamics for a general flexible structure with a rigid body (the micro-manipulator base) at its tip are partitioned as:

$$\begin{bmatrix} \mathbf{M}_{b_{TT}} & \mathbf{M}_{b_{TR}} \\ \mathbf{M}_{b_{TR}}^T & \mathbf{M}_{b_{RR}} \end{bmatrix} \begin{bmatrix} \ddot{\mathbf{q}}_{b_T} \\ \ddot{\mathbf{q}}_{b_R} \end{bmatrix} + \begin{bmatrix} \mathbf{K}_{b_{TT}} & \mathbf{K}_{b_{TR}} \\ \mathbf{K}_{b_{TR}}^T & \mathbf{K}_{b_{RR}} \end{bmatrix} \begin{bmatrix} \mathbf{q}_{b_T} \\ \mathbf{q}_{b_R} \end{bmatrix} = \mathbf{0}, \quad (3.21)$$

where  $\mathbf{q}_{b_T}$  and  $\mathbf{q}_{b_R}$  define the translational and rotational elastic deflections respectively and the mass and stiffness terms are defined correspondingly. The rotational degrees of freedom are neglected when the system is reduced to a virtual manipulator. The remaining translational system is described by:

$$\mathbf{M}_{b_{TT}} \ddot{\mathbf{q}}_{b_T} + \mathbf{K}_{b_{TT}} \mathbf{q}_{b_T} = \mathbf{0}, \quad (3.22)$$

The modal matrix,  $\mathbf{Z}$ , is now used to decouple the translational terms [20], leading to the following diagonal mass and stiffness matrices:

$$\begin{aligned} \hat{\mathbf{M}}_b &= \mathbf{Z}^T \mathbf{M}_{b_{TT}} \mathbf{Z} \\ \hat{\mathbf{K}}_b &= \mathbf{Z}^T \mathbf{K}_{b_{TT}} \mathbf{Z} \end{aligned} \quad (3.23)$$

The diagonal elements of  $\hat{\mathbf{M}}_b$  and  $\hat{\mathbf{K}}_b$  represent the mass and stiffness along the principle directions of the system. Since only translational terms are used, the principle directions are entirely translational. These diagonal elements are substituted for the  $m_b$  and  $k_b$  terms

to calculate the optimum spring and damper gains for the mass-spring-damper systems of Figure 3.2c.

The spring and damper gains are assembled into diagonal matrices,  $\hat{\mathbf{K}}_r$  and  $\hat{\mathbf{C}}_r$ , which are then transformed back to the body coordinate frame:

$$\begin{aligned}\mathbf{K}_r &= \mathbf{Z}^{-T} \hat{\mathbf{K}}_r \mathbf{Z}^{-1} \\ \mathbf{C}_r &= \mathbf{Z}^{-T} \hat{\mathbf{C}}_r \mathbf{Z}^{-1}\end{aligned}\tag{3.24}$$

The matrices  $\mathbf{K}_r$  and  $\mathbf{C}_r$ , although not generally diagonal, can be directly substituted into equation (3.20) to calculate  $\mathbf{P}_{P-PED}$  and  $\mathbf{D}_{P-PED}$ .

### Instability with Full P-PED Gain Matrices

Experience has shown that instability is a problem when using the full  $\mathbf{P}_{P-PED}$  and  $\mathbf{D}_{P-PED}$  gain matrices for experiments. Joint friction and possibly other non-linearities are the suspected cause of the experimental instability. Torque feedback at each joint would likely lessen the problem. However, since torque feedback is not available in SARA, instability was avoided by using only the diagonal elements of the complete gain matrices. This was suggested by Torres *et al* for manipulators with only local PD control, and has been used in their published works [22, 23].

### Poorly Conditioned Base Stiffness Matrix

The translational stiffness elements of flexible structures can differ by orders of magnitude. Consider for example the flexible links of LAURA, which are described in Chapter 2. With units of N, m, and radians, the stiffness matrix for one of these links is

$$\mathbf{K}_{link} = \begin{bmatrix} k_{xx} & 0 & 0 \\ 0 & k_{yy} & k_{y\theta} \\ 0 & k_{y\theta} & k_{\theta\theta} \end{bmatrix} = \begin{bmatrix} 4.448e7 & 0 & 0 \\ 0 & 7.175e3 & -1.794e3 \\ 0 & -1.794e3 & 5.979e2 \end{bmatrix}\tag{3.25}$$

Note that  $k_{xx}$ , the axial link stiffness, is almost 4 orders of magnitude greater than the transverse stiffness,  $k_{yy}$ . As a result,  $k_{rx}$  and  $c_{rx}$  will be much larger than  $k_{ry}$  and  $c_{ry}$ , and the  $\mathbf{P}_{P-PED}$  and  $\mathbf{D}_{P-PED}$  matrices will be dominated by these larger terms. Theoretically this is not a problem when the full  $\mathbf{P}_{P-PED}$  and  $\mathbf{D}_{P-PED}$  matrices are used. In practice, however, exceedingly large gains lead to torque saturation and instability. If diagonal gain matrices are used, the micro-manipulator, although stable, will be nearly rigid in most configurations, and therefore ineffective at damping the dominant low frequency vibrations.

The simple solution is to drop any exceedingly stiff degrees of freedom. For the case of a single flexible link, it is easy to justify neglecting the axial DOF. However, since the degree of freedom corresponding to  $k_{bx}$  is dropped,  $k_{rx}$  is not calculated and therefore effectively set to zero. The result is that in certain micro-manipulator configurations  $\mathbf{P}_{P-PED}$  and  $\mathbf{D}_{P-PED}$  are uniformly zero, and the micro-manipulator motion is uncontrolled. Another solution is to set the stiffness of the stiffer direction,  $k_{bx}$ , equal to that of the more compliant direction,  $k_{by}$ , for the purpose of calculating the P-PED gain matrices. These two options are referred to as P-PED<sub>A</sub> and P-PED<sub>B</sub> in Chapter 5, and the damping performance between the two methods is shown to differ significantly.

Experiments were performed with the LAURA elbow bent to  $-15^\circ$  and  $+60^\circ$ . In these configurations, the difference between the translational stiffnesses is not as large, and hence, it is difficult to identify when to neglect or modify a DOF. Therefore, for the experimental work, both translational degrees of freedom ( $x$ - and  $y$ -) are used to calculate  $\mathbf{P}_{P-PED}$  and  $\mathbf{D}_{P-PED}$ .

### 3.4 Impedance Matching

The Impedance Matching (IM) method of JSD control was developed as a simple alternative to P-PED. The latter suffers from a number of modelling assumptions and implementation concerns which complicate its application to macro-micro manipulators. One of the primary goals in developing IM was to avoid these pitfalls.

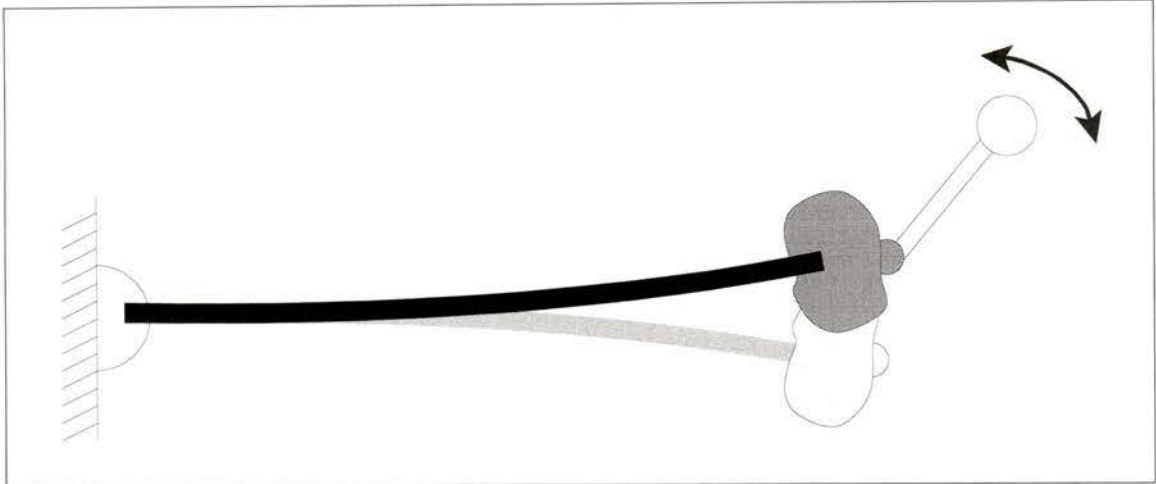


Figure 3.3: *Simple Planar Macro-Micro Manipulator for Derivation of Impedance Matching*

### 3.4.1 Derivation

A simple planar macro-micro manipulator is illustrated in Figure 3.3. For the purpose of developing the method, macro-manipulator vibration confined to the dominant mode at frequency  $\tilde{\omega}_e$  is considered. Here the dominant mode is defined from the pole locations with the rigid micro-manipulator DOF's locked. The pole which lies closest to the real axis is dominant [5]. Alternatively, the dominant frequency can be measured on the assembled manipulator.

The micro-manipulator is controlled with a PD control law to ensure that energy will be dissipated from the macro-manipulator, as explained in §3.2. It is assumed that the macro-manipulator continues to vibrate at the original frequency,  $\tilde{\omega}_e$ , while the micro-manipulator dissipates the elastic energy. If the rate of dissipation is small compared to the initial elastic energy, the amplitude of vibration can also be assumed constant. These assumptions are valid for a micro-manipulator which is much smaller than the macro-manipulator, as would generally be expected.

Like the model used to derive P-PED, this system is similar to a damped dynamic vibration absorber. The difference with Impedance Matching is that the micro-manipulator is subject to a moving base rather than an oscillating force.

The motion of a single DOF system like the micro-manipulator subjected to a sinusoidal

base motion at frequency  $\tilde{\omega}_e$  is well known [14, 20]. If the natural frequency of the micro-manipulator in isolation is  $\omega_r$  and its damping ratio is  $\zeta$ , the steady-state motion of the micro-manipulator,  $\theta_r$ , is described by:

$$\theta_r = \Theta \sin(\tilde{\omega}_e t - \phi), \quad (3.26)$$

and,

$$\Theta = \left[ \frac{\mu Y}{\sqrt{\mu^2(\mu^2 - 1)^2 + 4\zeta^2}} \right] \quad (3.27)$$

where  $Y$  is a constant related to the magnitude and direction of base motion, and  $\mu = \tilde{\omega}_e/\omega_r$  is the frequency ratio.

By tuning the joint proportional and derivative gains,  $p$  and  $d$ , the rate of energy dissipation,  $P$ , can be maximized. At any instant,

$$\begin{aligned} P &= -\tau \dot{\theta}_r \\ &= (p\theta_r + d\dot{\theta}_r)\dot{\theta}_r \\ &= \Theta^2 [p \sin(\tilde{\omega}_e t - \phi) \cos(\tilde{\omega}_e t - \phi) + d \cos^2(\tilde{\omega}_e t - \phi)] \end{aligned} \quad (3.28)$$

When integrated over time, the proportional gain term  $p \sin(\tilde{\omega}_e t - \phi) \cos(\tilde{\omega}_e t - \phi)$  goes to zero. The goal then is to maximize the energy dissipated due to the derivative gain,  $P_d = \Theta^2 [d \cos^2(\tilde{\omega}_e t - \phi)]$ , which is expanded as

$$P_d = (2J\tilde{\omega}_e^3 Y^2) \left[ \frac{\mu\zeta}{\mu^2(\mu^2 - 1)^2 + 4\zeta^2} \right] \cos^2(\tilde{\omega}_e t - \phi) \quad (3.29)$$

where the inertia of the single micro-manipulator link is  $J$ ,  $d = 2\zeta\sqrt{Jp}$ , and  $\omega_r = \sqrt{p/J}$ .

Since  $\cos^2(\tilde{\omega}_e t - \phi)$  is always positive and  $(2J\tilde{\omega}_e^3 Y^2)$  is a constant, the optimal values of  $p$  and  $d$  are determined by maximizing the objective function

$$g(\mu, \zeta) = \frac{\mu\zeta}{\mu^2(\mu^2 - 1)^2 + 4\zeta^2} \quad (3.30)$$

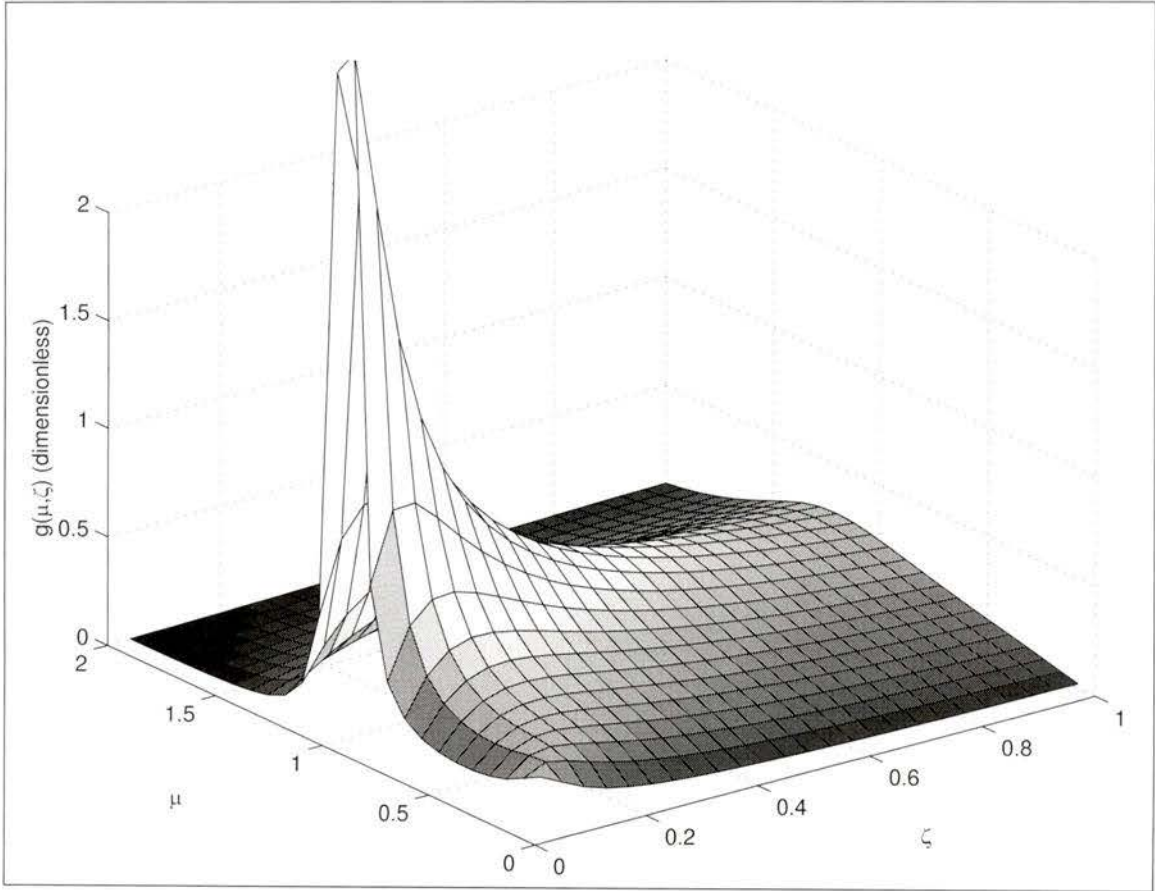


Figure 3.4: *Objective Function  $g(\mu, \zeta)$  for Calculating Optimum Impedance Matching Joint Gains*

In the special case of  $\mu^2 = 1$  and  $\zeta \rightarrow 0^+$ ,  $g(\mu, \zeta)$  approaches infinity. This special case describes a nearly undamped oscillator forced at resonance. From (3.26) and (3.27), it is clear that the motion of the micro-manipulator in this case also approaches infinity – an undesirable condition for any physical system. Peak damping performance must therefore be traded off against manipulator motion constraints.

Figure 3.4 displays a plot of  $g(\mu, \zeta)$  over the domain of reasonable values for  $\mu$  and  $\zeta$ . Note that for any value of  $\zeta$ ,  $g(\mu, \zeta)$  is maximized with  $\mu \simeq 1$ . For simplicity, then,  $\mu$  is set to 1 and  $\zeta$  is made as small as possible within the limitations of reasonable micro-manipulator joint displacements. The joint gains  $p$  and  $d$  are then calculated as follows:

$$p = \frac{J\tilde{\omega}_e^2}{\mu^2} = J\tilde{\omega}_e^2 \quad \text{and} \quad d = 2\zeta\sqrt{Jp} = 2\zeta J\tilde{\omega}_e \quad (3.31)$$

To this point the optimum gains for a joint forced at a single frequency,  $\tilde{\omega}_e$ , have been developed. The free vibration of a real macro-manipulator is a superposition of vibrations at each modal frequency. In practice, however, the vibration is dominated by the first mode for the following reasons:

- deployment maneuvers generally follow slow trajectories and therefore excite only the low modes of vibration;
- micro-manipulator joint motions, although high-bandwidth, only directly affect the tip of the macro-manipulator and therefore primarily excite the first cantilevered-mode;
- structural damping inherent to all physical systems tends to damp high frequency modes in less time than low frequency modes;
- high frequency modes typically involve motions in the stiff macro-manipulator directions, with the result that the corresponding deflections are small.

For these reasons,  $\tilde{\omega}_e$  should generally be set equal to the first macro-manipulator modal frequency.

The above procedure can be extended to a general  $n$ -DOF micro-manipulator by simply substituting the micro-manipulator stiffness, damping, and mass *matrices* for  $p$ ,  $d$ , and  $J$  in equation (3.31).

$$\begin{aligned} \mathbf{P}_{IM} &= \mathbf{M}_{rr} \omega_e^2 \\ \mathbf{D}_{IM} &= 2\zeta \mathbf{M}_{rr} \omega_e \end{aligned} \tag{3.32}$$

The closed-loop frequencies of the micro-manipulator when using the gain matrices  $\mathbf{P}_{IM}$  and  $\mathbf{D}_{IM}$  are all tuned to  $\tilde{\omega}_e$ . Unfortunately, as with the full P-PED gain matrices, the full  $\mathbf{P}_{IM}$  and  $\mathbf{D}_{IM}$  matrices often lead to instability. Once again, it is expected that joint torque feedback would alleviate the instability problems. A practical solution for SARA is presented in the following section.

### 3.4.2 Implementation

Unlike P-PED, a detailed macro-manipulator model is not required to implement the Impedance Matching algorithm. In fact, the only required information is the first modal frequency, which can be measured if a model is not available.

The single significant problem which arose when implementing IM on the LAURA-SARA manipulator was instability when using the full gain matrices. Alternative gain matrices with a diagonal structure were therefore required, and these are developed below. Note that it is not appropriate to simply extract the diagonal elements of the full gain matrices, as the natural frequencies of the micro-manipulator would not be conserved.

The following procedure can be applied only to planar micro-manipulators with two revolute degrees of freedom. The SARA wrist joint was locked with a stiff proportional gain for the IM experiments so that SARA would fit this criteria. Locking the wrist joint has very little effect on the results since its output inertia is very small.

Without full gain matrices, it is impossible to tune all SARA modes to a single frequency. Instead, SARA was tuned to two separate frequencies,  $\tilde{\omega}_{e1}$  and  $\tilde{\omega}_{e2}$ , equal to the first two modal frequencies of the LAURA-SARA manipulator as calculated with SARA locked. In Chapter 2, it was found that the model consistently over-estimated the modal frequencies. The model frequencies were therefore reduced by 7% to generate  $\tilde{\omega}_{e1}$  and  $\tilde{\omega}_{e2}$ .

The objective of this alternative derivation is to choose the diagonal elements of the joint proportional gain matrix,

$$\mathbf{P}_{IM} = \begin{bmatrix} p_1 & 0 \\ 0 & p_2 \end{bmatrix}, \quad (3.33)$$

so that the two modal frequencies of the micro-manipulator are equal to  $\tilde{\omega}_{e1}$  and  $\tilde{\omega}_{e2}$ . The micro-manipulator mass matrix,  $\mathbf{M}_{rr}$ , is partitioned as

$$\mathbf{M}_{rr} = \begin{bmatrix} m_{11} & m_{12} \\ m_{12} & m_{22} \end{bmatrix}, \quad (3.34)$$

and the inverse of  $\mathbf{M}_{rr}$  is

$$\mathbf{N} = \begin{bmatrix} n_{11} & n_{12} \\ n_{12} & n_{22} \end{bmatrix} \quad (3.35)$$

The closed-loop characteristic equation of the micro-manipulator is:

$$\lambda^2 - (n_{11}p_1 + n_{22}p_2)\lambda + (n_{11}n_{22} - n_{12}^2)p_1p_2 = 0 \quad (3.36)$$

The eigenvalues are equal to the squares of the micro-manipulator natural frequencies;  $\lambda_1 = \tilde{\omega}_{e1}^2$  and  $\lambda_2 = \tilde{\omega}_{e2}^2$ . The algebraic solutions for  $p_1$  and  $p_2$  are:

$$\begin{aligned} p_1 &= \frac{1}{2n_{11}} \left[ (\lambda_1 + \lambda_2) - \sqrt{(\lambda_1 + \lambda_2)^2 - \frac{4n_{11}n_{22}\lambda_1\lambda_2}{n_{11}n_{22} - n_{12}^2}} \right] \\ p_2 &= \frac{1}{2n_{22}} \left[ (\lambda_1 + \lambda_2) + \sqrt{(\lambda_1 + \lambda_2)^2 - \frac{4n_{11}n_{22}\lambda_1\lambda_2}{n_{11}n_{22} - n_{12}^2}} \right] \end{aligned} \quad (3.37)$$

A second pair of gains is attainable by reversing the signs on the square root terms. The choice of which gains to use is manipulator dependant. A useful rule of thumb is that it is preferable to focus the first mode (at  $\tilde{\omega}_{e1}$ ) in the larger micro-manipulator joint, which is better able to dissipate large amounts of elastic energy.

Finally, the diagonal derivative gain matrix,  $\mathbf{D}_{IM}$ , is calculated from  $\mathbf{M}_{rr}$ ,  $\mathbf{P}_{IM}$ , and the desired damping ratio,  $\zeta$ :

$$\mathbf{D}_{IM} = \begin{bmatrix} d_1 & 0 \\ 0 & d_2 \end{bmatrix}, \quad (3.38)$$

where

$$\begin{aligned} d_1 &= 2\zeta\sqrt{m_{11}p_1} \\ d_2 &= 2\zeta\sqrt{m_{22}p_2} \end{aligned} \quad (3.39)$$

This basic procedure can be extended to find diagonal gain matrices for a general  $n$ -DOF spatial manipulator. It may also often be possible to lock all but two parallel joints so that the above equations can be used directly.

## Chapter 4

# Damping Performance Prediction and Evaluation Tools

In Chapter 3, two active damping strategies were introduced and developed. These strategies, and others, aim to provide optimal damping for a specified nominal micro-manipulator configuration. There is, however, very little published research on methods of determining the best nominal configurations. One exception is the *coupling map*, originally developed by Torres for path-planning [21], but also suggested as a tool to determine the best micro-manipulator configurations for active damping.

Two new performance prediction tools, the *accelerative damping map* and the *modal inertia map*, were developed as part of the present work. Each of these tools produces a scalar measure of predicted damping performance at a given nominal micro-manipulator configuration. A map of performance predictions over the range of micro-manipulator configurations is generated by plotting these individual scalar predictions. The three methods are introduced in the above order in §4.1 through §4.3.

The general macro-micro manipulator equations of motion were presented in Chapter 3. They are repeated here for convenience:

*General Macro-Micro Manipulator Equations of Motion:*

$$\begin{bmatrix} \mathbf{M}_{ee} & \mathbf{M}_{er} \\ \mathbf{M}_{er}^T & \mathbf{M}_{rr} \end{bmatrix} \begin{bmatrix} \ddot{\mathbf{q}}_e \\ \ddot{\mathbf{q}}_r \end{bmatrix} + \begin{bmatrix} \mathbf{K}_{ee} & \mathbf{0} \\ \mathbf{0} & \mathbf{0} \end{bmatrix} \begin{bmatrix} \mathbf{q}_e \\ \mathbf{q}_r \end{bmatrix} = \begin{bmatrix} \boldsymbol{\tau}_e \\ \boldsymbol{\tau}_r \end{bmatrix} \quad (4.1)$$

A simplified model with a massless macro-manipulator was required for the development of the P-PED method. The resulting simplified equations of motion will be required to develop the Coupling Map below and so are also repeated:

*Simplified Macro-Micro Manipulator Equations of Motion:*

$$\begin{bmatrix} \mathbf{M}_b & \mathbf{M}_{br} \\ \mathbf{M}_{br}^T & \mathbf{M}_{rr} \end{bmatrix} \begin{bmatrix} \ddot{\mathbf{q}}_e \\ \ddot{\mathbf{q}}_r \end{bmatrix} + \begin{bmatrix} \mathbf{K}_b & \mathbf{0} \\ \mathbf{0} & \mathbf{0} \end{bmatrix} \begin{bmatrix} \mathbf{q}_b \\ \mathbf{q}_r \end{bmatrix} = \begin{bmatrix} \boldsymbol{\tau}_b \\ \boldsymbol{\tau}_r \end{bmatrix} \quad (4.2)$$

A standard measure of damping performance is introduced in §4.4. This measure is used throughout the simulation and experimental work of Chapters 5 and 6 to quantify the observed damping performance.

## 4.1 Coupling Map

The Coupling Map (CM) was proposed by Torres as a path-planning tool, and is an extension of the Disturbance Map and the Enhanced Disturbance Map [21], which were applicable only to free-floating space manipulators. The Coupling Map can, however, also be used on elastically constrained manipulators, such as a micro-manipulator mounted on a flexible structure. Application of the Coupling Map as a tool for determining optimum micro-manipulator configurations for active damping is only briefly mentioned by Torres [21].

Some of the steps in the derivation which follows are questionable when considered in the context of using CM as a damping performance prediction tool. These steps are denoted by a question mark (?) and are discussed further in §4.1.2.

### 4.1.1 Derivation

The original presentation of the Coupling Map is rewritten below using the notation introduced in §3.1 and §3.3.1. Many of the original explanations have not been included; the

reader is directed to references [21] and [22] for further details.

The assumptions required for P-PED are also required for the Coupling Map, namely that the micro-manipulator is supported on a massless flexible structure (?) with no internal degrees of freedom. The applicable equations of motion are therefore those of (4.2). A generalized momentum vector,  $\mathbf{p}$ , is also required, and is defined as:

$$\mathbf{p} = \mathbf{M}(\bar{\mathbf{q}})\dot{\mathbf{q}} \quad (4.3)$$

The Coupling Map is based on five additional assumptions, beyond the massless flexible structure requirement, as follows:

1. the manipulator begins its motion from rest;
2. gravitational forces are negligible; (?)
3. internal forces between the flexible structure and the micro-manipulator are small; (?)
4. structural resonances in the flexible structure are not excited;
5. the end-effector does not interact with the environment.

According to the first assumption, the generalized momentum,  $\mathbf{p}$ , is initially zero, and the other assumptions ensure that it remains very small. This conservation of momentum assumption forms the basis of the Coupling Map, and is expressed as:

$$\mathbf{M}(\bar{\mathbf{q}})\dot{\mathbf{q}} = \begin{bmatrix} \mathbf{M}_b & \mathbf{M}_{br} \\ \mathbf{M}_{br}^T & \mathbf{M}_{rr} \end{bmatrix} \begin{bmatrix} \dot{\mathbf{q}}_b \\ \dot{\mathbf{q}}_r \end{bmatrix} = \begin{bmatrix} \mathbf{p}_b \\ \mathbf{p}_r \end{bmatrix} \approx \begin{bmatrix} 0 \\ 0 \end{bmatrix} \quad (4.4)$$

Once conservation of momentum has been assumed, equation (4.4) can be used to establish a relationship between rigid micro-manipulator motions and the elastic deflections of the flexible structure.

Either row of equation (4.4) could be used to solve for  $\dot{\mathbf{q}}_b$  as a function of  $\dot{\mathbf{q}}_r$ . The Coupling Map is developed from the first row, which enforces conservation of momentum for the base elastic degrees of freedom. The pertinent relationship between small micro-

manipulator joint displacements and the resulting base displacements is:

$$\delta \mathbf{q}_b = \mathbf{G} \delta \mathbf{q}_r, \quad (4.5)$$

where  $\mathbf{G} = -\mathbf{M}_b^{-1} \mathbf{M}_{br}$  and the derivative operation has been replaced by a variation.

The matrix  $\mathbf{G}$  is called the system's *disturbance matrix* and it relates infinitesimal joint motions to infinitesimal base motions for a *free-floating* manipulator. It is applicable to elastically constrained systems only under assumptions 3, 4, and 5 from the above list. For a free-floating manipulator held stationary by reaction jets,  $\delta \mathbf{q}_b$ , called the *instantaneous base dynamic disturbance*, is proportional to the required forces/torques exerted by the jets. That is,

$$\boldsymbol{\tau}_b \propto \delta \mathbf{q}_b \quad (?) \quad (4.6)$$

It is noted that the elastic characteristics of the flexible structure have not yet been included in the derivation. To include these characteristics, the elastic strain energy,  $V$ , is used as a measure of the induced elastic deflection due to micro-manipulator motions. If the force  $\boldsymbol{\tau}_b$  is applied to the flexible structure, the resulting strain energy is:

$$V = \frac{1}{2} \boldsymbol{\tau}_b^T \mathbf{K}_b^{-1} \boldsymbol{\tau}_b \quad (4.7)$$

Substituting from equation (4.6) gives

$$V \propto \delta \mathbf{q}_b^T \mathbf{K}_b^{-1} \delta \mathbf{q}_b \quad (4.8)$$

Finally, from equation (4.5),  $V$  is rewritten in terms of infinitesimal micro-manipulator joint motions,  $\delta \mathbf{q}_r$ :

$$V \propto \delta \mathbf{q}_r^T \mathbf{Q} \delta \mathbf{q}_r, \quad (4.9)$$

where the positive definite matrix

$$\mathbf{Q} = \mathbf{G}^T \mathbf{K}_b^{-1} \mathbf{G} = (-\mathbf{M}_b^{-1} \mathbf{M}_{br})^T \mathbf{K}_b^{-1} (-\mathbf{M}_b^{-1} \mathbf{M}_{br}) \quad (4.10)$$

is defined as the *coupling matrix*. The eigenvalues of  $\mathbf{Q}$  indicate the degree of coupling between micro-manipulator joint motions and the resulting strain energy induced in the flexible structure. Large eigenvalues indicate a high degree of coupling and therefore predict good active damping performance.

As devised for path-planning, the Coupling Map includes both the Euclidian norm of a vector of the eigenvalues of  $\mathbf{Q}$ , indicated by shading, superimposed on lines showing the directions of least coupling, as determined by the appropriate eigenvector. For active damping, only the degree of coupling between the micro-manipulator and its elastic base is important, so the lines are not included in this work. Also, the coupling magnitude is indicated by the height of a surface plot rather than by shading. Sample Coupling Maps are available in §5.1.3, 5.2.3, and 6.3.1.

It should also be noted that a singular value decomposition was prescribed in the original work, rather than an eigenvalue/eigenvector analysis. However, the eigenvalues are identical to the singular values for a positive definite matrix such as  $\mathbf{Q}$ , so the more common and efficient eigenvalues are used here with identical results.

#### 4.1.2 Discussion

A number of difficulties arise when the Coupling Map is used as a damping performance prediction tool, four of which were indicated by questions marks (?) in the previous section. These, plus the additional problem of frame dependance, are discussed below. Where solutions have been found, they are also presented.

### **Model Simplifications**

The derivation of the Coupling Map requires a system with a massless flexible structure that has no internal degrees of freedom. The LAURA-SARA manipulator obviously does not meet these criteria, so Guyan reduction was employed to reduce the system to fit the required model (see Appendix C).

When Guyan reduction was applied for P-PED in §3.3.4, only the inertia of the macro-manipulator and the micro-manipulator base were included. In contrast, the complete micro-manipulator is included when reducing the system to calculate the Coupling Map.

### **Assumption of Negligible Gravitational Forces**

One of the assumptions in developing the Coupling Map is that gravitational forces are negligible. This presents no difficulties for the space manipulators for which the method was developed, but is clearly invalid for the terrestrial LDUA manipulator (see §1.1). However, flexible structure deflections due to gravitational forces are typically small and may be neglected. Alternatively, the nominal state of the manipulator can be calculated under the influence of gravity, and the equations of motion linearized about this state. Gravity is not a concern for the LAURA-SARA manipulator as it acts on a horizontal plane.

### **Assumption of Small Interbody Forces**

This is a reasonable assumption for path-planning where a good path will lead to small forces and torques between the micro-manipulator and its base. However, for effective active damping the micro-manipulator must exert large forces on its base. No resolution to this problem has been found. Of course, ‘small’ is a relative term and the assumption may still apply for a small micro-manipulator mounted on a massive base.

## Proportionality of Displacements and Restraint Forces

Through equation (4.6) the instantaneous base dynamic disturbance,  $\delta\mathbf{q}_b$ , is related to reaction forces and eventually to the strain energy of the flexible structure,  $V$ . Although strictly there is nothing wrong with this equation, it seems awkward to start with momentum (velocity) considerations and later switch to forces and torques, which are more appropriately considered with accelerations.

The meaning of  $\boldsymbol{\tau}_b$  in the context of an elastically supported micro-manipulator, rather than a free-floating manipulator, is also ambiguous.

## Frame Dependence

It is a simple matter to show that the coupling matrix,  $\mathbf{Q}$ , is a function of the location of the base coordinate frame, and *therefore* not frame invariant. The choice of coordinate frames affects both the magnitude and *shape* of the Coupling Map. To resolve this problem would require significant changes in the derivation, so that the resulting equations could no longer be called the Coupling Map. Perhaps by chance, the shape and magnitude of the Coupling Maps for the manipulators investigated in Chapters 5 and 6 were qualitatively unchanged for reasonable coordinate frame locations.

## 4.2 Accelerative Damping Map

The Accelerative Damping Map (ADM) was developed in the current work in response to the problems found with the Coupling Map. No macro-micro manipulator model simplifications are required, gravitational forces are not a concern, and the ADM is frame invariant. Also, the ADM is based on micro-manipulator joint accelerations and the resulting generalized forces (wrench) applied to the tip of the macro-manipulator.

### 4.2.1 Derivation

There are no restraints on the manipulator model, so the general equations of motion defined in equation (4.1) are used. Two simplifying assumptions are however required:

1. micro-manipulator joint rates are small;
2. flexible structure elastic deflections, rates, and accelerations are small.

The small rate assumptions were used to develop the linearized equations of motion in equation (4.1). The elastic force vector,  $\boldsymbol{\tau}_e$ , of equation (4.1) is a sum of force vectors resulting from elastic deflections and accelerations and from micro-manipulator joint accelerations. That is,  $\boldsymbol{\tau}_e = \boldsymbol{\tau}_{ee} + \boldsymbol{\tau}_{er}$ , where  $\boldsymbol{\tau}_{ee} = \mathbf{M}_{ee}\ddot{\mathbf{q}}_e + \mathbf{K}_{ee}\mathbf{q}_e$  and  $\boldsymbol{\tau}_{er} = \mathbf{M}_{er}\ddot{\mathbf{q}}_r$ . The second assumption ensures that  $\boldsymbol{\tau}_{ee}$  remains small and is therefore neglected.

Therefore, only micro-manipulator joint accelerations can apply appreciable forces and moments to the flexible structure. For any vector of micro-manipulator joint accelerations applied from rest,  $\ddot{\mathbf{q}}_r$ , the resulting forces and moments applied to the base are:

$$\boldsymbol{\tau}_{er} = \mathbf{M}_{er}\ddot{\mathbf{q}}_r \quad (4.11)$$

As with the Coupling Map, the strain energy,  $V$ , is used as a measure of the effect of  $\boldsymbol{\tau}_{er}$  on the flexible structure. The strain energy is:

$$\begin{aligned} V &= \frac{1}{2}\boldsymbol{\tau}_{er}^T \mathbf{K}_{ee}^{-1} \boldsymbol{\tau}_{er} \\ &= \frac{1}{2}\ddot{\mathbf{q}}_r^T (\mathbf{M}_{er}^T \mathbf{K}_{ee}^{-1} \mathbf{M}_{er}) \ddot{\mathbf{q}}_r \\ &= \frac{1}{2}\ddot{\mathbf{q}}_r^T \mathbf{R} \ddot{\mathbf{q}}_r \end{aligned} \quad (4.12)$$

where

$$\mathbf{R} = \mathbf{M}_{er}^T \mathbf{K}_{ee}^{-1} \mathbf{M}_{er} \quad (4.13)$$

is the *accelerative damping matrix*. Each eigenvalue of  $\mathbf{R}$  indicates the induced strain energy when the micro-manipulator joint acceleration vector  $\ddot{\mathbf{q}}_r$  is equal to the corresponding normalized eigenvector. Thus, if the eigenvalues are large, good active damping performance

is predicted. The Euclidian norm of a vector of the eigenvalues of  $\mathbf{R}$  is the scalar measure of predicted damping performance from the Accelerative Damping Map.

### 4.2.2 Discussion

Unlike the Coupling Map, ADM was developed specifically as a tool to determine the optimal micro-manipulator configurations for active damping. There are no restrictions on the geometry or mass distribution of the macro-manipulator, and the resulting map is frame invariant. Since active damping generally involves rapid changes in direction, it is reasonable to expect micro-manipulator joint rates to remain low, while accelerations are large. The primary assumptions of ADM fit that scenario.

A potential problem with ADM is that the mass of the macro-manipulator is not used in deriving the method. The accelerative coupling matrix  $\mathbf{R}$  is a function only of the  $\mathbf{M}_{er}$  mass terms and the flexible structure stiffness matrix,  $\mathbf{K}_{ee}$ . The Modal Inertia Map, presented below, was developed to address this shortfall.

## 4.3 Modal Inertia Map

### 4.3.1 Concept

Both the Coupling Map and the Accelerative Damping Map assume small macro-manipulator elastic deflections. Displacements (CM) or accelerations (ADM) are applied to the joints of the micro-manipulator, and the effect of the resulting base wrench on the macro-manipulator is ascertained through the elastic strain energy. The Modal Inertia Map (MIM) is completely different: it is based on measuring the *micro*-manipulator excitation resulting from *macro*-manipulator tip accelerations.

Recall that Joint Space Derivative (JSD) active damping schemes, such as P-PED and Impedance Matching, rely on macro-manipulator vibrations inducing micro-manipulator joint motions. Optimal damping performance is thus achieved when the micro-manipulator is configured so that its joints are very sensitive to macro-manipulator vibrations. The

MIM is a method of measuring this sensitivity for a particular mode of macro-manipulator vibration.

The dominant mode concept, introduced in the Impedance Matching derivation (§3.4.1), is required for the MIM. The predicted damping performance is measured by the sensitivity of the micro-manipulator to macro-manipulator vibrations in the dominant mode. It was argued in §3.4.1 that the first mode will nearly always dominate the system response. However, Modal Inertia Maps can be developed for other modes if required.

To illustrate the MIM concept, a simple planar macro-micro manipulator like that used to derive Impedance Matching (§3.4.1, Figure 3.3) is considered. Macro-manipulator vibrations are confined to the dominant mode, with the single micro-manipulator joint locked at a nominal angle. The peak torque required to hold the micro-manipulator as the macro-manipulator vibrates is easily calculated from the equations of motion. If this peak torque is large at a particular micro-manipulator configuration, good damping performance is expected.

### 4.3.2 Derivation

No model simplifications are required to develop the Modal Inertia Map, so the general equations of motion in equation (4.1) are used. The first step is to calculate the dominant macro-manipulator mode shape,  $\tilde{\mathbf{q}}_e$ , with the micro-manipulator locked in a nominal configuration,  $\bar{\mathbf{q}}_r$ . The mode shapes are calculated by solving the eigenvector problem for the model:  $\mathbf{M}_{ee}\ddot{\mathbf{q}}_e + \mathbf{K}_{ee}\mathbf{q}_e = 0$ . (It is noted that  $\mathbf{M}_{ee}$  and  $\mathbf{K}_{ee}$  are functions of  $\bar{\mathbf{q}}_r$ ). The dominant elastic mode shape,  $\tilde{\mathbf{q}}_e$ , is generally that of the lowest mode of vibration.

Alternatively, if an accurate macro-manipulator model is not available, the dominant mode shape can be directly measured on the assembled manipulator. The measurements should be made on the micro-manipulator base, as the motion of the base is required in the next stage of the derivation.

As the macro-manipulator vibrates, the elastic coordinates are described by

$$\mathbf{q}_e = A\tilde{\mathbf{q}}_e \sin(\tilde{\omega}_e t + \phi), \quad (4.14)$$

where  $A$  is the vibration amplitude and  $\tilde{\omega}_e$  is the frequency of the dominant mode. Similarly, the elastic accelerations are

$$\ddot{\mathbf{q}}_e = \tilde{\omega}_e^2 A\tilde{\mathbf{q}}_e \sin(\tilde{\omega}_e t + \phi). \quad (4.15)$$

The vibration is normalized by setting  $A = 1$ . The peak acceleration of the elastic structure is thus  $\ddot{\mathbf{q}}_{e,max} = \tilde{\omega}_e^2 \tilde{\mathbf{q}}_e$ . At the instant when  $\ddot{\mathbf{q}}_{e,max}$  is applied, the torques  $\boldsymbol{\tau}_r$  required to lock the micro-manipulator joints at their nominal configuration are:

$$\boldsymbol{\tau}_{r,max}(\bar{\mathbf{q}}_r) = \mathbf{M}_{er}^T \ddot{\mathbf{q}}_{e,max} = \mathbf{M}_{er}^T \tilde{\omega}_e^2 \tilde{\mathbf{q}}_e \quad (4.16)$$

For the simple manipulator used to conceptually develop the MIM in the previous section, the peak torque required to lock the single micro-manipulator link was proportional to the effective inertia of the link for base motions parallel to the dominant mode shape. Similarly, the elements of the vector  $\boldsymbol{\tau}_{r,max}(\bar{\mathbf{q}}_r)$  are proportional to the effective inertia seen at each joint for vibration confined to the dominant elastic mode. The Euclidian norm of  $\boldsymbol{\tau}_{r,max}(\bar{\mathbf{q}}_r)$  is called the *modal inertia* for the micro-manipulator configuration defined by  $\bar{\mathbf{q}}_r$ . The magnitude of the modal inertia is used as the measure of predicted damping performance.

### 4.3.3 Discussion

The Modal Inertia Map was developed specifically for Joint Space Derivative (JSD) control damping strategies. All of the terms of the linearized equations of motion are used to derive the Modal Inertia Map. By contrast, only the elastic stiffness matrix  $\mathbf{K}_{ee}$  and the  $\mathbf{M}_{er}$  block of the system mass matrix are used to derive the Accelerative Damping Map. For the Coupling Map, a reduced macro-manipulator stiffness matrix,  $\mathbf{K}_b$ , is used with the reduced

mass matrix blocks,  $\mathbf{M}_b$  and  $\mathbf{M}_{br}$ .

## 4.4 Damping Performance Evaluation

The two major research goals of this work have been to compare the damping performance between active damping methods and to develop and evaluate tools for predicting the best micro-manipulator configurations for damping. A standard measure of damping performance for the simulation and experimental results is required for both these objectives.

It has been assumed in the derivation of Impedance Matching and the Modal Inertia Map that a single mode of vibration, at a frequency  $\tilde{\omega}_e$ , dominates the elastic response. This assumption was validated by the simulation and experimental results of Chapters 5 and 6. A similar assumption is therefore used below to derive the standard measure of damping performance,  $\kappa$ .

Strain energy,  $V = \frac{1}{2} \mathbf{q}_e^T \mathbf{K}_{ee} \mathbf{q}_e$ , is used to measure the elastic energy in the system at any instant. For undamped dominant mode vibration, the elastic coordinates are defined by  $\mathbf{q}_e = \mathbf{q}_{e,max} \sin(\tilde{\omega}_e t + \phi)$ . The strain energy can thus be expanded as  $V = V_{max} \sin^2(\tilde{\omega}_e t + \phi)$ , where  $V_{max} = \frac{1}{2} \mathbf{q}_{e,max}^T \mathbf{K}_{ee} \mathbf{q}_{e,max}$  is the peak strain energy.

If the vibration is viscously damped, the elastic coordinates are defined by

$$\mathbf{q}_e = e^{-kt} \mathbf{q}_{e,max} \sin(\tilde{\omega}_e t + \phi), \quad (4.17)$$

where  $k$  is a time constant defining the exponential rate of decay. The strain energy is thus

$$V = e^{-\kappa t} V_{max} \sin^2(\tilde{\omega}_e t + \phi), \quad (4.18)$$

and  $\kappa = 2k$  is used as the standard measure of damping performance.

## Chapter 5

# Simulation Results

Simulation results for five simplified manipulators are presented in this chapter. The manipulators are divided into two groups; four very simple (VS) manipulators and one consisting of SARA mounted on a single flexible link. The latter is referred to as the OLS manipulator, for ‘One Link plus SARA’.

It is difficult to gain insight into the procedures and methods of active damping by implementing them experimentally on a complex manipulator. There are inevitably many unmodelled complexities in real systems, and it can be difficult to separate their effects from those of the theory under investigation. The simplified simulations presented here avoid these complications and clearly demonstrate the pros and cons of the various methods developed in previous chapters.

Another disadvantage of a purely experimental investigation is that the properties of the experimental manipulator are generally fixed. There is no guarantee that the results and conclusions attained with a particular manipulator will be applicable to other manipulators. To address this concern, the four kinematically similar VS manipulators were designed to exhibit a wide range of stiffness and inertial properties.

The OLS manipulator is a simplified version of the LAURA-SARA manipulator, which was introduced in Chapter 2 and is investigated experimentally in Chapter 6. A comparison of the OLS and LAURA-SARA results will help to isolate the effects of various complexities in

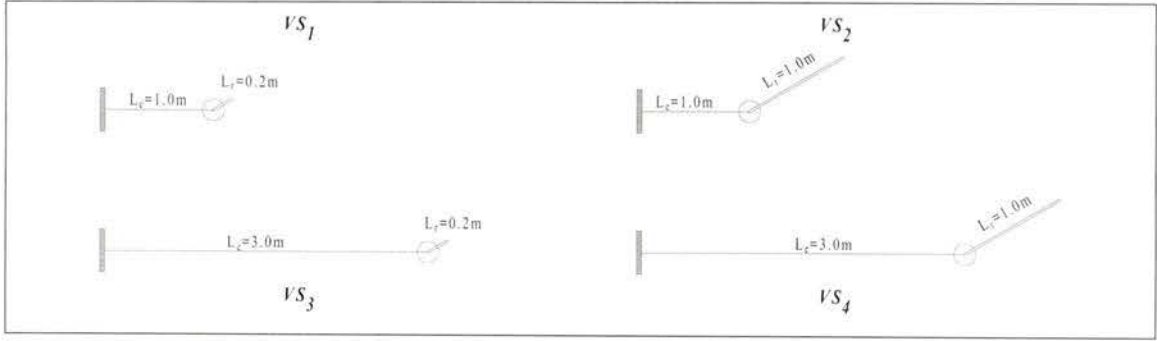


Figure 5.1: *Very Simple (VS) Manipulators*

the latter.

This chapter is intended to demonstrate potential strengths and weaknesses of the different methods, and to gain some insight into their application. For the sake of brevity, strain energy and joint position plots are not included here. The experimental results of Chapter 6 are presented in more detail.

## 5.1 Very Simple Manipulators

### 5.1.1 System Models

The four VS manipulators,  $VS_1$  through  $VS_4$ , are illustrated in Figure 5.1, and the properties of each are listed in Table 5.1. Each is a planar manipulator constructed from a single-DOF micro-manipulator mounted on a round base, which is itself mounted on a *massless* flexible link. The manipulators differ only in the lengths of the flexible and rigid links. For each manipulator, the flexible link stiffness matrix is equal to that of an aluminum link ( $E=68.95$  GPA) with a  $10\text{cm} \times 1\text{cm}$  cross-section.

Table 5.1: *Geometric and Inertial Properties of the VS Manipulators*

Property	Symbol	Units	$VS_1$	$VS_2$	$VS_3$	$VS_4$
Base Mass	$m_b$	(kg)	3.0	3.0	3.0	3.0
Base Radius	$R_b$	(m)	0.1	0.1	0.1	0.1
Rigid Link Mass	$m_r$	(kg)	1.0	1.0	1.0	1.0
Flexible Link Length	$L_e$	(m)	1.0	1.0	3.0	3.0
Rigid Link Length	$L_r$	(m)	0.2	1.0	0.2	1.0

Since the VS flexible structures are massless, Guyan reduction is not required for either P-PED (§3.3) or the Coupling Map (§4.1). This is important, as the results from the VS manipulators thus reflect the performance of P-PED and the Coupling Map as originally presented by Torres [21]. This helps to isolate any problems caused by implementing Guyan reduction for the experimental work presented in Chapter 6.

The VS manipulators have three degrees of freedom, defined by the vector  $\mathbf{q} = [y_b, \theta_b, \theta_r]^T$ , where  $y_b$  and  $\theta_b$  are the transverse and angular elastic base displacements, and  $\theta_r$  is the rigid link angle. The flexible link is modelled as axially rigid, so axial base displacement is neglected. Manipulator dynamics were linearized about a nominal micro-manipulator angle,  $\bar{\theta}_r$ , for the damping performance simulations which follow.

### 5.1.2 Damping Performance

The damping performance of P-PED and Impedance Matching on the VS manipulators was determined by applying an initial elastic disturbance,  $\mathbf{q}_{b0} = [y_{b0}, \theta_{b0}]^T$ , to the micro-manipulator base. An exponential curve fit to the strain energy response then yielded the decay constant,  $\kappa$ , for the particular configuration and damping method. The damping performance is potentially a function not only of the PD gains and nominal micro-manipulator configuration, but also of the direction of the initial disturbance,  $\mathbf{q}_{b0}$ . However, simulations with many different initial disturbance vectors gave nearly identical results. A standard initial disturbance of  $\mathbf{q}_{b0} = [1cm, 0]^T$  was used to generate the results which follow. Figure 5.2 shows the damping performance results for the four systems over a complete range of nominal micro-manipulator configurations.

### Pseudo-Passive Energy Dissipation

Recall from §3.3.4 that P-PED performs poorly when directly applied to manipulators with poorly conditioned stiffness matrices. In particular, the very stiff translational direction(s) lead to unreasonably large terms in the micro-manipulator proportional and derivative gain matrices. Two methods of avoiding this problem were suggested: the stiff directions can

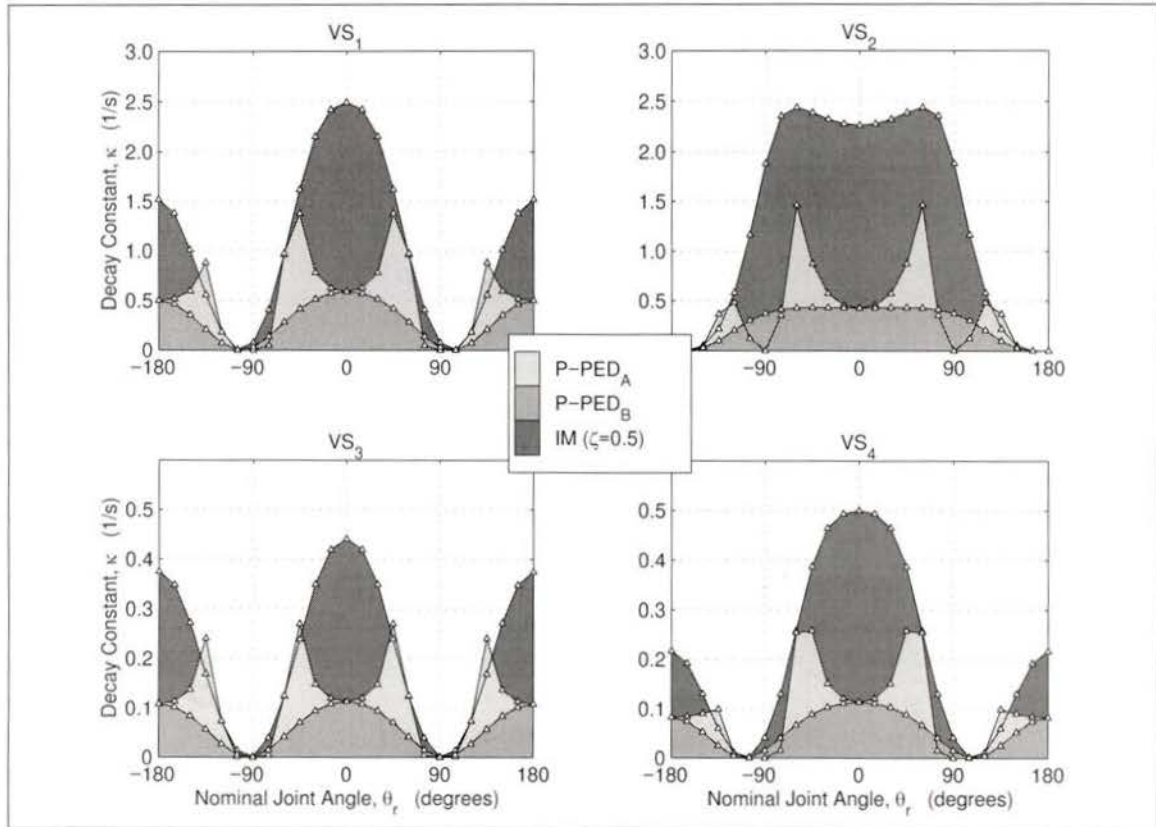


Figure 5.2: Observed Damping Performance for VS Manipulators Using P-PED<sub>A</sub>, P-PED<sub>B</sub>, and Impedance Matching

simply be neglected, or the stiffness of the stiff direction(s) can be reduced to that of a more flexible direction. Both these methods, labelled P-PED<sub>A</sub> and P-PED<sub>B</sub> respectively, were implemented on the VS manipulators.

The virtual manipulator Jacobian, which is used to determine the P-PED gain matrices, has the same form for each of the four VS manipulators:

$$\mathbf{J}_{cm,vs} = \begin{bmatrix} -\frac{1}{2}L_r \sin(\bar{\theta}_r) \\ +\frac{1}{2}L_r \cos(\bar{\theta}_r) \end{bmatrix} \quad (5.1)$$

The PD joint gains are easily calculated as a function of  $\bar{\theta}_r$ :

$$\begin{aligned} \text{P-PED}_A: \quad p_A &= \frac{1}{4}k_{ry}L_r^2 \cos^2(\bar{\theta}_r) & d_A &= \frac{1}{4}c_{ry}L_r^2 \cos^2(\bar{\theta}_r) \\ \text{P-PED}_B: \quad p_B &= \frac{1}{4}k_{ry}L_r^2 & d_B &= \frac{1}{4}c_{ry}L_r^2 \end{aligned} \quad (5.2)$$

where  $k_{ry}$  and  $c_{ry}$  are the optimum spring and damper constants calculated for the mass-spring-damper systems, as per §3.3.2, and are independent of the micro-manipulator configuration. Note that  $p_A$  and  $d_A$  tend to zero as  $\bar{\theta}_r$  approaches  $\pm 90^\circ$ , whereas  $p_B$  and  $d_B$  are constants. When  $\bar{\theta}_r = 0^\circ$  and  $180^\circ$ , the gains for P-PED<sub>A</sub> and P-PED<sub>B</sub> are identical.

P-PED<sub>A</sub> generally out-performs P-PED<sub>B</sub>, but its good performance seems to be a result of neglecting the stiff axial direction rather than of a fundamental strength of the P-PED method. Observe that the best damping occurs on either side of  $\bar{\theta}_r = \pm 90^\circ$ , where the  $p_A$  and  $d_A$  gains are very small. Local minima are seen at  $\bar{\theta}_r = 0^\circ$  and  $180^\circ$ , where the gains are functions of the transverse stiffness only and are unaffected by the assumptions regarding the stiff axial direction.

The P-PED<sub>B</sub> performance curves have a very different shape than the P-PED<sub>A</sub> curves. Damping is generally most effective when the micro-manipulator is at  $\bar{\theta}_r = 0^\circ$  and  $180^\circ$  and least effective at  $\bar{\theta}_r = \pm 90^\circ$ , with the exception of VS<sub>2</sub>, where the performance curve has a single peak at  $\bar{\theta}_r = 0^\circ$ . These curves are very similar in shape to the Impedance Matching performance curves discussed below.

The damping performance from both P-PED methods was significantly worse than that obtained using Impedance Matching. A possible explanation is that P-PED on a planar manipulator is intended to approximate two orthogonal mass-spring-damper systems in the plane. The single DOF of the VS micro-manipulator is insufficient for this task. Better performance relative to Impedance Matching could perhaps be expected from a multi-DOF micro-manipulator, and is observed on the OLS manipulator.

### Impedance Matching

The VS manipulators are identical in form to the manipulator used to derive Impedance Matching in §3.4. From equation (3.31), the IM gains are:

$$\begin{aligned} p_{IM} &= J_r \tilde{\omega}_e^2 \\ d_{IM} &= 2\zeta J_r \tilde{\omega}_e \end{aligned} \tag{5.3}$$

where  $J_r = \frac{1}{3}m_r L_r^2$  is the mass moment of inertia of the rigid link about the joint axis of rotation,  $\tilde{\omega}_e$  is the dominant (first) elastic modal frequency of the flexible structure calculated with the micro-manipulator locked at its nominal configuration, and  $\zeta$  is the damping ratio of the micro-manipulator. Recall that the best damping is expected as  $\zeta \rightarrow 0$ , but larger values of  $\zeta$  are required to limit the magnitude of micro-manipulator joint motions. A compromise value of  $\zeta = 0.5$  is used for this investigation.

From Figure 5.2 it is observed that the damping performance using IM was consistently better than that using the P-PED methods. The curves for systems VS<sub>1</sub>, VS<sub>3</sub>, and VS<sub>4</sub> have approximately the same shape, with the best damping performance occurring at  $\bar{\theta}_r = 0^\circ$ , near zero damping at  $\bar{\theta}_r = \pm 90^\circ$ , and a local maximum at  $\bar{\theta}_r = \pm 180^\circ$ . System VS<sub>2</sub> is different however, with a local minimum at  $\bar{\theta}_r = 0^\circ$  and peak performance at  $\bar{\theta}_r = \pm 60^\circ$ .

The different shape of the VS<sub>2</sub> performance curve can be explained by the assumptions required to derive Impedance Matching in Chapter 3. When deriving IM, it was assumed that *the macro-manipulator continues to vibrate at the original frequency,  $\tilde{\omega}_e$ , while the micro-manipulator dissipates the elastic energy*. However,  $\tilde{\omega}_e$  was calculated with  $\theta_r$  locked and could change when compliance is introduced at the joint. Should the frequency change significantly, the micro-manipulator would no longer be properly ‘tuned’ and damping performance would be reduced.

Figure 5.3 shows the fractional change in  $\tilde{\omega}_e$  when the micro-manipulator is controlled with IM gains, rather than rigidly locked. The large change in  $\tilde{\omega}_e$  in the vicinity of  $\bar{\theta}_r = 0^\circ$  on VS<sub>2</sub> explains the truncated shape of the VS<sub>2</sub> performance curve.

### 5.1.3 Performance Predictions

The performance predictions from the Coupling Map (CM), Accelerative Damping Map (ADM), and Modal Inertia Map (MIM) are plotted in Figure 5.4. The prediction curves have been normalized so that each is dimensionless with a maximum value of one. The contribution of each map towards predicting the observed performance is defined by the

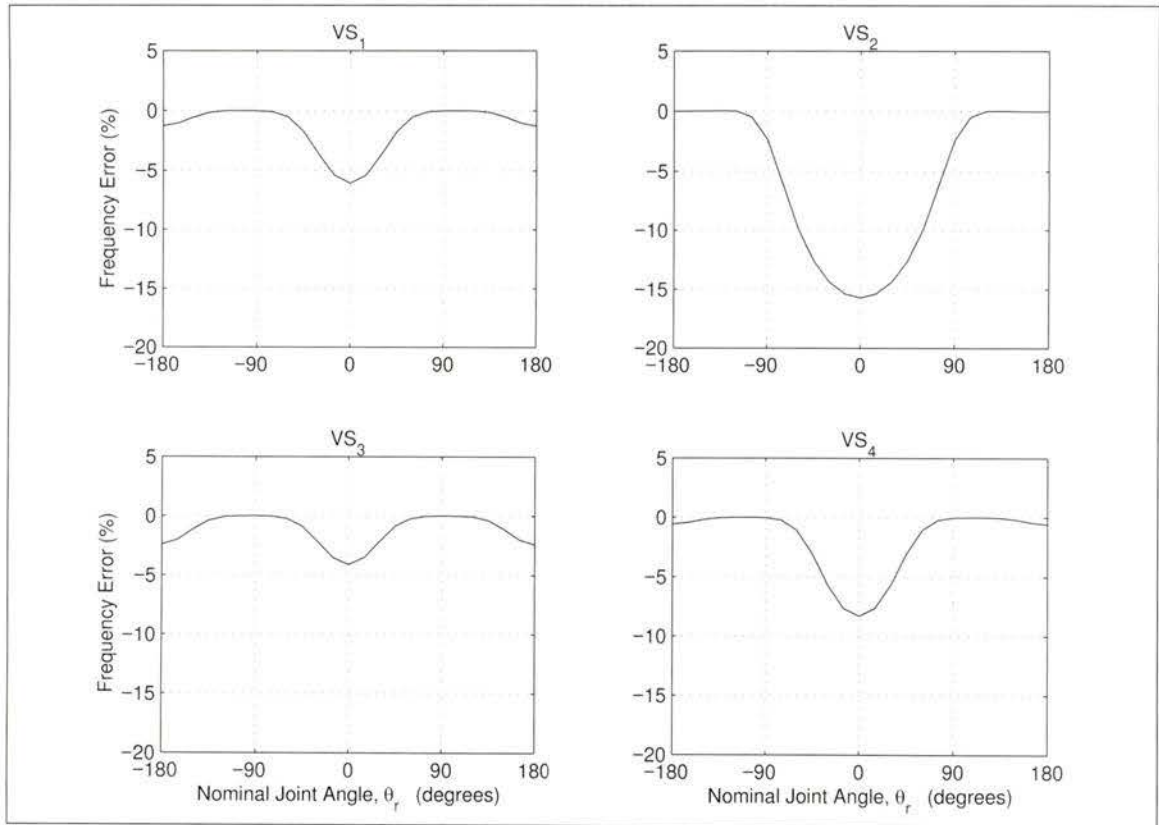


Figure 5.3: *Change in Dominant (First) Modal Frequency of VS Manipulators when IM Compliance is Introduced to Micro-Manipulator*

coefficient of determination,  $r^2$  [12]. The  $r^2$  values for each of the three maps versus each of P-PED<sub>A</sub>, P-PED<sub>B</sub>, and Impedance Matching are plotted in Figure 5.5.

The goal of the performance prediction maps is to determine the micro-manipulator configuration at which active damping is most effective. It is clear from the performance plots of the previous section that IM is more effective than either P-PED<sub>A</sub> or P-PED<sub>B</sub>, so the discussion which follows is focused on the IM results.

### Coupling Map

The CM curves in Figure 5.4 differ considerably from the ADM and MIM curves, and more importantly also from the measured damping performance. The Coupling Map is best at predicting the P-PED<sub>B</sub> performance, with a peak  $r^2$  value of 0.66 seen with VS<sub>2</sub>. Predictions of the P-PED<sub>A</sub> performance are the worst, with a peak  $r^2$  of only 0.23 seen

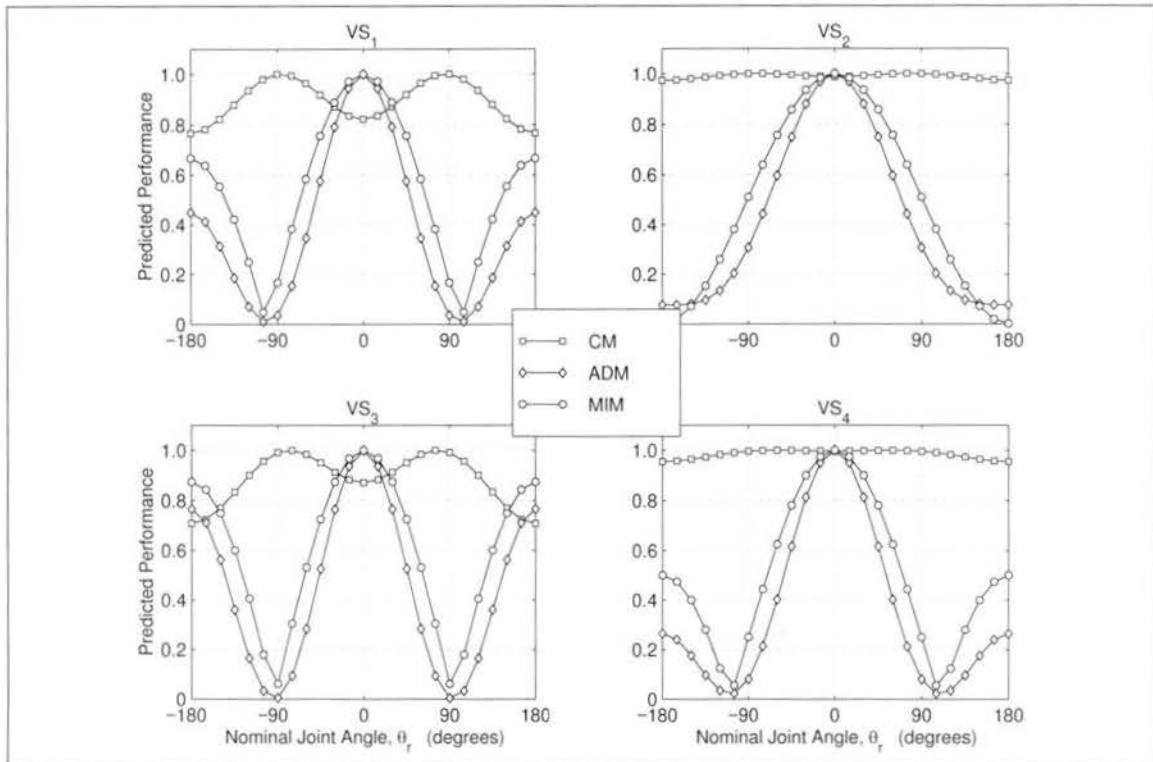


Figure 5.4: Damping Performance Predictions for VS Manipulators Using Coupling Map, Accelerative Damping Map, and Modal Inertia Map

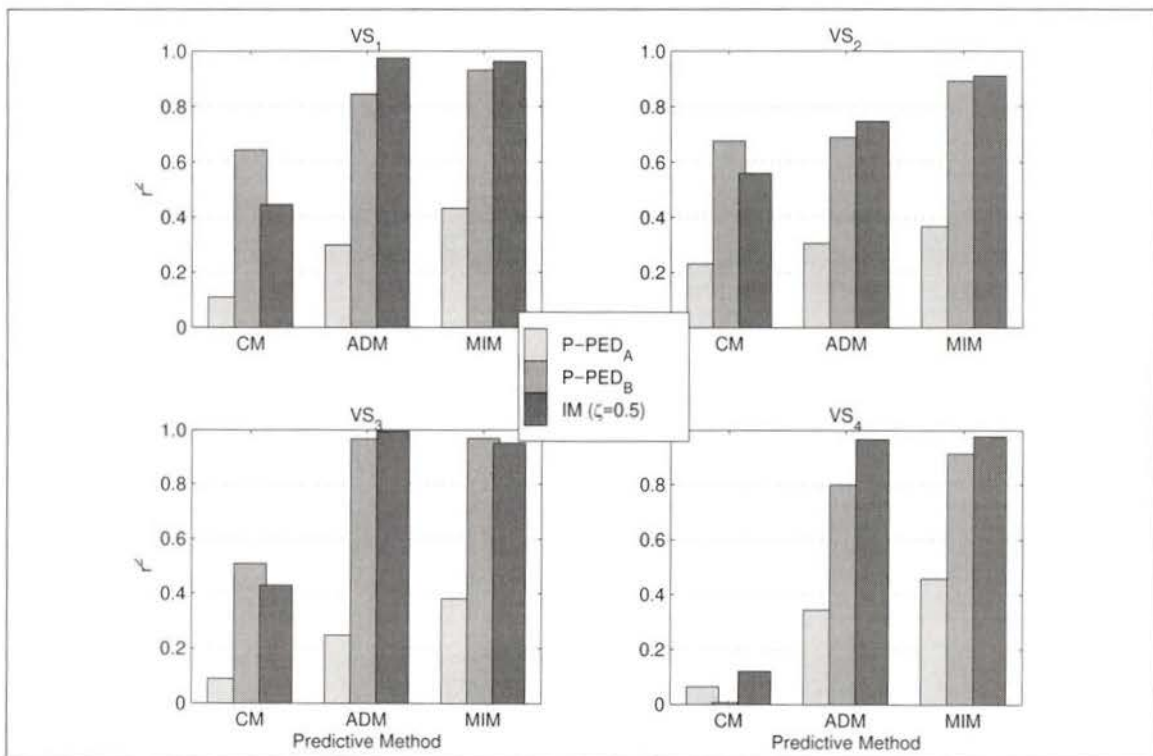


Figure 5.5: Contribution of CM, ADM, MIM in Predicting the P-PED<sub>A</sub>, P-PED<sub>B</sub>, and IM Damping Performance for VS Manipulators

with VS<sub>2</sub>. The inability of the Coupling Map to predict damping performance on the VS manipulators no doubt arises from the many Coupling Map problems discussed in §4.1.2.

### Accelerative Damping Map

The ADM curves are very poor predictors of P-PED<sub>A</sub> performance, but do exhibit the basic shape of the P-PED<sub>B</sub> and IM damping performance curves for the four VS systems. It is significant that the single central performance peak at  $\bar{\theta}_r = 0^\circ$  observed with P-PED<sub>B</sub> and IM (ignoring the central dip in performance) is reflected in the ADM predictions.

Between 75% and 98% of the shape of the IM performance curves is accounted for by the ADM predictions. The low of 75% is seen with VS<sub>2</sub> primarily due to the truncated performance which was discussed in §5.1.2. Since the goal of ADM is to predict the *maximum* degree of damping possible at a given configuration, it is not surprising that this limitation of the IM method is not seen in the predictions. The  $r^2$  values for the ADM curves versus the P-PED<sub>B</sub> performance are also quite high.

Other subtle details, such as the relative magnitude of the IM performance peaks at  $\bar{\theta}_r = 0^\circ$  and  $\bar{\theta}_r = 180^\circ$  for VS<sub>1</sub>, VS<sub>3</sub> and VS<sub>4</sub> are seen in the ADM prediction curves.

### Modal Inertia Map

There is little difference between the ADM prediction curves and the MIM prediction curves. Generally, the central peak of the ADM curves is more pronounced and has steeper sides, but the location of minima and maxima are nearly identical between the two maps. The ADM discussion therefore applies directly to the MIM curves.

The central assumption of the Modal Inertia Map is that the dominant mode shape,  $\tilde{q}_e$ , accurately represents the elastic vibration not only with  $\theta_r$  locked but also when compliance is introduced in the joint. It is possible, however, that joint compliance will affect  $\tilde{q}_e$ , just as it was shown to affect the corresponding modal frequency  $\tilde{\omega}_e$ . This was investigated by calculating the mode shape with IM joint compliance introduced to the joint,  $\tilde{q}_{e,IM}$ , and comparing it to  $\tilde{q}_e$ . The *mode shape error*, defined as the sine of the angle between these

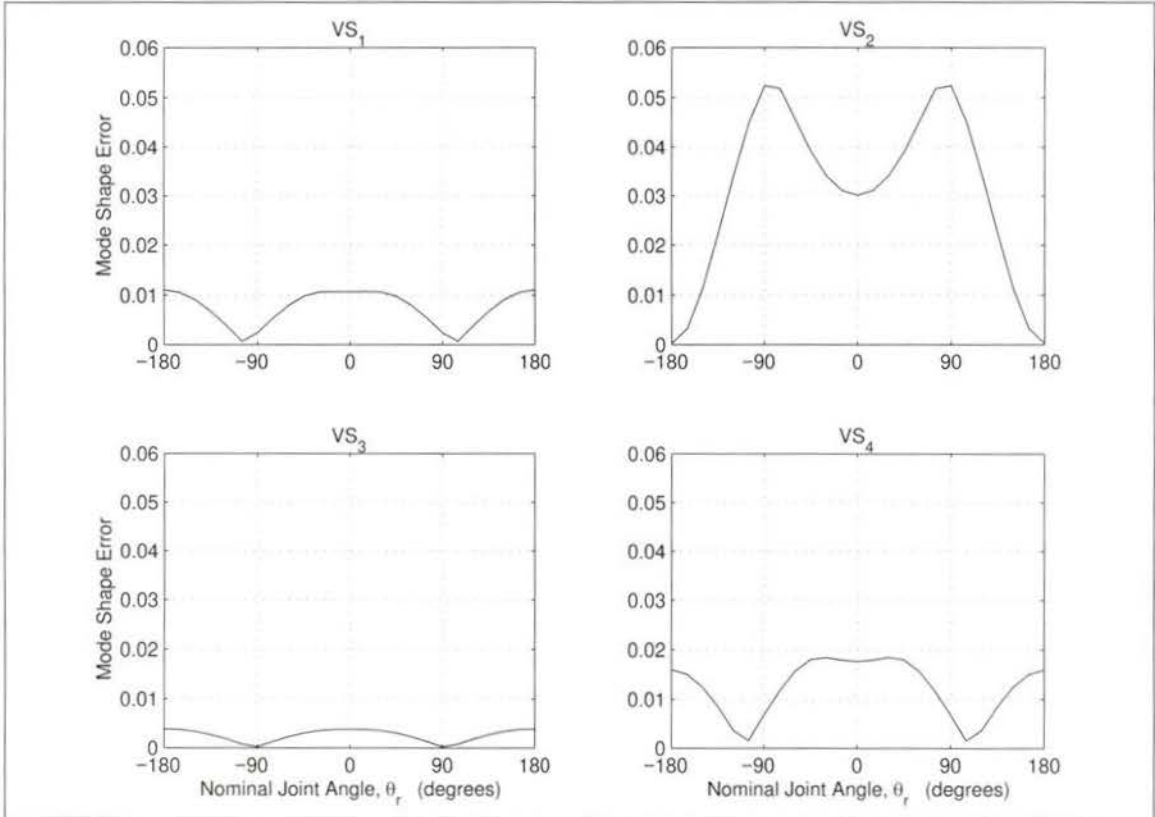


Figure 5.6: *Change in Shape of Dominant (First) Mode of VS Manipulators when IM Compliance is Introduced to Micro-Manipulator*

two vectors, is plotted in Figure 5.6. The error is less than 0.011 for VS<sub>1</sub> and VS<sub>3</sub>, and reaches peak values of 0.052 and 0.018 for VS<sub>2</sub> and VS<sub>4</sub> respectively. These errors are very small, indicating that MIM is essentially insensitive to the micro-manipulator gains used. This is an important result as it separates the performance prediction from the choice of active damping algorithm.

## 5.2 SARA on a Single Flexible Link

Many of the results obtained for the OLS manipulator closely mimic those for the manipulators of the previous section. The following discussion is therefore abbreviated to avoid repetition.



Figure 5.7: *One Link plus SARA (OLS) Manipulator*

### 5.2.1 System Model

Figure 5.7 shows the complete OLS manipulator. The flexible link is a 1.215m length of aluminum with a  $6.35\text{mm} \times 50\text{mm}$  cross-section. This cross-section is the same as the LAURA flexible links, and the length matches that of LAURA in the straight-out configuration. The OLS manipulator is thus equivalent to removing the LAURA2 joint from the LAURA-SARA manipulator and replacing it with a length of flexible link. The link is rigid in the axial direction.

A coordinate vector,  $\mathbf{q} = [\mathbf{q}_b^T, \mathbf{q}_r^T]^T$ , is defined, where  $\mathbf{q}_b = [y_b, \theta_b]^T$  defines the elastic deflections of the SARA base, and  $\mathbf{q}_r = [\theta_{S1}, \theta_{S2}, \theta_{S3}]^T$  defines the angles of the three joints of SARA. As with the VS manipulators, all non-linear terms in the dynamics equations are dropped.

The observed and predicted performance plots in the following sections are two-dimensional surfaces over a grid defining the range of nominal  $\theta_{S1}$  and  $\theta_{S2}$  angles,  $\bar{\theta}_{S1}$  and  $\bar{\theta}_{S2}$ , in  $15^\circ$  intervals. The nominal  $\theta_{S3}$  configuration is straight-out ( $\bar{\theta}_{S3} = 0^\circ$ ) for all simulations. At each point  $[\bar{\theta}_{S1}, \bar{\theta}_{S2}]$  the height of the surface represents the observed or predicted performance. Lines on the back planes of each plot are projections of the surface peaks intended to show the scale of surface features. Reference lines at  $90^\circ$  intervals are also included to help locate features on the grid.

## 5.2.2 Damping Performance

As before, the performance curves were generated by applying an initial deflection,  $\mathbf{q}_{b0}$ , to the SARA base and fitting an exponential decay function to the strain energy response. The decay constant,  $\kappa$ , is proportional to the damping performance. Various initial deflections were attempted with very little difference in the performance curves. A standard of  $\mathbf{q}_{b0} = [1cm, 0]^T$  was used for all simulations presented here.

### Pseudo-Passive Energy Dissipation

Figures 5.8 and 5.9 show the observed damping performance using P-PED<sub>A</sub> and P-PED<sub>B</sub> respectively. A peak performance of  $\kappa = 1.08s^{-1}$  was achieved for P-PED<sub>A</sub> with an average of  $\kappa = 0.40s^{-1}$ . The corresponding values for P-PED<sub>B</sub> are  $1.17s^{-1}$  and  $0.41s^{-1}$ .

The P-PED gain matrices have a much more complicated structure for the 3-dof SARA micro-manipulator than they did for the single-dof micro-manipulator of the previous section. Each element of the  $3 \times 3$  matrices is a non-linear function of the SARA joint angles and the virtual manipulator link lengths. The shape of the performance surfaces is therefore quite difficult to interpret. However, some simple comparisons to the results of the previous section can be informative.

When  $\bar{\theta}_{S2} = 0^\circ$  or  $\bar{\theta}_{S2} = 180^\circ$ , the OLS manipulator is very similar to the VS manipulators. Its three links form a line, and the base reaction forces to any joint movements are perpendicular to this line. Cross-sections through the surfaces of Figures 5.8 and 5.9 at these locations show a very strong resemblance to the corresponding curves for VS<sub>1</sub>, VS<sub>3</sub>, and VS<sub>4</sub> in Figure 5.2.

Both surfaces exhibit ‘valleys’ of poor performance where  $\bar{\theta}_{S1} = 0^\circ$  and  $180^\circ$ . This is in direct contrast to the Impedance Matching results of the next section, which show peak performance at these same locations.

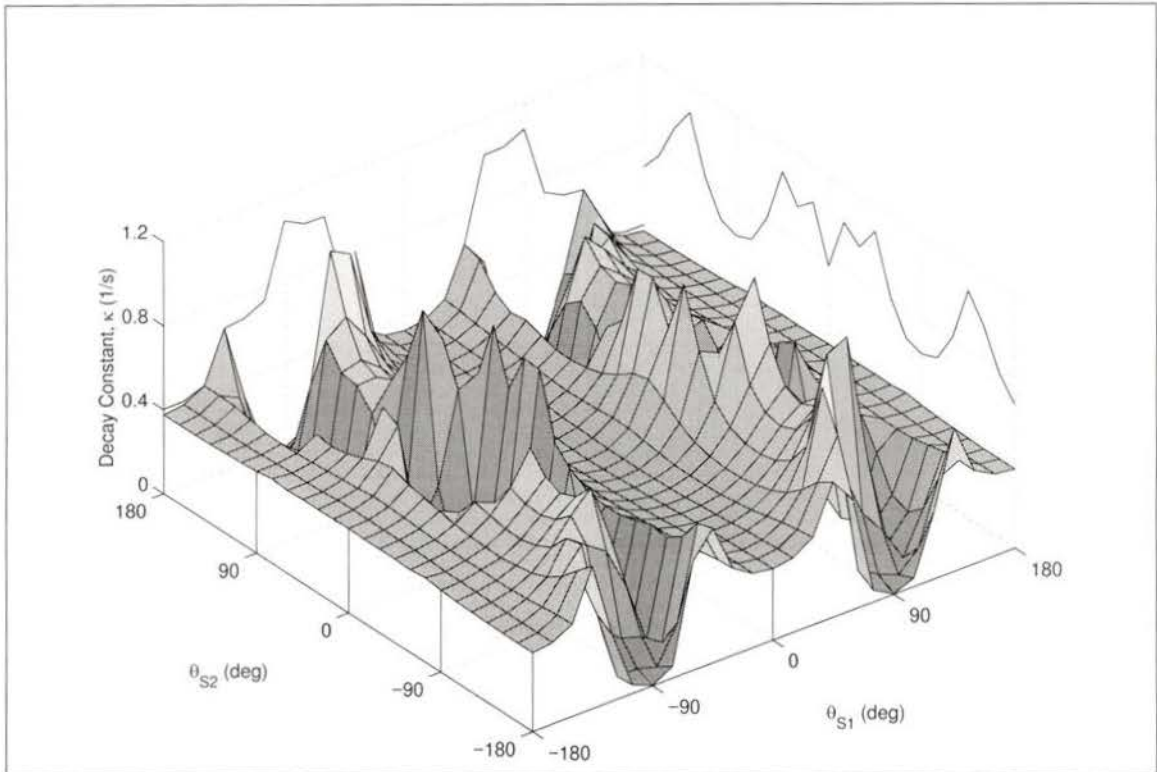


Figure 5.8: Observed Damping Performance for OLS Manipulator Using P-PEDA

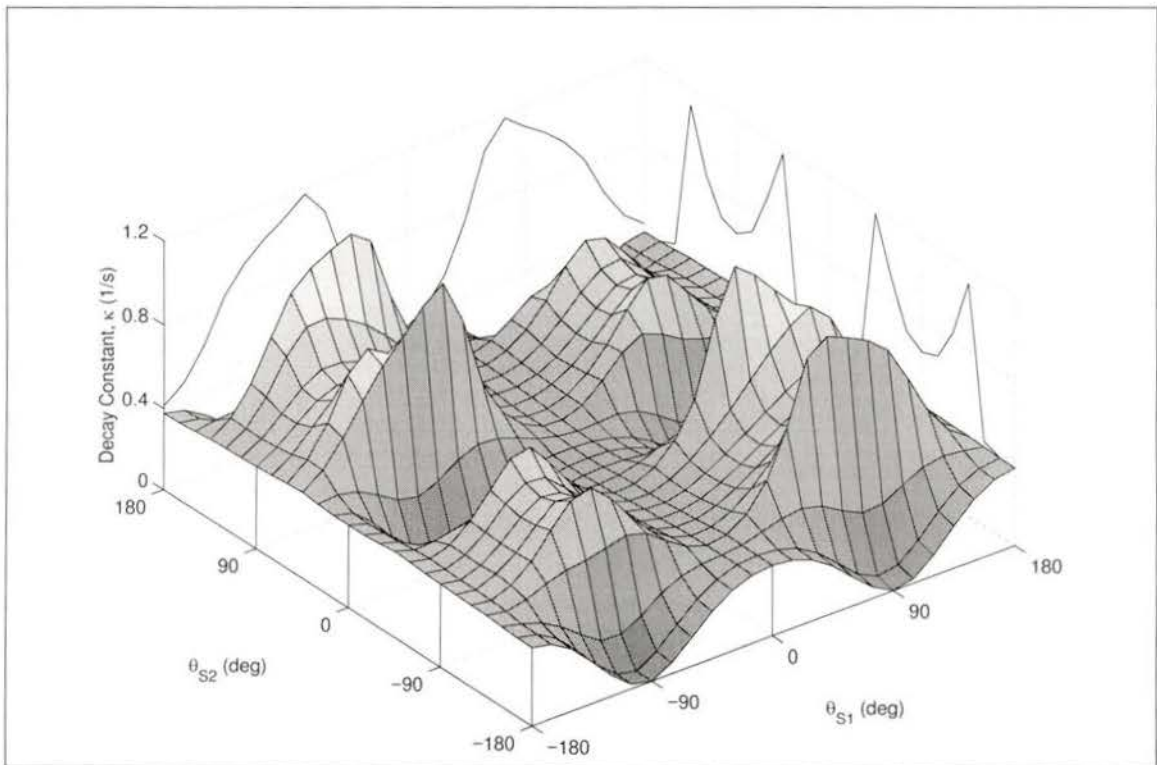


Figure 5.9: Observed Damping Performance for OLS Manipulator Using P-PEDB

## Impedance Matching

Using full gain matrices, it is possible, and even preferable, to tune all of the modes of SARA to the dominant (first) mode of the complete OLS manipulator. However, alternative diagonal gain matrices were developed in §3.4.2 since the full gain matrices led to SARA instability when implemented experimentally. It is not possible to tune all SARA modes to the single dominant modal frequency of the OLS manipulator using diagonal gain matrices. Instead, the first two SARA modes were tuned to the first *two* OLS manipulator modal frequencies. Simulations were performed using both the full and diagonal gain matrices, and the results were very similar. Only the diagonal gain matrix results are presented here to be consistent with the experimental results of Chapter 6.

The observed IM damping performance is shown in Figure 5.10. The same ‘truncated’ performance that was observed in the VS<sub>2</sub> results is seen here. Once again, the effect of the micro-manipulator compliance on the dominant modal frequency explains this effect; the fractional frequency error plotted in Figure 5.11 correlates well with the region of reduced performance.

The mean performance is  $\kappa = 0.46s^{-1}$ , slightly greater than the P-PED results, but the peak of  $\kappa = 0.87s^{-1}$  is considerably less than that from P-PED<sub>A</sub> or P-PED<sub>B</sub>. Potentially, the peak performance could be improved by adjusting the micro-manipulator gain matrices online. These adjustments would serve to adjust the micro-manipulator frequency,  $\omega_r$ , so that it follows the dominant elastic frequency  $\tilde{\omega}_e$ , which changes due to micro-manipulator compliance.

Even if the performance of the IM method can be improved in the central region by adjusting the frequency to which the manipulator is tuned, P-PED would still produce superior performance in other locations. The best active damping locations using P-PED are well away from the central region. It is therefore likely that a combination of IM and P-PED will yield better results over the entire range of SARA configurations.

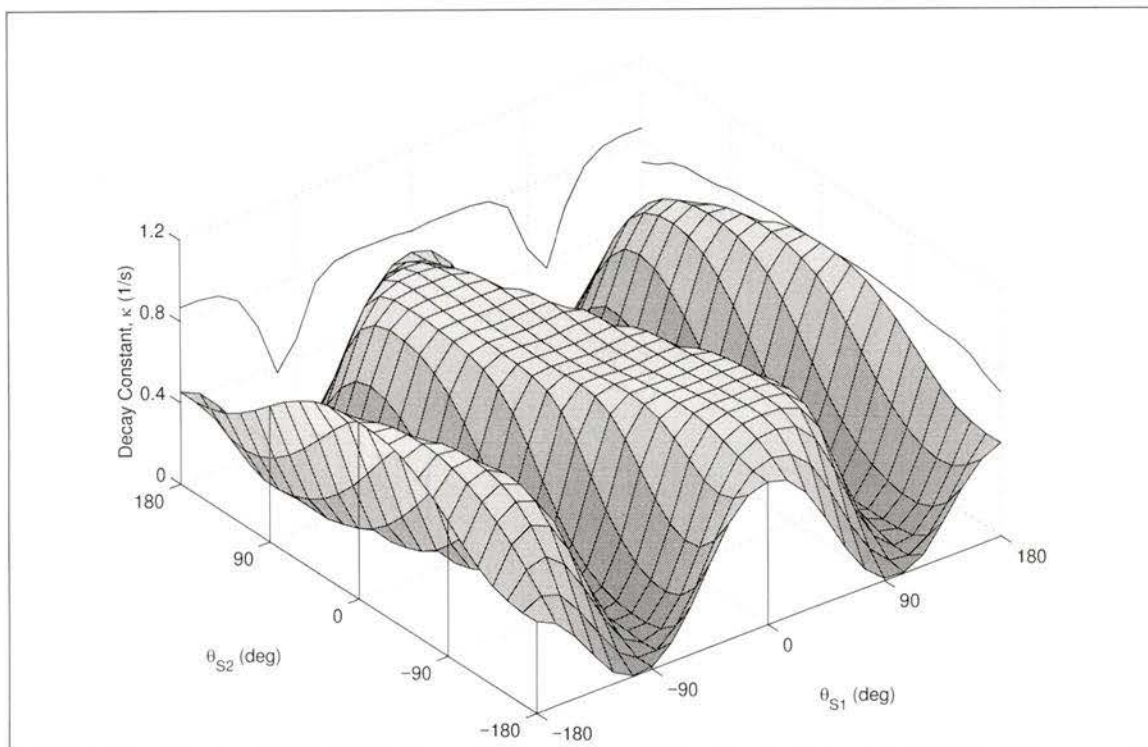


Figure 5.10: Observed Damping Performance for OLS Manipulator Using Impedance Matching

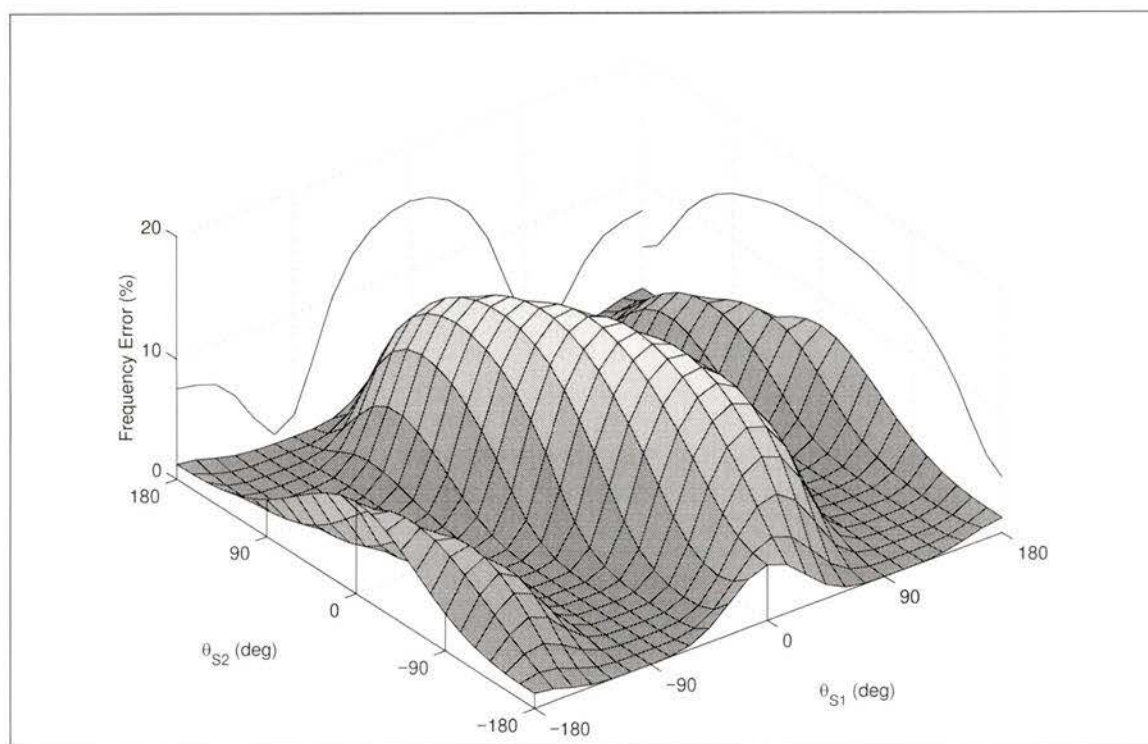


Figure 5.11: Change in Dominant (First) Modal Frequency of OLS Manipulator when IM Compliance is Introduced to SARA

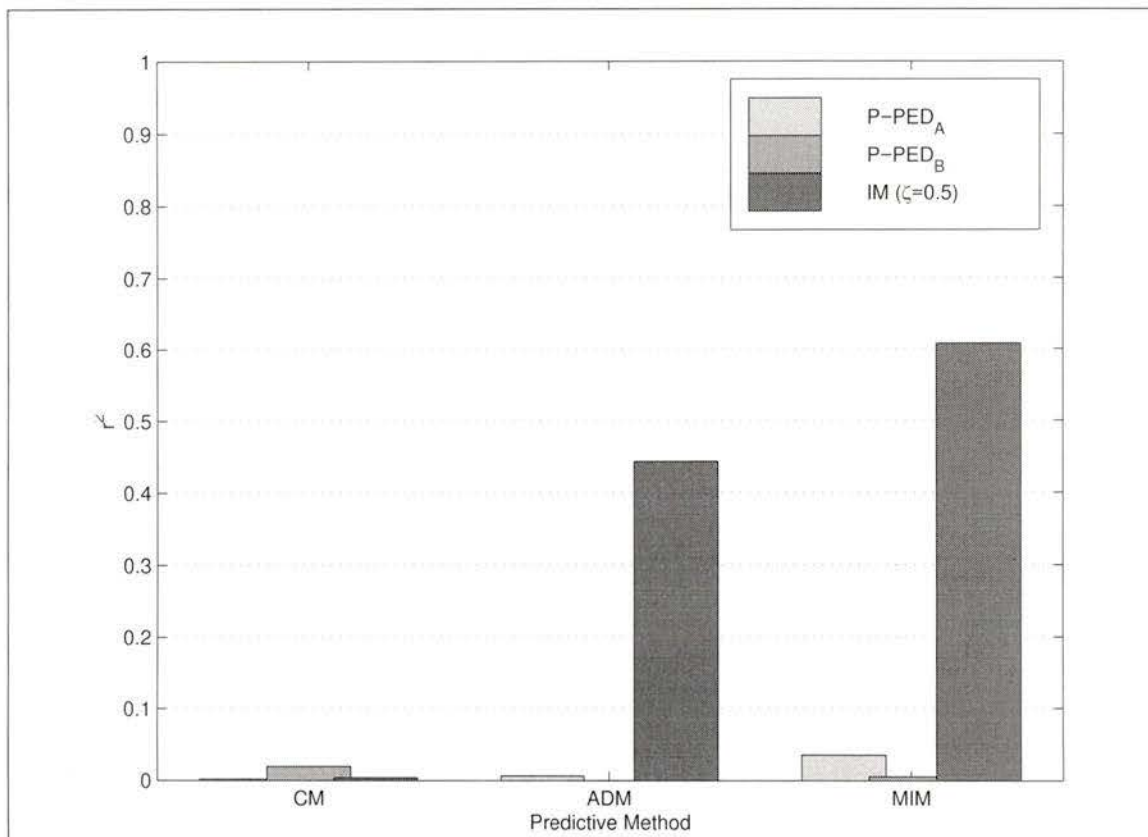


Figure 5.12: Contribution of CM, ADM, and MIM in Predicting the P-PED<sub>A</sub>, P-PED<sub>B</sub>, and Impedance Matching Damping Performance for OLS Manipulator

### 5.2.3 Performance Predictions

In Figure 5.12, the  $r^2$  values for the Coupling Map (CM), Accelerative Damping Map (ADM), and Modal Inertia Map (MIM) versus P-PED<sub>A</sub>, P-PED<sub>B</sub>, and Impedance Matching are plotted. In general, these values are much smaller than those for the VS manipulators. The CM, ADM, and MIM prediction maps are plotted in Figures 5.13 through 5.15 and are discussed below.

#### Coupling Map

The surface defined by the Coupling Map predictions, which is plotted in Figure 5.13, shows none of the features of P-PED<sub>A</sub>, P-PED<sub>B</sub>, or Impedance Matching performance surfaces. In fact, CM contributes almost nothing to predicting the performance of any of the methods, with a maximum  $r^2$  of only 0.02 versus P-PED<sub>B</sub>. When combined with the results from

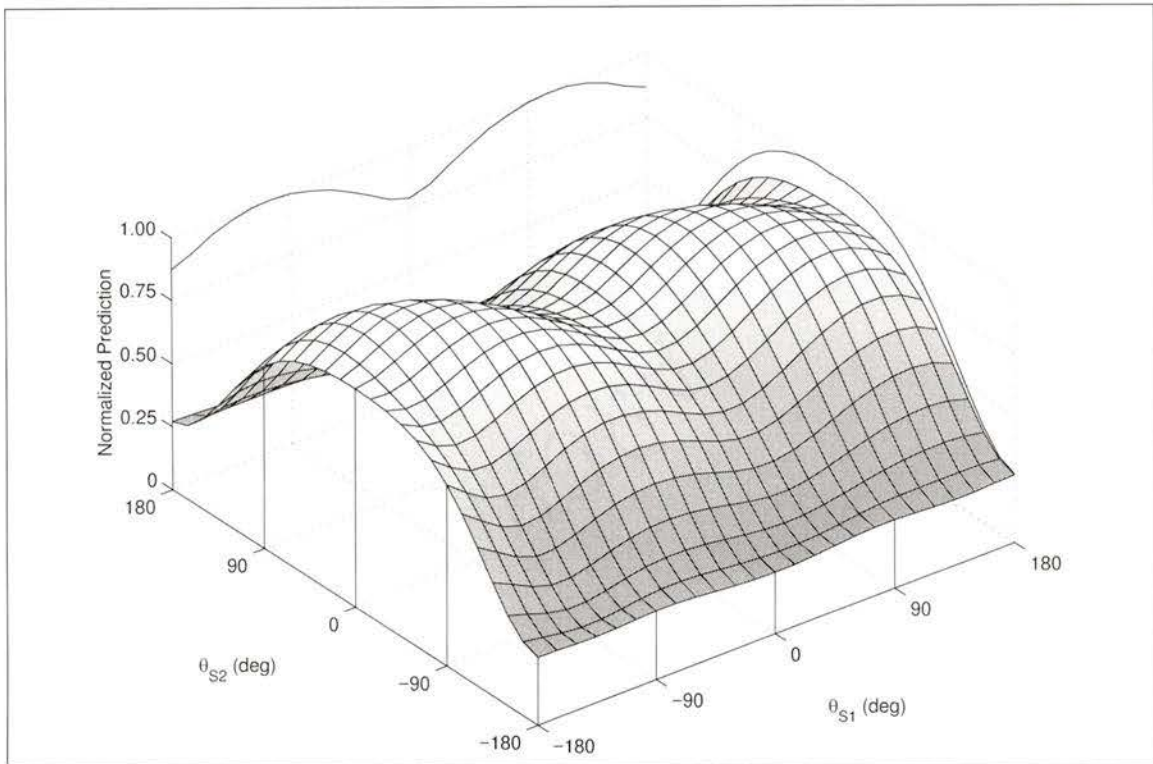


Figure 5.13: *Coupling Map Performance Predictions for OLS Manipulator*

the VS manipulators, this strongly suggests that the Coupling Map is not a good tool for determining the optimum micro-manipulator configurations for active damping.

### **Accelerative Damping Map and Modal Inertia Map**

Figures 5.14 and 5.15 show that the ADM and MIM predictions are once again similar. The central peak of the ADM surface is more pronounced than the corresponding MIM peak, but otherwise, the shapes of the two surfaces closely match.

Neither surface mimics the P-PED performance results, but they are relatively coherent with the IM surface. MIM is the better predictor of the two with  $r^2 = 0.61$ , compared to 0.44 from ADM. As was found with the VS<sub>2</sub> manipulator, the primary difference between the predictions and the IM performance is that the ‘truncated’ central region of the IM performance surface is not seen in the predictions.

The MIM method is based on accurate knowledge of the shape of the dominant mode of vibration. In §5.1.3, a mode shape error was introduced to quantify the change in the

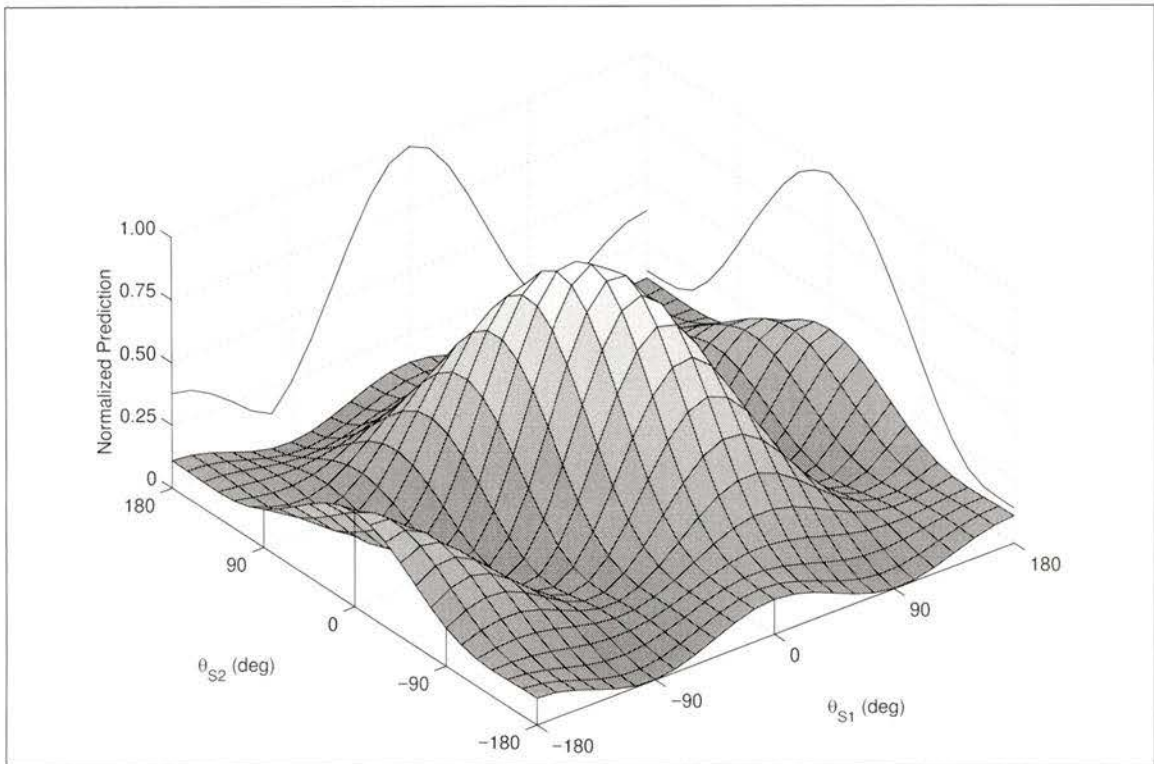


Figure 5.14: Accelerative Damping Map Performance Predictions for OLS Manipulator

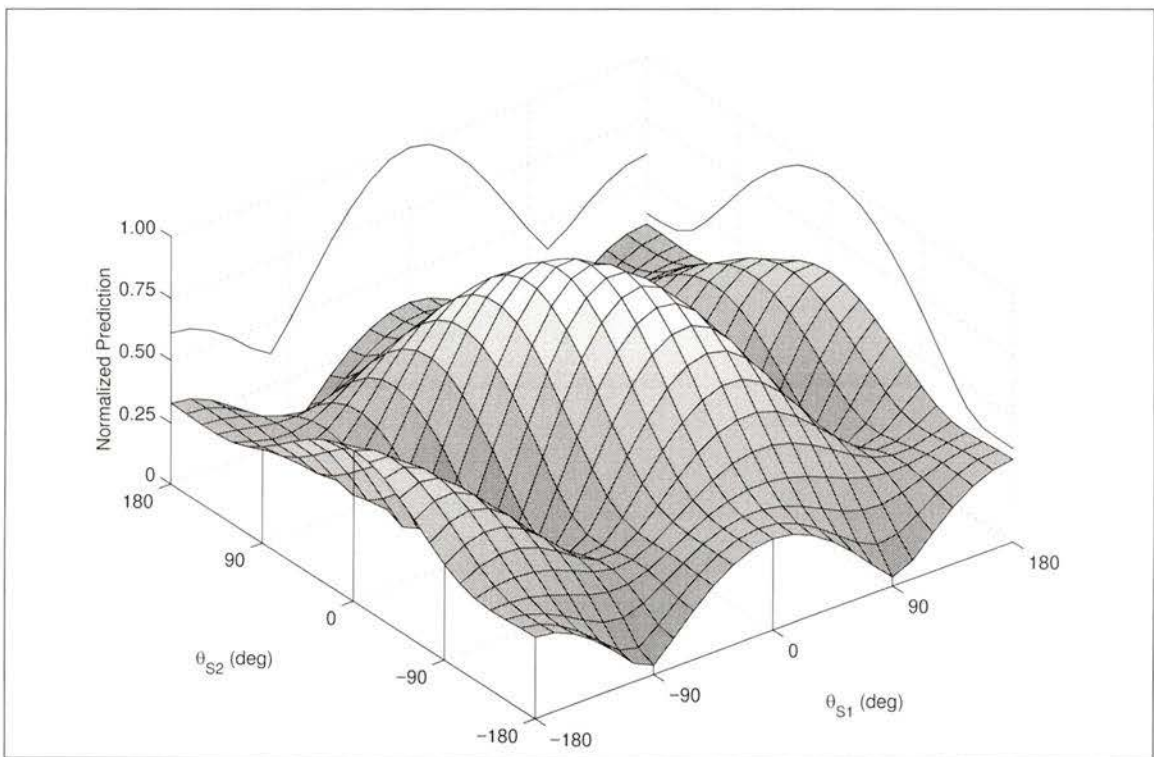


Figure 5.15: Modal Inertia Map Performance Predictions for OLS Manipulator

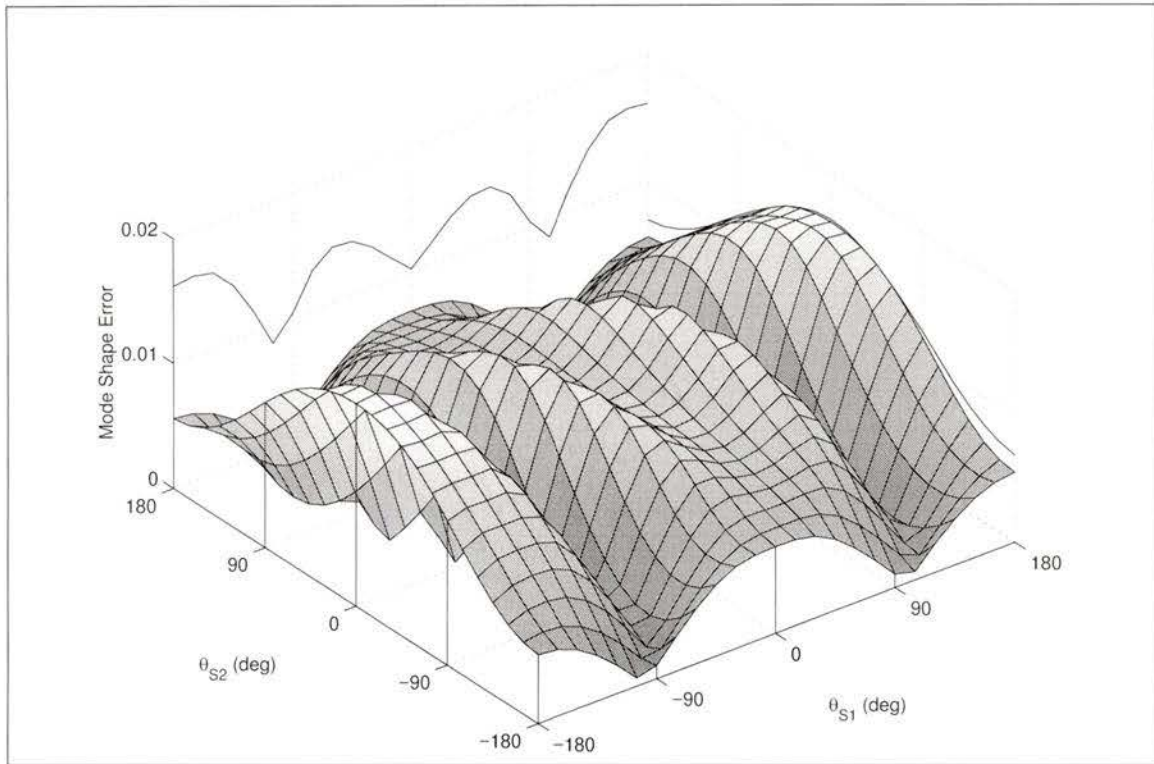


Figure 5.16: *Change in Shape of Dominant (First) Mode of OLS Manipulator when IM Compliance is Introduced to SARA*

mode shape due to the introduction of micro-manipulator compliance. It was shown that the mode shape changed little for the VS manipulators. The mode shape error for the OLS manipulator is plotted in Figure 5.16. The maximum error, 0.016, is again very small, suggesting that MIM is valid for reasonable micro-manipulator gain matrices.

### 5.3 Summary

For the VS manipulators, Impedance Matching resulted in far better damping performance than either P-PED<sub>A</sub> or P-PED<sub>B</sub>. Of the two P-PED methods, P-PED<sub>A</sub> gave better results but this was attributed to neglecting the rigid axial direction rather than a strength of the P-PED theory. The Impedance Matching performance curve for VS<sub>2</sub> contained a central depression around  $\bar{\theta}_r = 0^\circ$ , whereas the curves for the other three systems had peaks at this location. The depression, or ‘truncated’ performance, was attributed to changes in the dominant elastic modal frequency due to the introduction of micro-manipulator compliance.

The P-PED methods yielded better peak damping performance than Impedance Matching on the OLS manipulator. A central region of truncated performance was seen in the Impedance Matching results, similar to that seen on  $VS_2$ . It was again attributed to changes in the dominant elastic modal frequency. It was hypothesized that performance truncation could be limited by changing the tuned micro-manipulator frequency online.

The Coupling Map was a consistently poor predictor of damping performance. Both ADM and MIM, which gave similar predictions, predicted the Impedance Matching performance very well, except that the truncated performance was not seen in the predictions. Since MIM is predicated on accurate knowledge of the dominant mode shape, tests were performed to determine if this mode shape changes significantly when micro-manipulator compliance is introduced. It was shown to change very little, so MIM appears to be valid regardless of the micro-manipulator gains used for active damping.

## Chapter 6

# Experimental Results

The procedure for and results of experimental work on the LAURA-SARA manipulator are presented in this chapter. A detailed description of this manipulator was presented in Chapter 2. It is similar to the OLS manipulator of Chapter 5, except that two flexible links separated by the LAURA elbow joint (LAURA2) comprise the flexible structure of LAURA-SARA, rather than the single long flexible link of the OLS manipulator. The LAURA2 joint contributes both an internal degree of freedom and significant structural mass to LAURA.

### 6.1 Procedure

Experiments were performed with the LAURA2 joint locked at two different angles;  $\bar{\theta}_{L2} = -15^\circ$  and  $\bar{\theta}_{L2} = 60^\circ$ . The LAURA shoulder and elbow joints were held in their nominal configurations with proportional gains of 8000 and 4000 Nm/rad respectively. Although each of the LAURA links is essentially rigid axially, there is significant compliance in all directions when  $\bar{\theta}_{L2}$  is non-zero.

A standard elastic deflection was imposed and released at the SARA base at the start of each OLS manipulator simulation. Although this idealized procedure was useful for simulations, it is neither experimentally practical nor representative of how vibrations are excited in real manipulators. Typically, the macro-manipulator is used to deploy the micro-

Table 6.1: LAURA Deployment Details for LAURA-SARA Experiments

Test Configuration	Trajectory Description	LAURA1		LAURA2	
		Start	Finish	Start	Finish
LAURA2 at $-15^\circ$	$10^\circ/\text{s}$ for 3s	$-30^\circ$	$0^\circ$	$-45^\circ$	$-15^\circ$
LAURA2 at $60^\circ$	$6\frac{2}{3}^\circ/\text{s}$ for 3s	$-20^\circ$	$0^\circ$	$40^\circ$	$60^\circ$

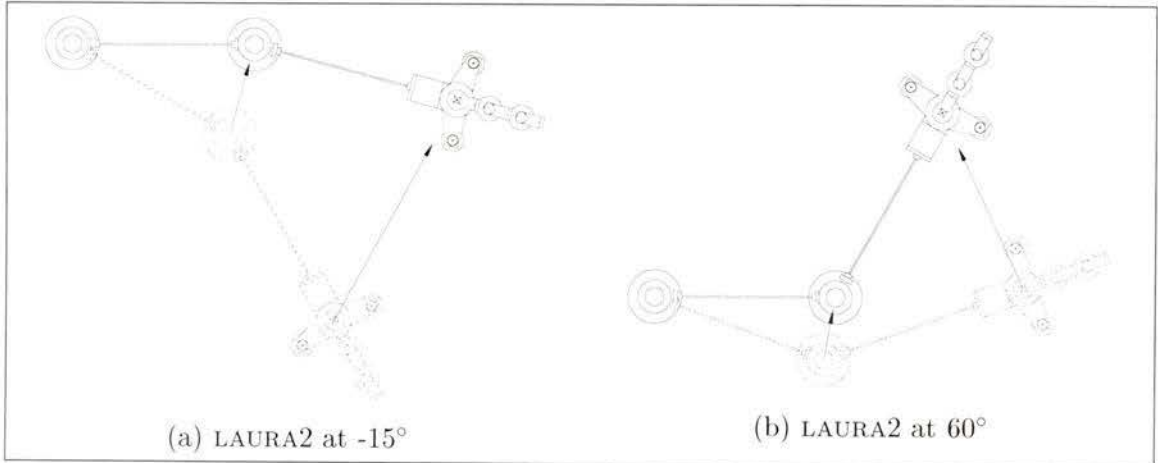


Figure 6.1: Deployment Maneuvers and LAURA Configurations for Experiments with LAURA-SARA Manipulator

manipulator to a work site and its joints are then locked while the micro-manipulator performs a task. Therefore, at the start of each experiment, LAURA was deployed to the test configuration with SARA controlled by stiff PD gains. The LAURA1 and LAURA2 deployment trajectories are summarized in Table 6.1 and illustrated in Figure 6.1. Constant joint rates were commanded for three seconds to move the joints to their desired end positions. After deployment, SARA was controlled with stiff PD gains for two seconds before switching to the appropriate P-PED or IM gains for active damping.

Example SARA base deflections and joint responses over the course of a typical experiment are plotted in Figure 6.2. The particular results shown are from a test using Impedance Matching with  $\bar{\theta}_{L2} = 60^\circ$ ,  $\bar{\theta}_{S1} = -45^\circ$ , and  $\bar{\theta}_{S2} = -90^\circ$ . The time index on all experiments starts at  $t = -5\text{s}$  so that SARA is switched from stiff gains to active damping gains at  $t = 0\text{s}$ . These results are typical in that the vibration is almost completely restricted to the first mode.

For both LAURA configurations, experiments were conducted over a grid of nominal

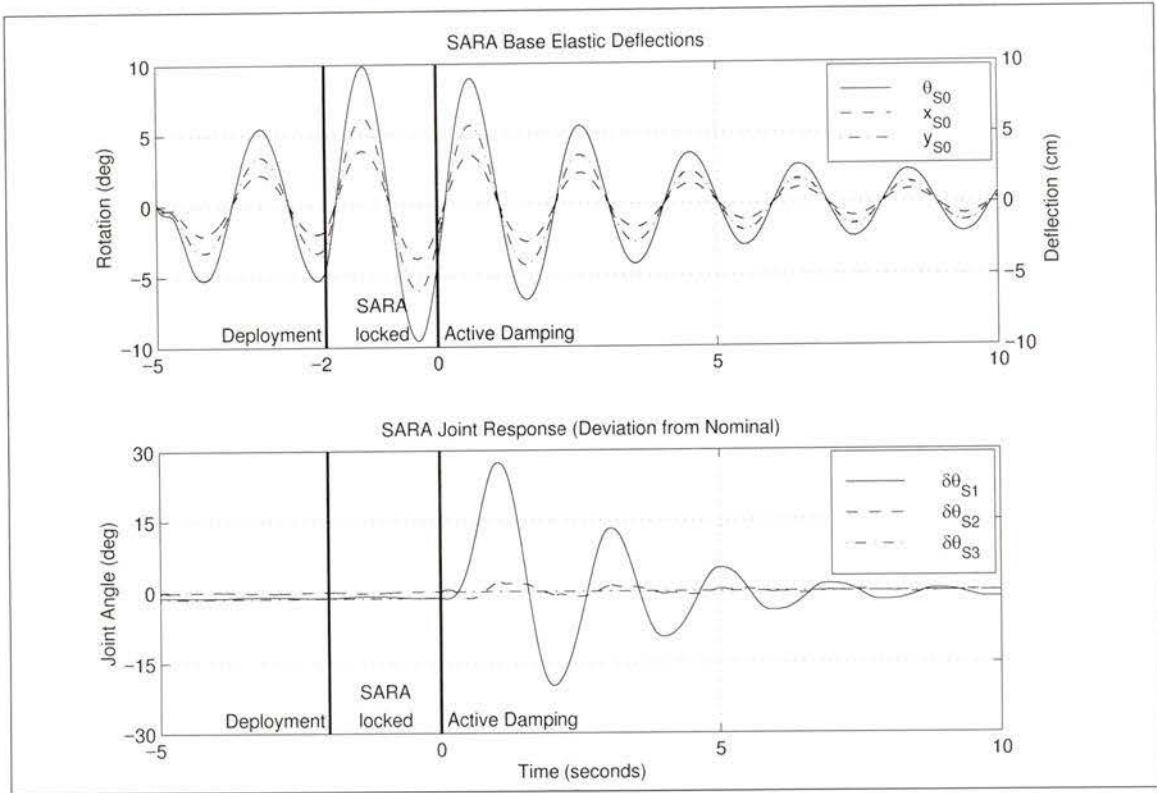


Figure 6.2: Representative SARA Base Elastic Deflections and Response of SARA Joints

SARA1 and SARA2 joint angles ( $\bar{\theta}_{S1}$  and  $\bar{\theta}_{S2}$ ) in  $45^\circ$  increments. As with the OLS manipulator simulations, SARA3 was nominally locked at  $0^\circ$  for all tests.

## 6.2 Damping Performance

The data from each experiment was analyzed offline to determine the decay constant,  $\kappa$ . The performance measured in this way ranged from a low of  $\kappa = 0.04s^{-1}$  to a high of  $\kappa = 1.23s^{-1}$ . Representative strain energy plots are shown in Figure 6.3. At the low end,  $\kappa = 0.04s^{-1}$  is near the small observed structural damping from the impact experiments of Chapter 2, where the joints of SARA were mechanically locked.

The surface plots which follow represent the measured damping performance over the complete range of SARA1 and SARA2 joint angles. Reference lines are drawn around the perimeter of each plot at  $90^\circ$  intervals to help locate surface features, and the height of these features can be determined from the projections of the surface peaks on the back planes.

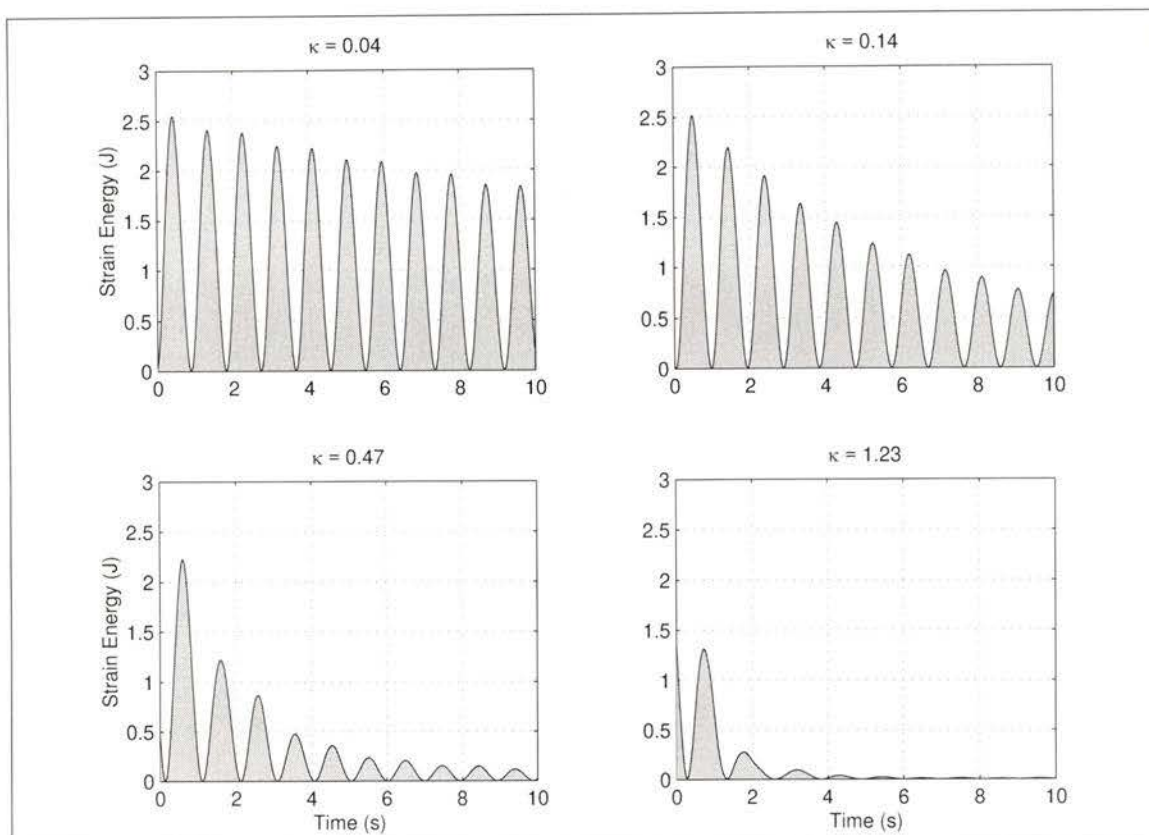


Figure 6.3: *Representative Strain Energy Plots Demonstrating the Range of Damping Performance Observed on the LAURA-SARA Manipulator*

## 6.2.1 Pseudo-Passive Energy Dissipation

### Implementation

Many of the potential P-PED implementation problems discussed in §3.3.4 arose with the LAURA-SARA manipulator. In particular, a significant macro-manipulator mass, coupled translational degrees of freedom at SARA's base, and instability when using the full P-PED matrices were present. The fourth potential problem, a poorly conditioned base stiffness matrix, was avoided by not performing any experiments with LAURA2 straight. Solutions as they apply to this particular manipulator are presented below using the definitions from §3.3.1 and §3.3.4.

The use of Guyan reduction was necessitated by the significant mass and internal degrees of freedom in LAURA. The resulting  $3 \times 3$  mass and stiffness matrices correspond to the elastic

coordinates of the SARA base, defined by the base coordinate vector  $\mathbf{q}_b = [x_{S0}, y_{S0}, \theta_{S0}]^T$ .

Using units of N, m, and radians, the reduced LAURA stiffness matrices are:

$$\text{LAURA2 at } -15^\circ: \quad \mathbf{K}_{b,-15^\circ} = \begin{bmatrix} 1.648e5 & 2.148e4 & -9.960e3 \\ 2.148e4 & 3.296e3 & -1.701e3 \\ -9.960e3 & -1.701e3 & 1.001e3 \end{bmatrix} \quad (6.1)$$

$$\text{LAURA2 at } 60^\circ: \quad \mathbf{K}_{b,60^\circ} = \begin{bmatrix} 8.826e3 & -4.680e3 & 2.077e3 \\ -4.680e3 & 3.316e3 & -1.711e3 \\ 2.077e3 & -1.711e3 & 1.006e3 \end{bmatrix} \quad (6.2)$$

It is immediately clear that the elastic base translations,  $x_b$  and  $y_b$ , are strongly coupled through the stiffness matrices. To obtain the orthogonal stiffness terms required to determine P-PED gains, the above stiffness matrices were diagonalized as per §3.3.4 to give:

$$\text{LAURA2 at } -15^\circ: \quad \hat{\mathbf{K}}_{b,-15^\circ} = \begin{bmatrix} 22550 & 0 \\ 0 & 498 \end{bmatrix} \quad (6.3)$$

$$\text{LAURA2 at } 60^\circ: \quad \hat{\mathbf{K}}_{b,60^\circ} = \begin{bmatrix} 7737 & 0 \\ 0 & 658 \end{bmatrix} \quad (6.4)$$

The condition numbers of  $\hat{\mathbf{K}}_{b,-15^\circ}$  and  $\hat{\mathbf{K}}_{b,60^\circ}$  are 45.3 and 11.8 respectively. By contrast, the condition number of the LAURA stiffness matrix when  $\bar{\theta}_{L2} = 0^\circ$  ( $\hat{\mathbf{K}}_{b,0^\circ}$ , not shown), where the arm is nearly rigid axially, is 46 320. Unlike the simulations, both base translational degrees of freedom were used to calculate the gain matrices for experimental work.

The final difficulty in implementing P-PED was that SARA was unstable when using the full gain matrices. As described in §3.3.4, the off-diagonal terms were simply dropped for all experimental work presented here.

In a few configurations, SARA was stable using full gain matrices, but the damping performance using the full matrices was worse than the diagonal matrix results presented below. Some experiments were also conducted using gains calculated directly from  $\mathbf{K}_{b,-15^\circ}$

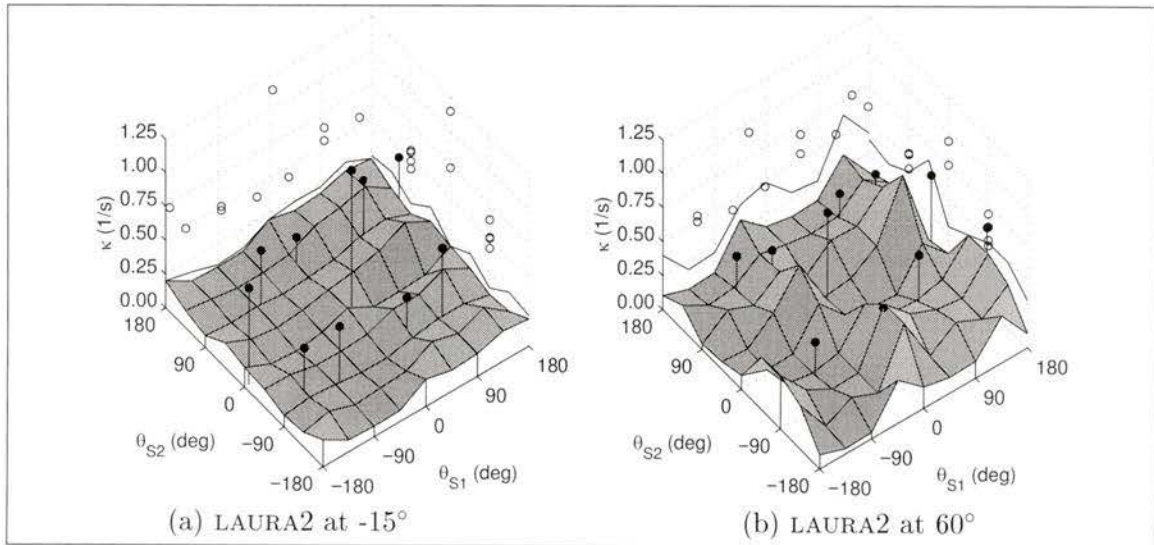


Figure 6.4: Measured Damping Performance on LAURA-SARA Manipulator Using P-PED

and  $\mathbf{K}_{b,60^\circ}$  (without first decoupling the base translation terms), again with results worse than those presented below.

## Results

Plots of the measured damping performance using P-PED at both LAURA configurations are shown in Figure 6.4. Compared to the OLS manipulator results in Chapter 5, the measured performance on the regularly spaced grid of  $\bar{\theta}_{S1}$  and  $\bar{\theta}_{S2}$  angles is in general very poor. This poor performance is explained by the dominance of the stiff translational direction in calculating the P-PED gains. The result is large SARA proportional and derivative gains and poor damping performance.

In certain SARA configurations, however, the stiff translation direction has little effect on the gains calculation. At these configurations, SARA joint accelerations result in base reaction forces which are primarily aligned with the ‘soft’ translational directions. Additional experiments, marked by individual points above the surface plots, were performed at some of these configurations with much improved damping performance.

Dropping the off-diagonal terms from the full P-PED gain matrices is another possible cause for the poor observed performance. Nevertheless, it was necessary to do so as SARA

was unstable when controlled with the full matrices. Also, as mentioned above, at the few configurations where SARA was stable with full gain matrices, the observed damping performance was worse than the diagonal matrix results presented here. Guyan reduction and translational direction decoupling are other potential culprits, but they were both also required to experimentally implement P-PED.

## 6.2.2 Impedance Matching

### Implementation

Equation (3.32) in §3.4.1 was a very simple method of calculating full Impedance Matching gain matrices,  $\mathbf{P}_{IM}$  and  $\mathbf{D}_{IM}$ . Unfortunately, SARA was unstable when controlled with these matrices, so alternative diagonal matrices were developed in §3.4.2. These alternative matrices were used for all Impedance Matching experiments and also for the OLS manipulator simulations presented in Chapter 5. A damping ratio,  $\zeta$ , of 0.5 was used for both the OLS simulations and the LAURA-SARA experiments.

In developing the diagonal gain matrices, SARA was tuned to both the first and second elastic modal frequencies. However, as was seen in Figure 6.2, the LAURA vibration and thus the SARA response was dominated by the first mode.

### Results

Measured damping performance plots for the two LAURA configurations are shown in Figure 6.5. The two surfaces are nearly identical with the exception of a small shift in the  $\theta_{S1}$  direction.

The peak performance values with LAURA2 at  $-15^\circ$  and LAURA2 at  $60^\circ$  are  $\kappa = 1.16s^{-1}$  and  $\kappa = 1.23s^{-1}$  respectively, and the corresponding mean values are  $0.43s^{-1}$  and  $0.37s^{-1}$ . The measured performance surfaces are also very similar both in scale and shape to the OLS manipulator simulation results (§5.2.2). The primary difference is that the truncated central region of the simulation results is not present in the surfaces of Figure 6.5. This truncation

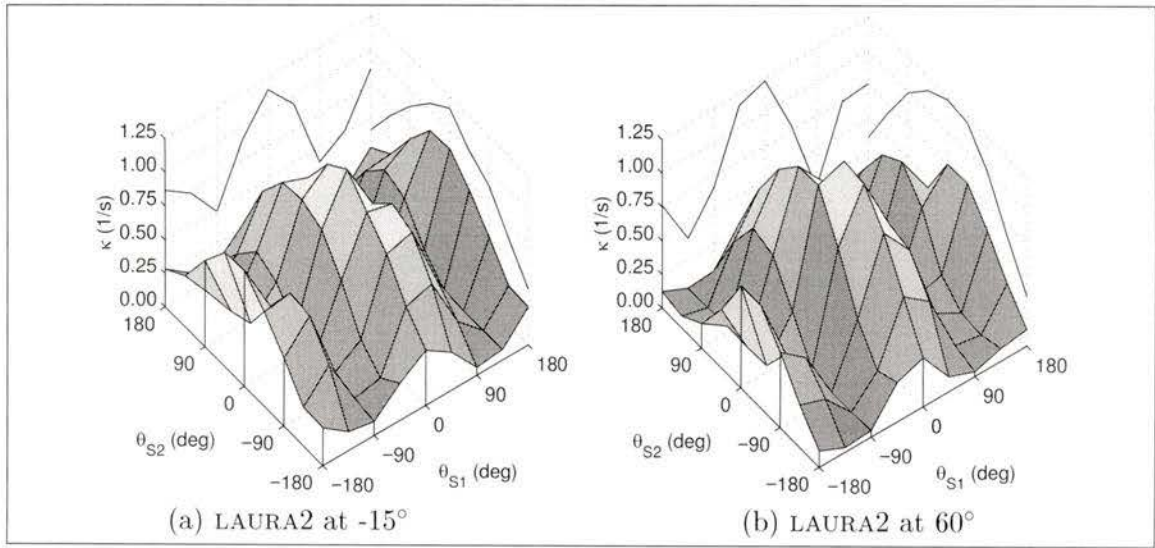


Figure 6.5: Measured Damping Performance on LAURA-SARA Manipulator Using Impedance Matching

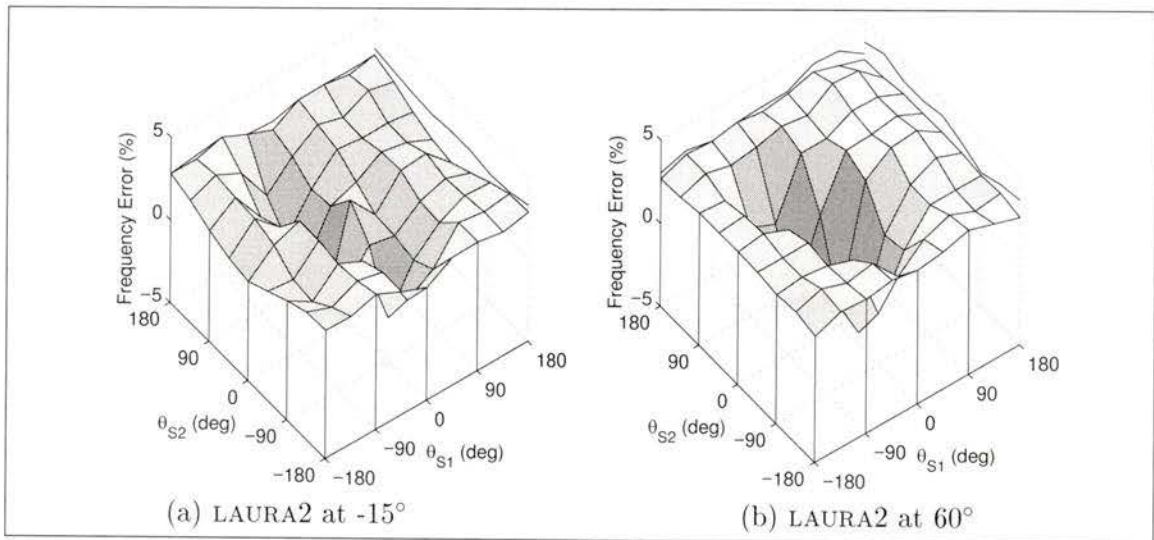


Figure 6.6: Change in Frequency of Dominant Mode of LAURA-SARA Manipulator when IM Compliance is Introduced to SARA

was attributed to a large change (as much as 15%) in the dominant modal frequency when compliance was introduced to SARA in the form of the  $\mathbf{P}_{IM}$  and  $\mathbf{D}_{IM}$  gain matrices. As shown in Figure 6.6, the change in  $\tilde{\omega}_e$  for the LAURA-SARA manipulator is less than 5%. The lesser change in the dominant modal frequency is likely due to the extra mass in the flexible structure, so that the effect of SARA compliance on the complete system is smaller.

The similarity between the two IM surfaces in Figure 6.5 is explained by a comparison

Table 6.2: First Mode Shape of LAURA-SARA Manipulator with SARA Locked in Straight-Out Configuration

LAURA Configuration	Mode Shape		
	$x_{S0}$ (m)	$y_{S0}$ (m)	$\theta_{S0}$ (rad)
LAURA2 at $-15^\circ$	-0.049	0.701	0.711
LAURA2 at $60^\circ$	0.167	0.640	0.750

of the first elastic mode shape in each LAURA configuration. In Table 6.2, these mode shapes, expressed in the SARA base frame and calculated with SARA locked in the straight-out configuration, are shown. There is very little difference between the mode shapes. Since the SARA base motion changes little between LAURA configurations, the damping performance curves are also mostly unchanged.

## 6.3 Performance Predictions

### 6.3.1 Prediction Maps

The Coupling Maps, Accelerative Damping Maps, and Modal Inertia Maps for the LAURA-SARA manipulator are plotted in Figures 6.7, 6.8, and 6.9 respectively. The maps are plotted at  $15^\circ$  intervals, rather than the  $45^\circ$  intervals used in the experiments, to better show small details in the surfaces.

The LAURA-SARA Coupling Map has a very simple structure, with the predicted performance a function almost exclusively of the nominal SARA elbow angle,  $\bar{\theta}_{S2}$ . The peak predicted performance occurs at  $\bar{\theta}_{S2} = 0$ , and the performance drops as  $\bar{\theta}_{S2}$  increases until reaching minima at  $\bar{\theta}_{S2} = \pm 180^\circ$ . This shape is similar to that obtained for the OLS manipulator in Chapter 5, although there was slightly more dependance on  $\bar{\theta}_{S1}$  for that manipulator.

It is worth noting that Guyan reduction was required to generate the Coupling Maps for LAURA-SARA, but was not required for the OLS manipulator. The fact that the respective maps are similar in shape bodes well for the Guyan reduction procedure.

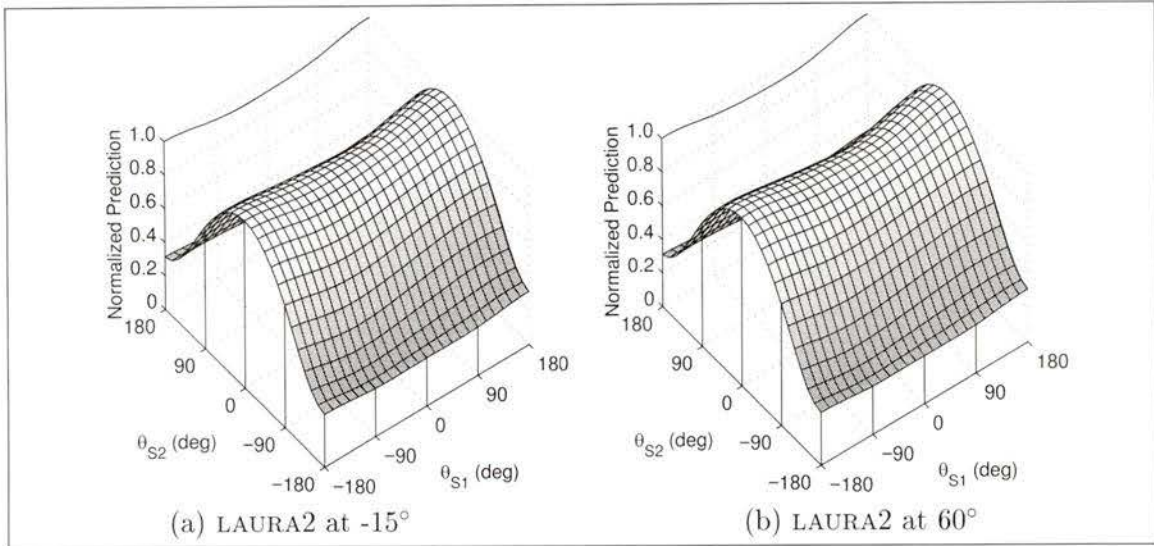


Figure 6.7: *Normalized Coupling Maps for LAURA-SARA Manipulator*

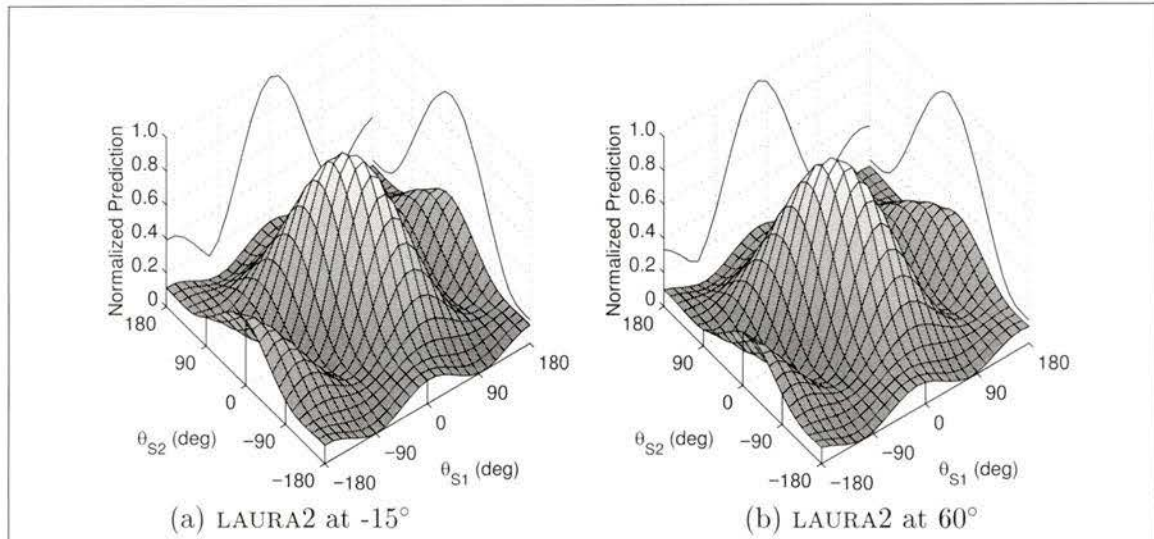


Figure 6.8: *Normalized Accelerative Damping Maps for LAURA-SARA Manipulator*

In Chapter 5, the ADM and MIM plots for a given manipulator were invariably similar in shape. This pattern continues with the maps plotted in Figures 6.8 and 6.9. Once again, the primary difference is that the central peak is more prominent in the ADM.

Except for a small shift in the location of the central peak, there is very little difference in the maps with LAURA2 at  $-15^\circ$  and LAURA2 at  $60^\circ$ . Each is also very similar to the corresponding OLS manipulator plots, especially the maps with LAURA2 at  $-15^\circ$ .

The similarity of the prediction maps between LAURA configurations is explained by the

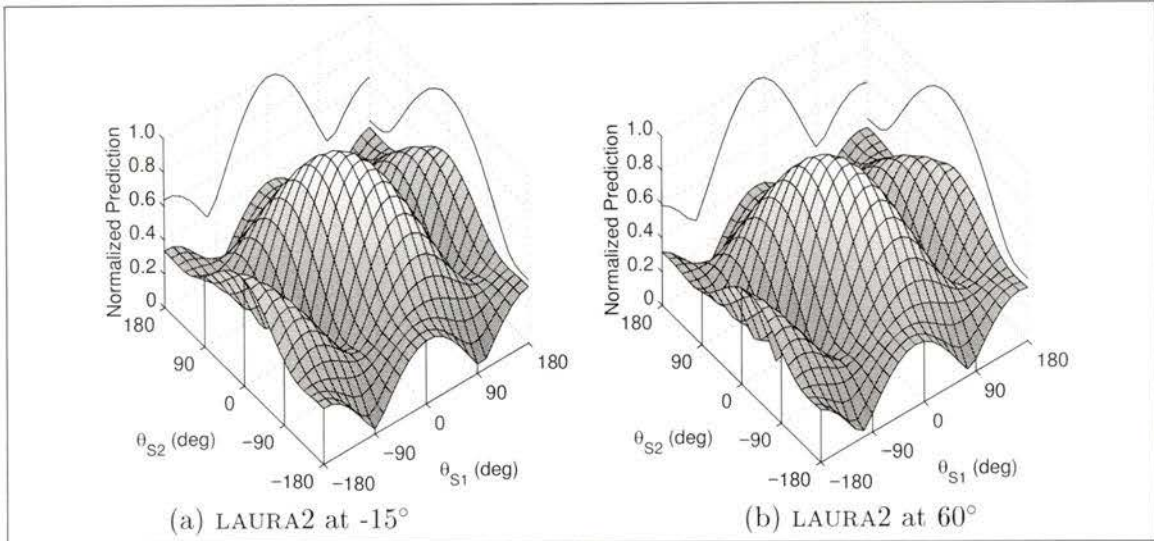


Figure 6.9: *Normalized Modal Inertia Maps for LAURA-SARA Manipulator*

similarity in the corresponding mode shapes when expressed in the SARA base frame, as explained in the discussion of the Impedance Matching results.

### 6.3.2 Correlations

The coefficient of determination,  $r^2$ , is a measure of the contribution of a particular map in determining the shape of a particular observed performance surface. The  $r^2$  values for each predictive map versus the experimental data are plotted in Figure 6.10.

The results in Figure 6.10 closely mimic those seen with the OLS manipulator and even the VS manipulators in Chapter 5. The Coupling Map is once again a very poor predictor of damping performance for both P-PED and Impedance Matching. The Accelerative Damping Map and Modal Inertia Map predict the Impedance Matching results very well, with  $r^2$  ranging from 0.77 to 0.90, but do not perform nearly as well against P-PED, with a peak  $r^2$  of only 0.07. The MIM was slightly better predictor of Impedance Matching performance than the ADM.

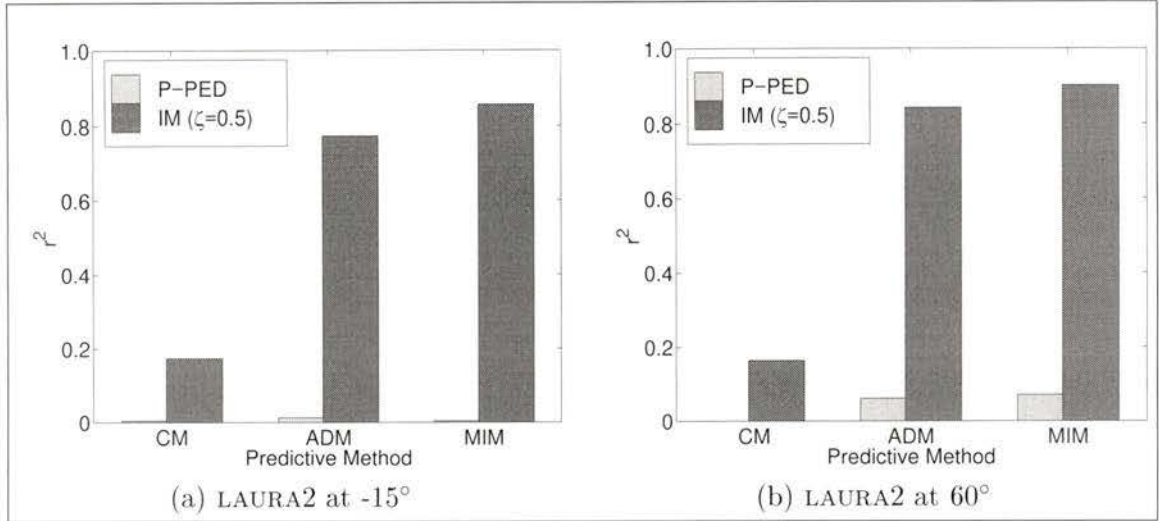


Figure 6.10: Contribution of CM, ADM, and MIM towards Predicting the P-PED and IM Damping Performance on the LAURA-SARA Manipulator

## 6.4 Summary

The P-PED damping performance for the LAURA-SARA manipulator was much worse than what would be expected from the OLS manipulator simulation results. Three potential reasons were given:

- relatively poor condition of LAURA stiffness matrix;
- limitations of Guyan reduction procedure;
- limitations of the stiffness matrix diagonalization procedure.

Evidence in the form of additional experiments at special SARA configurations supported the first explanation. Although the other two could not be refuted, they were both necessary to implement P-PED experimentally.

The damping performance of the Impedance Matching algorithm was considerably better than the corresponding P-PED performance, with nearly identical results for both LAURA configurations. Furthermore, the surfaces of measured performance were comparable both in shape and magnitude to the OLS manipulator simulation results. A significant difference was that the central plateau seen in the OLS surface was missing from the LAURA-SARA results. This difference was explained by the observation that the dominant modal frequency of

the LAURA-SARA manipulator changed little when IM compliance was introduced to SARA, whereas the change was significant with the OLS manipulator.

As was the case with the simulation results in Chapter 5, the Modal Inertia Map was the best predictor of IM damping performance, with the Accelerative Damping Map close behind. Neither predicted the P-PED damping performance well. The Coupling Map was again a poor predictor of either P-PED or IM damping performance.

## Chapter 7

# Conclusions

There were two primary objectives to this research. The first was to develop and implement methods of actively damping macro-manipulator vibrations using a distal end micro-manipulator, and the second to determine the optimal micro-manipulator configurations for this active damping. In the following pages, the procedure and theory required to meet these objectives, and the simulation and experimental results are summarized.

Macro-micro manipulators and their practical advantages were introduced in Chapter 1. These manipulators evolved out of the need for lightweight manipulators with a large works pace and accurate end-effector control. The small, rigid micro-manipulator performs the required tasks after being deployed to a work site by the large, flexible macro-manipulator. Residual macro-manipulator vibrations after deployment can be rapidly dissipated by the micro-manipulator if an appropriate active damping strategy is used and the micro-manipulator is effectively configured.

A number of published active damping control strategies were summarized. It was however noted that there has been little prior research effort towards determining the optimal micro-manipulator configurations for active damping.

An experimental macro-micro manipulator (the LAURA-SARA manipulator) was developed specifically to meet the research objectives, and is described in detail in Chapter 2. Design details were presented, followed by the development of a numerical model which

was validated experimentally in the frequency domain. The average frequency errors for the first two modes based on the numerical model were under 8%. The suspected cause of the frequency errors was unmodelled compliance, and in particular the cantilevered beam assumption used to model the flexible links.

A description of the LAURA-SARA control system was also given in Chapter 2. Two dedicated DSP boards in a host PC perform all control calculations at up to 4000 Hz. The host PC handles user interface and data archive duties. A message-based system is used to coordinate the PC and DSP's.

Two active damping strategies, Pseudo-Passive Energy Dissipation (P-PED) and Impedance Matching (IM), were first introduced in Chapter 3. P-PED was originally developed by Torres [21, 23], but it was extended in this work for application to a broader range of macro-micro manipulators. Torres' iterative root-locus procedure for calculating the P-PED gains was also replaced by a direct analytical solution. The Impedance Matching algorithm is an original contribution of this thesis. It does not require significant modelling assumptions and is therefore simple to implement on real manipulators.

Both the P-PED and IM methods produce full micro-manipulator proportional and derivative gain matrices. However, when the methods were implemented experimentally, SARA was unstable when controlled with these full matrices. As suggested by Torres, the off-diagonal elements of the P-PED gain matrices were simply dropped. An alternative development of the Impedance Matching algorithm, which led to diagonal gain matrices, was introduced.

Three tools for predicting the optimal micro-manipulator configurations for active damping were introduced in Chapter 4. The first, the Coupling Map, was originally devised for path-planning [21, 22], and is based on momentum conservation. Unfortunately, many of the original assumptions which were valid for path-planning were problematic for active damping. The Accelerative Damping Map was the second tool and is an original contribution. It was developed specifically for predicting active damping performance and is calculated

from the macro-manipulator tip wrench applied when the micro-manipulator joints accelerate from rest. Another original contribution, the Modal Inertia Map was also developed as a prediction tool. Its basis is the degree to which dominant mode macro-manipulator vibrations excite micro-manipulator joint motions.

Simulation results on four very simple (VS) manipulators and a simplified version of the LAURA-SARA manipulator (the OLS manipulator) were presented in Chapter 5. The damping performance using Impedance Matching was much better than that using P-PED on the VS manipulators. The damping performance from the two methods was comparable on the OLS manipulator.

An interesting feature in the Impedance Matching results for the OLS manipulator and one of the VS manipulators was a region of truncated performance near the straight-out micro-manipulator configuration. It was hypothesized that online adjustments of the micro-manipulator gain matrices would lead to improved IM damping performance in this region.

Throughout the simulation results, the Coupling Map was a very poor predictor of damping performance. The Accelerative Damping Map and Modal Inertia Map yielded very similar predictions, which also correlated well with the observed damping performance using Impedance Matching.

Calculation of the Modal Inertia Map requires accurate knowledge of the dominant mode shape. Unlike the dominant modal frequency discussed above, the dominant mode shape was shown to change little when joint compliance was introduced to the micro-manipulator. The Modal Inertia Map should therefore be valid regardless of the choice of active damping gain matrices.

Finally, experimental results on the complete LAURA-SARA manipulator were presented in Chapter 6. Compared to the OLS manipulator, P-PED performed very poorly on the LAURA-SARA manipulator. This was attributed to implementation differences, particularly in the treatment of stiff macro-manipulator directions. The experimental Impedance Matching results were significantly better than the experimental P-PED results. Also, the trun-

cated performance region seen in the OLS manipulator simulation results was not present in the experimental results.

The Modal Inertia Map and Accelerative Damping Map were again similar in shape to each other and to the Impedance Matching results. None of the maps predicted the P-PED damping performance well, and the Coupling Map was also a poor predictor of the Impedance Matching results.

Overall, Impedance Matching was found to be much simpler to implement on a physical manipulator than P-PED, and also generally yielded superior damping performance. Both the Accelerative Damping Map and the Modal Inertia Map effectively predict the relative damping performance over the range of micro-manipulator configurations. Either can be used to determine the nominal micro-manipulator configurations at which Impedance Matching should be employed.

Better Impedance Matching performance may be obtained through further research. In particular, the effect of different micro-manipulator damping ratios,  $\zeta$ , and of adjusting the ‘tuned’ micro-manipulator frequencies online should be investigated. It would also be informative to compare some of the other active damping strategies outlined in Chapter 1 both to each other and to the CM, ADM, and MIM predictions.

# References

- [1] Wayne J. Book and Soo Han Lee. Vibration Control of a Large Flexible Manipulator by a Small Robotic Arm. In *Proc. American Control Conference*, pages 1377–1380, 1989.
- [2] David W. Cannon. Command Generation and Inertial Damping Control of Flexible Macro-Micro Manipulators. Master's thesis, Georgia Institute of Technology, May 1996.
- [3] David W. Cannon, David P. Magee, and Wayne J. Book. Experimental Study on Macro/Mico Manipulator Vibration Control. In *Proc. IEEE International Conference on Robotics and Automation*, pages 2549–2554, April 1996.
- [4] Yasuhiko Dote. *Servo Motor and Motion Control Using Digital Signal Processors*. Prentice Hall and Texas Instruments, 1990.
- [5] Bernard Friedland. *Control System Design: An Introduction to State Space Methods*. McGraw-Hill, Inc., Toronto, Ontario, 1986.
- [6] Robert J. Guyan. Reduction of Stiffness and Mass Matrices. *AIAA Journal*, 3(2):380, 1964.
- [7] Inland Motor: Kollmorgen Corporation, Radford, Virginia. *Direct Drive DC Motors*. Catalog of direct drive motors with engineering design information.
- [8] Soo Han Lee. *Robust Control of a Flexible Link Robot and Rigid Link Robot: Theory, Simulation, and Experiment*. PhD thesis, Georgia Institute of Technology, March 1992.
- [9] Soo Han Lee and Wayne J Book. Robot Vibration Control Using Inertial Damping Forces. In *Proceedings of VIII CISM-IFTOMM Symposium on the Theory and Practice of Robots and Manipulators (Ro.Man.Sy.'90)*, July 1990.
- [10] Jae Y. Lew and Dan J. Trudnowski. Vibration Control of a Macro/Micro-Manipulator System. *IEEE Control Systems*, pages 26–31, 1996.
- [11] Jae Y. Lew, Dan J. Trudnowski, Mark S. Evans, and David W. Bennett. Micro Manipulator Motion Control to Suppress Macro Manipulator Structural Vibrations. In *Proc. IEEE International Conference on Robotics and Automation*, pages 3116–3120, 1995.
- [12] James T. McClave and Frank H. Dietrich. *A First Course in Statistics*. Maxwell MacMillan Canada, Toronto, fourth edition, 1992.

- [13] M. Nahon, C. Damaren, A. Bergen, and J. Goncalves. A Test Facility for Multi-armed Space-based Manipulators. *Canadian Aeronautics and Space Journal*, 41(4):150–162, 1995.
- [14] Singenesu S. Rao. *Mechanical Vibrations*. Addison–Wesley, Don Mills, Ontario, second edition, June 1990.
- [15] I. Sharf. Active Damping of a Large Flexible Manipulator with a Short-Reach Robot. In *Proceedings of the American Control Conference*, pages 3329–3333, June 1995.
- [16] I. Sharf. Active Damping of a Large Flexible Manipulator with a Short-Reach Robot. *ASME Journal of Dynamic Systems Measurement and Control*, 118:704–713, 1996.
- [17] J. Stanway, I. Sharf, and C. Damaren. Validation of a Dynamics Simulation for a Structurally Flexible Manipulator. In *Proc. IEEE International Conference on Robotics and Automation*, volume 3, pages 1959–1965, 1996.
- [18] J. Stanway, J. Wright, J. Van Vliet, C. Damaren, M. Nahon, and I. Sharf. Dynamics Validation and Control with a Dual-Arm Flexible Manipulator Test-Bed. In *Proceedings of the 9th CASI Conference on Astronautics*.
- [19] Jefferson Steven Graham Stanway. Validation of a Dynamics Simulation for a Structurally Flexible Manipulator. Master’s thesis, University of Victoria, 1996.
- [20] William T. Thomson. *Theory of Vibration with Applications*. Prentice Hall, Englewood Cliffs, New Jersey, fourth edition, 1993.
- [21] Miguel A. Torres. *Modeling, Path-Planning, and Control of Space Manipulators: The Coupling Map Concept*. PhD thesis, Massachusetts Institute of Technology, May 1993.
- [22] Miguel A. Torres and Steven Dubowsky. Path-Planning for Elastically Constrained Space Manipulator Systems. In *Proc. IEEE International Conference on Robotics and Automation*, May 1993.
- [23] Miguel A. Torres, Steven Dubowsky, and Attilio C. Pisoni. Vibration Control of Deployment Structures’ Long-Reach Space Manipulators: The P-PED Method. In *Proc. IEEE International Conference on Robotics and Automation*, pages 2498–2504, April 1996.
- [24] Dan J. Trudnowski, C.P. Baker, and M.S. Evans. Damping Control of a Large Flexible Manipulator Through Inertial Forces of a Small Manipulator. In *Proceedings of the American Control Conference*, pages 2878–2879, June 1993.
- [25] Z. Vafa and S. Dubowsky. The Kinematics and Dynamics of Space Manipulators: The Virtual Manipulator Approach. *The International Journal of Robotics Research*, 9(4):3–21, August 1990.
- [26] James Wright. Application of SPR Control to a Flexible Joint Manipulator. Master’s thesis, University of Victoria, 1996.

## Appendix A

# SARA Mechanical Design Drawings

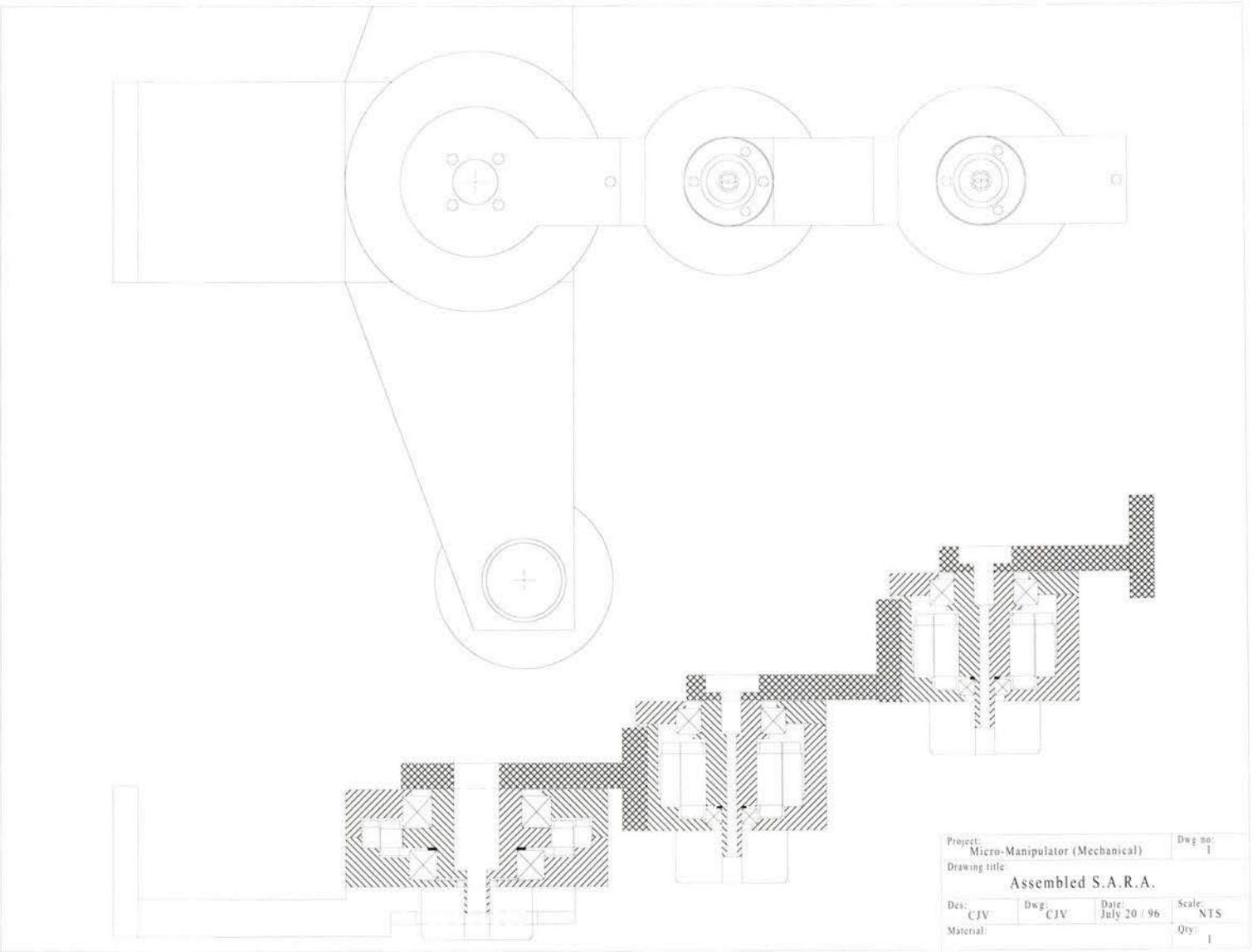


Figure A.1: Assembled Small Articulated Rigid Arm (SARA)

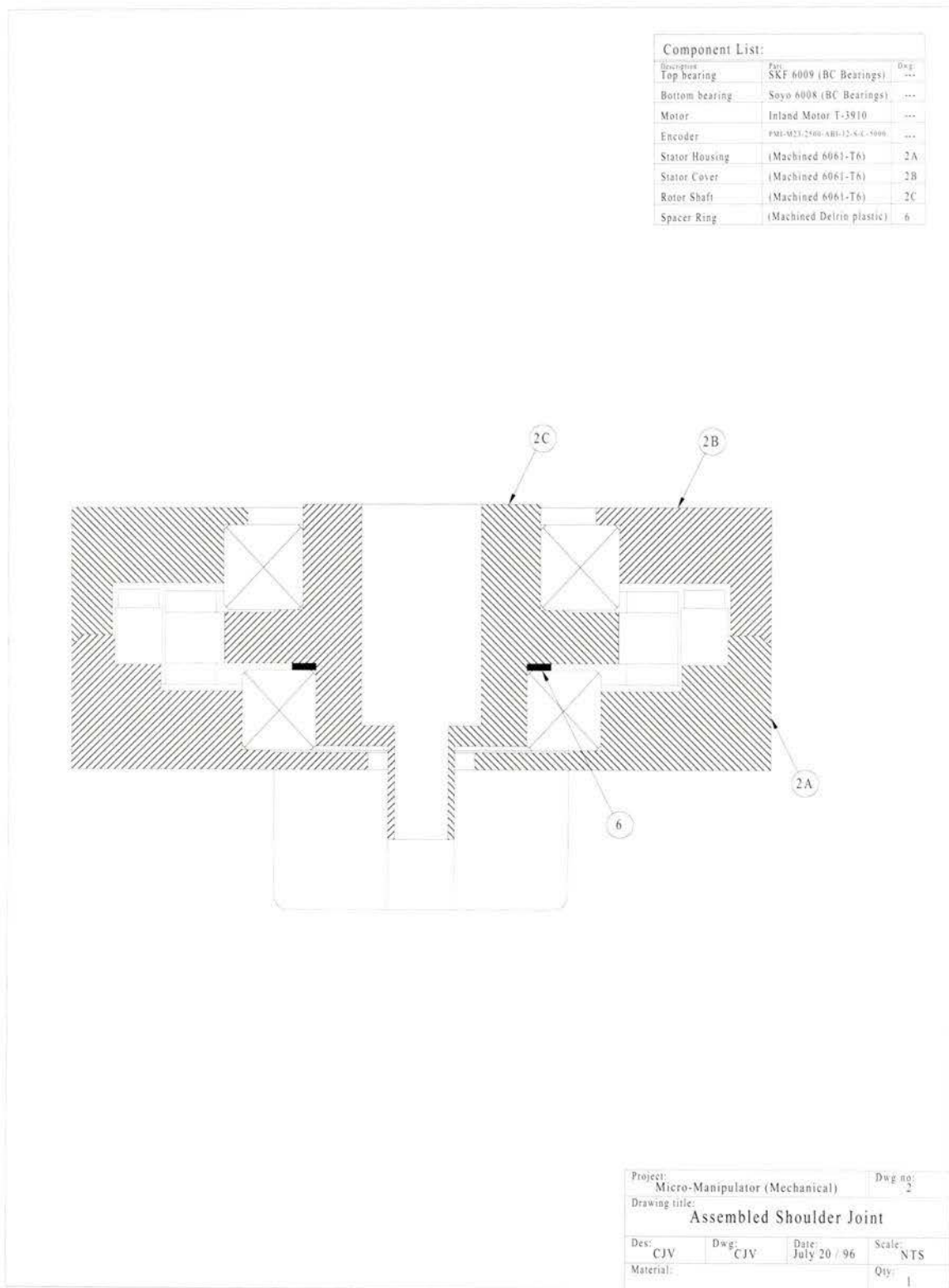


Figure A.2: Assembled SARA Shoulder Joint

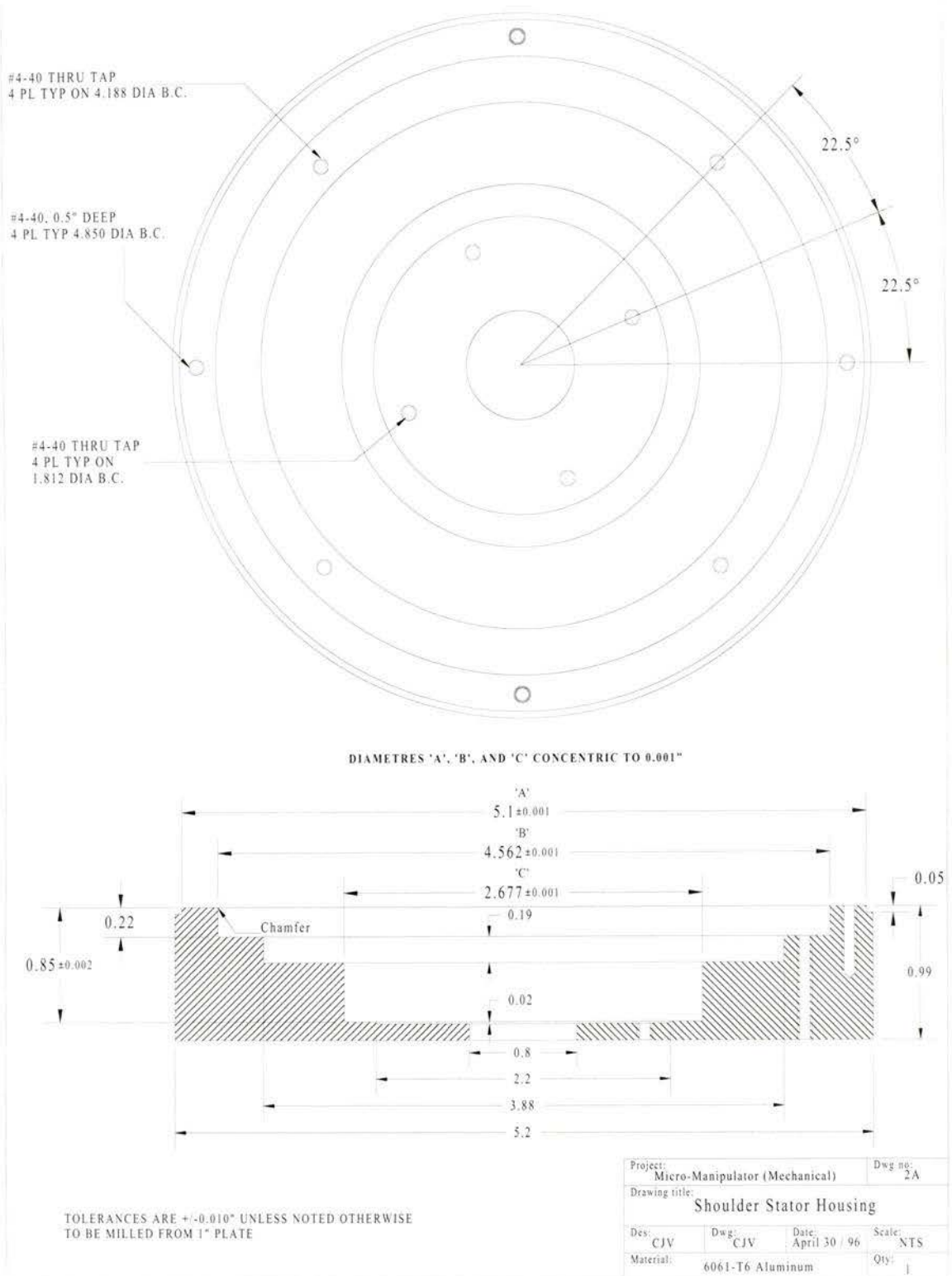


Figure A.3: SARA Shoulder Joint: Stator Housing

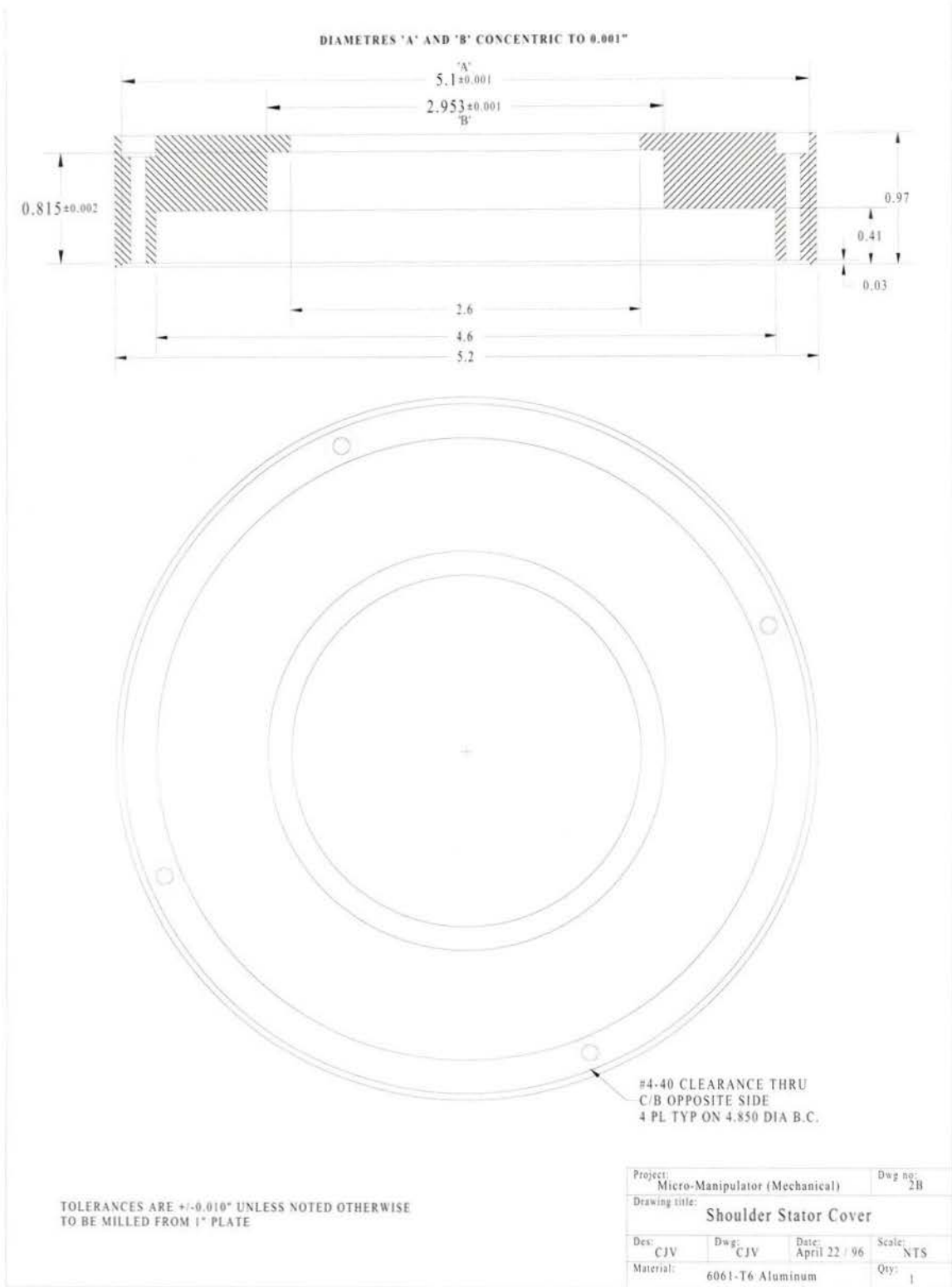


Figure A.4: SARA Shoulder Joint: Stator Housing Cover

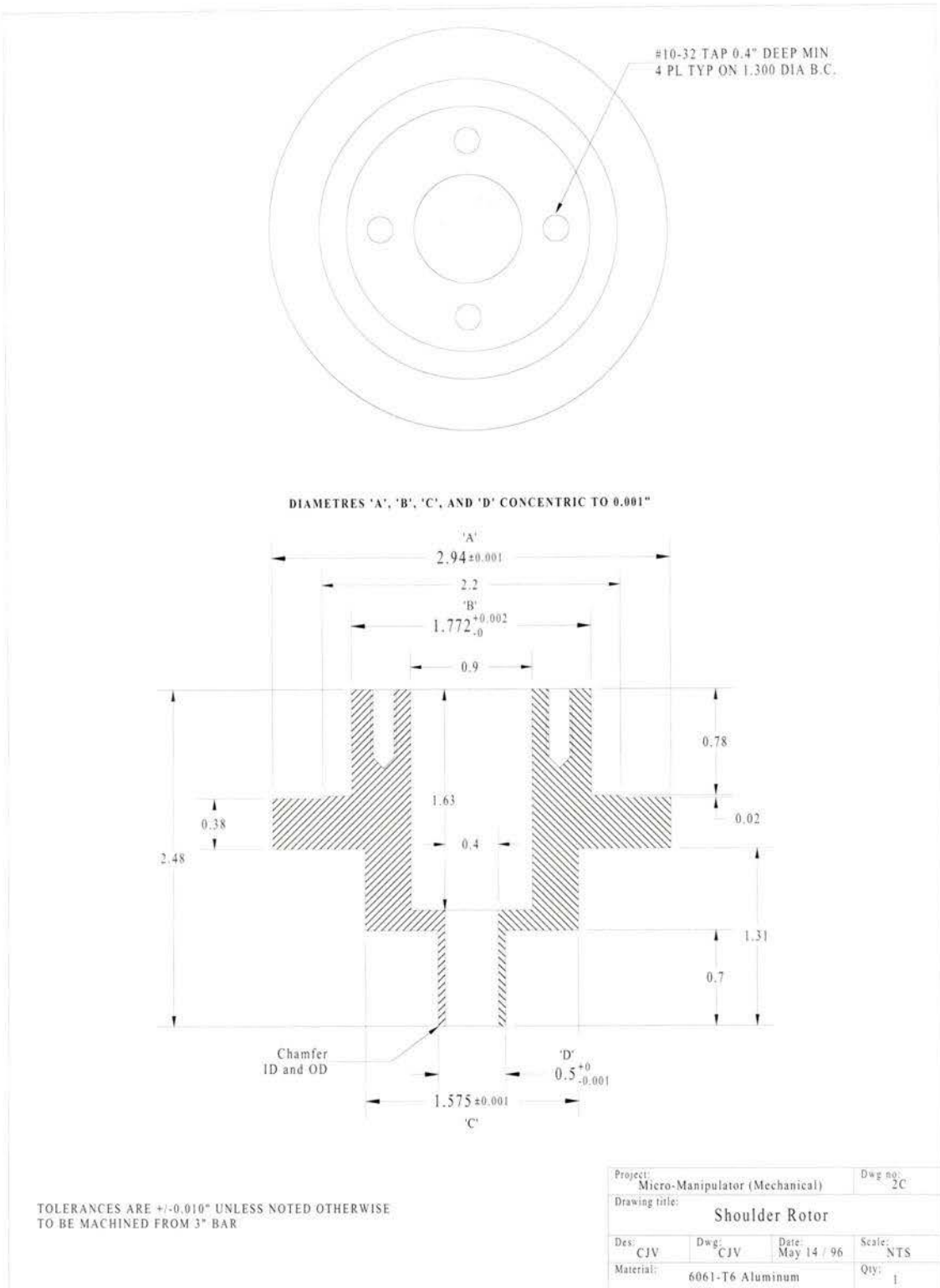
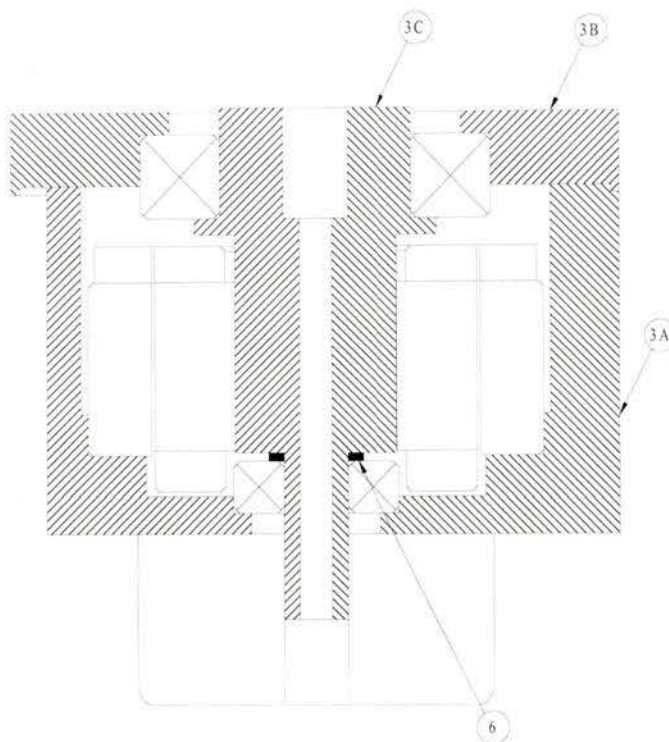


Figure A.5: SARA Shoulder Joint: Rotor Shaft

Component List:		
Descriptor	Part	Dwg.
Top bearing	SKF 6006 (BC Bearings)	...
Bottom bearing	SKF 6000 (BC Bearings)	....
Motor	Inland Motor T-2171	....
Encoder	PML-M23-2500-5B1-12-S-G-3437	....
Stator Housing	(Machined 6061-T6)	3A
Stator Cover	(Machined 6061-T6)	3B
Rotor Shaft	(Machined 6061-T6)	3C
Spacer Ring	(Machined Delrin plastic)	6



Project: Micro-Manipulator (Mechanical)		Dwg no: 3	
Drawing title: Assembled Elbow/Wrist Joint			
Des: CJV	Dwg: CJV	Date: July 20 / 96	Scale: NTS
Material:			Qty: 2

Figure A.6: Assembled SARA Elbow/Wrist Joint

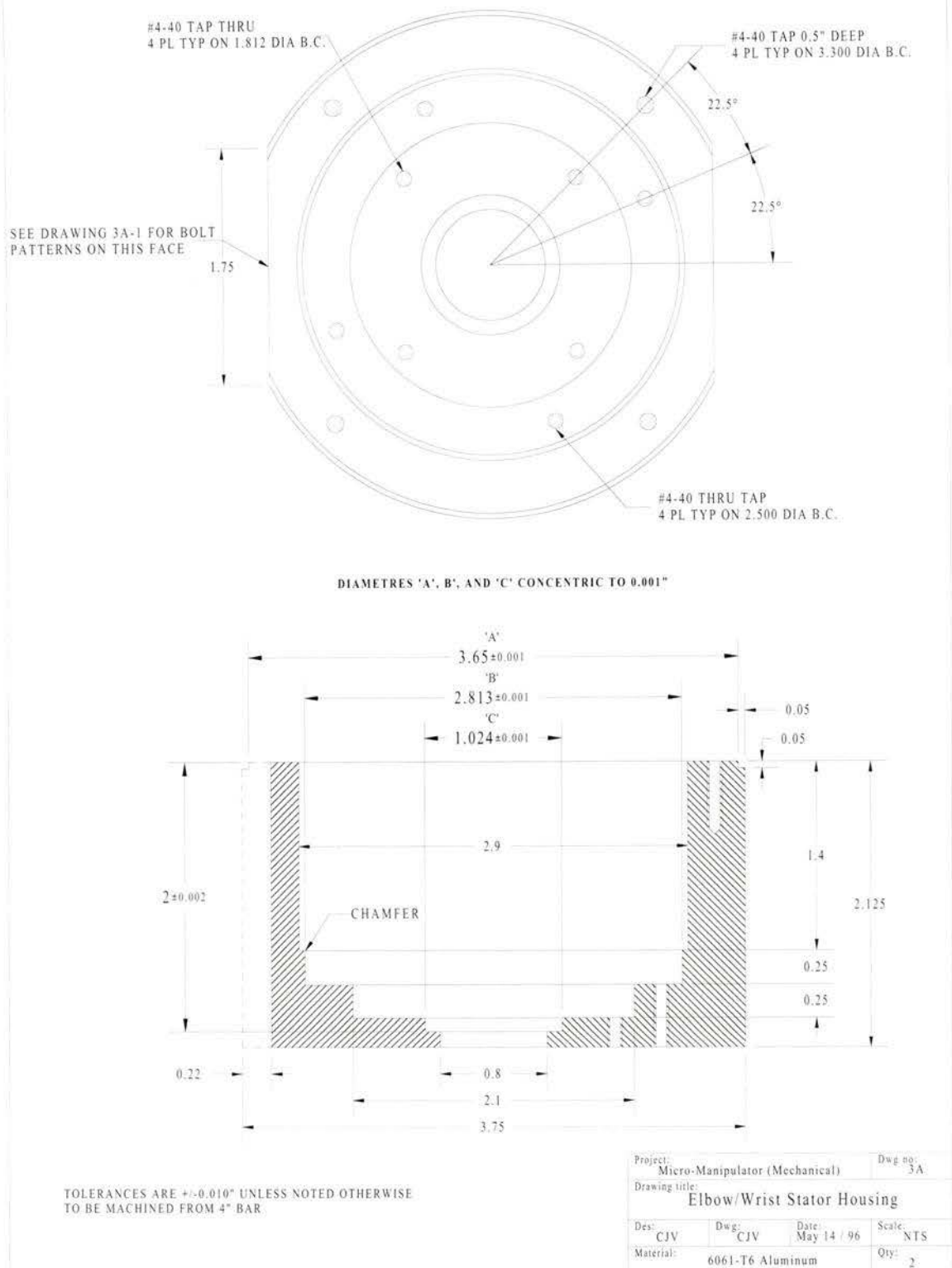
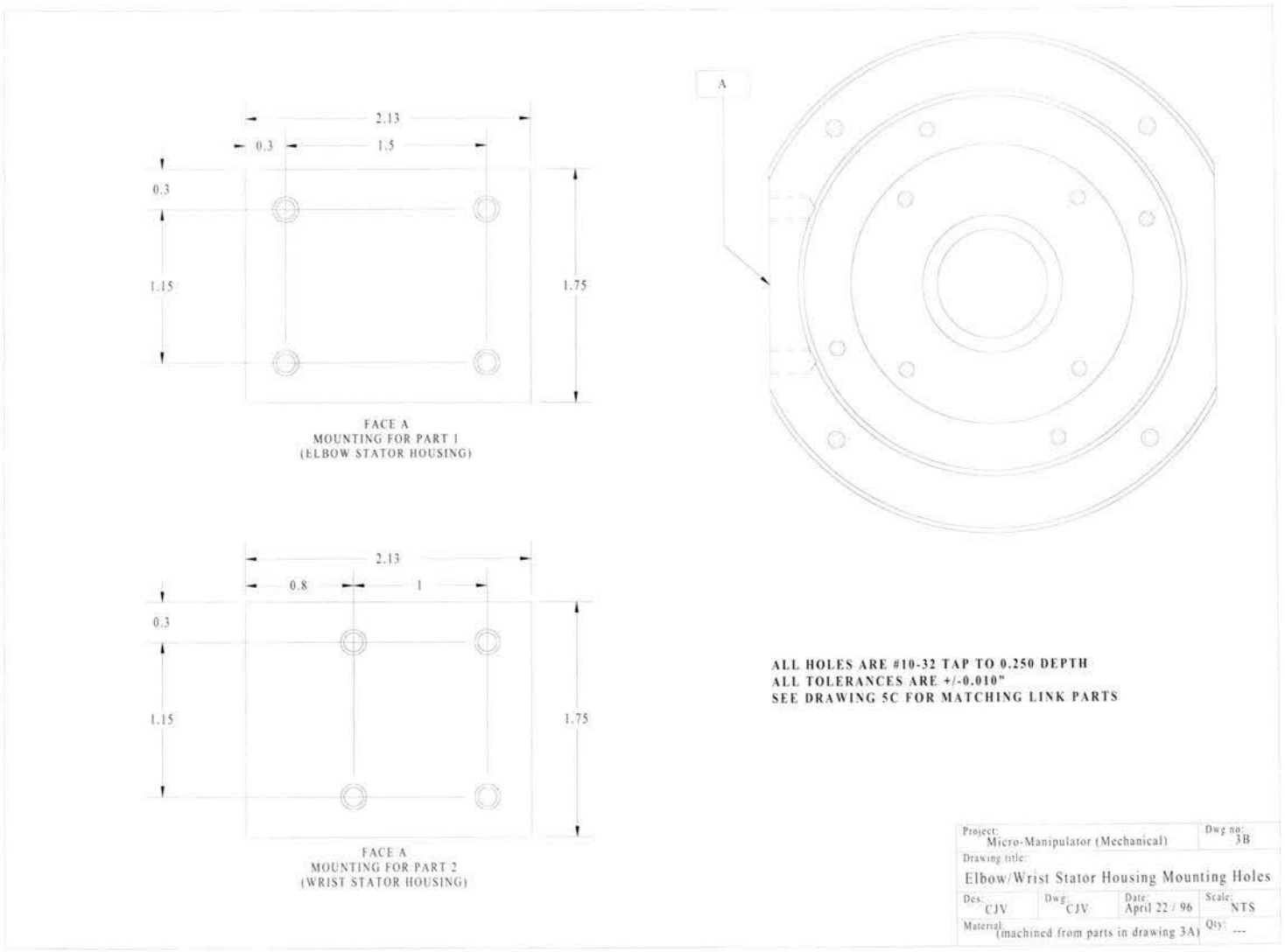


Figure A.7: SARA Elbow/Wrist Joint: Stator Housing

Figure A.8: SARA Elbow/Wrist Joint: Stator Housing Mounting Bolt Patterns



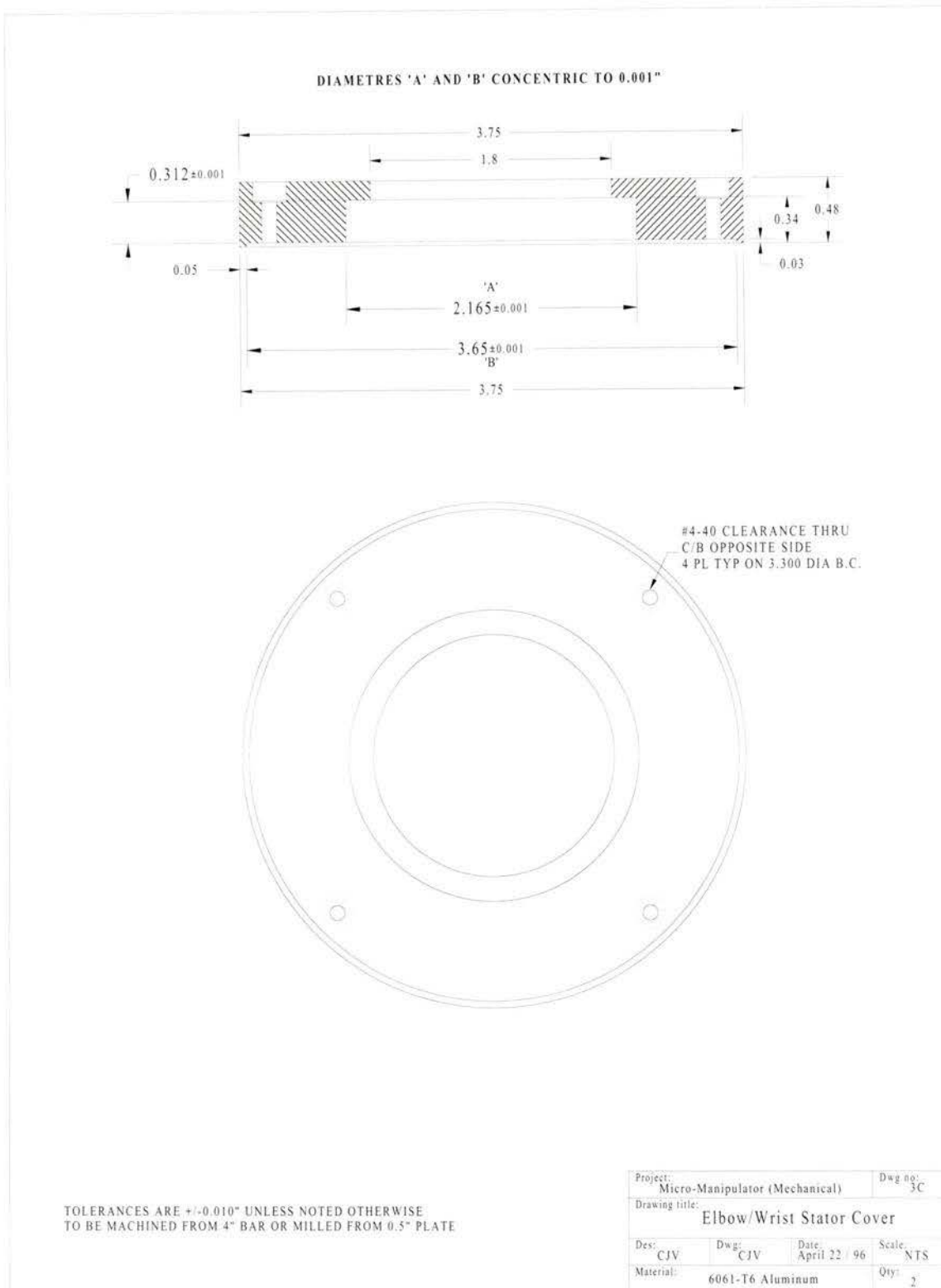


Figure A.9: SARA Elbow/Wrist Joint: Stator Housing Cover

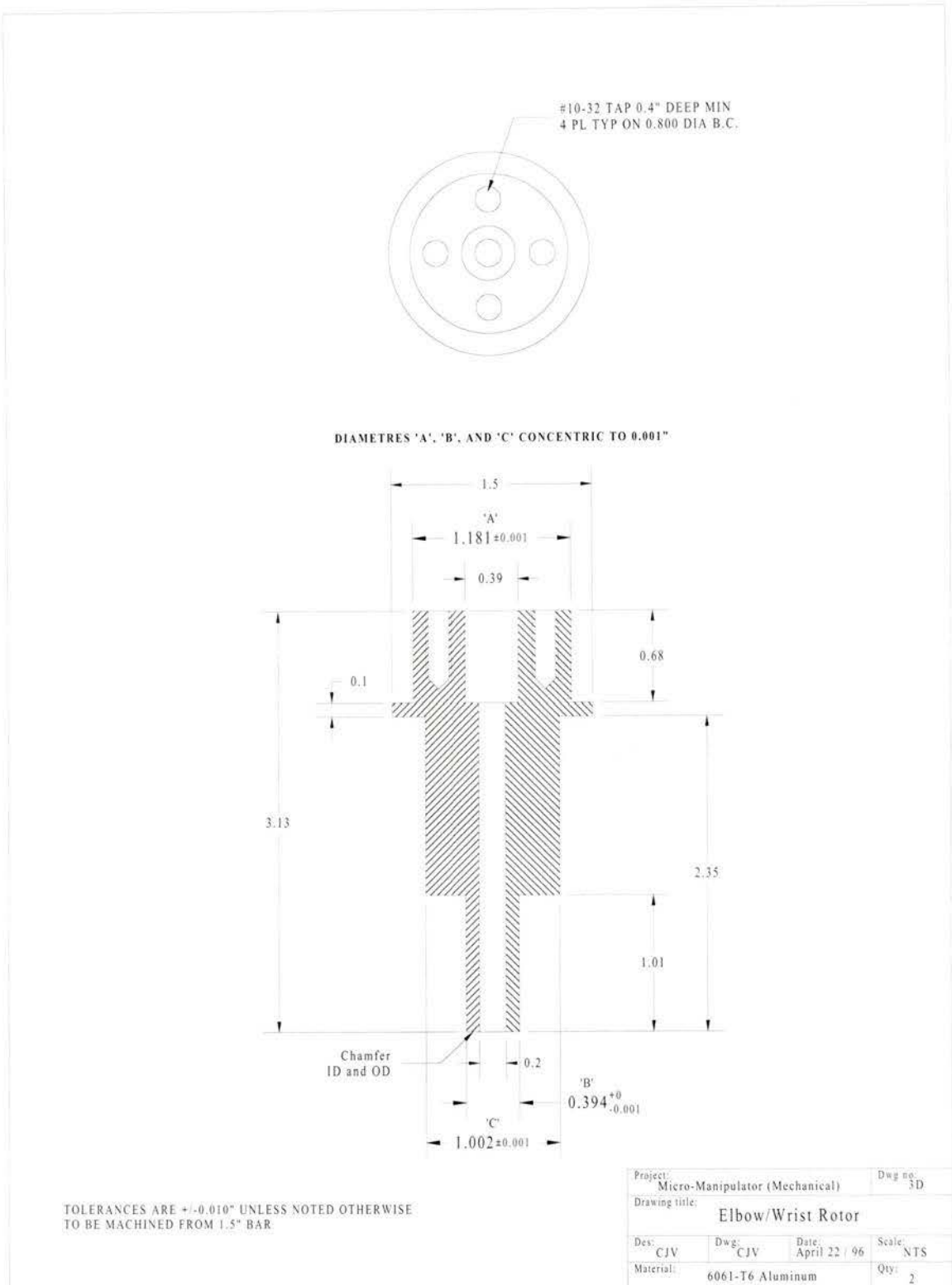


Figure A.10: SARA Elbow/Wrist Joint: Rotor Shaft

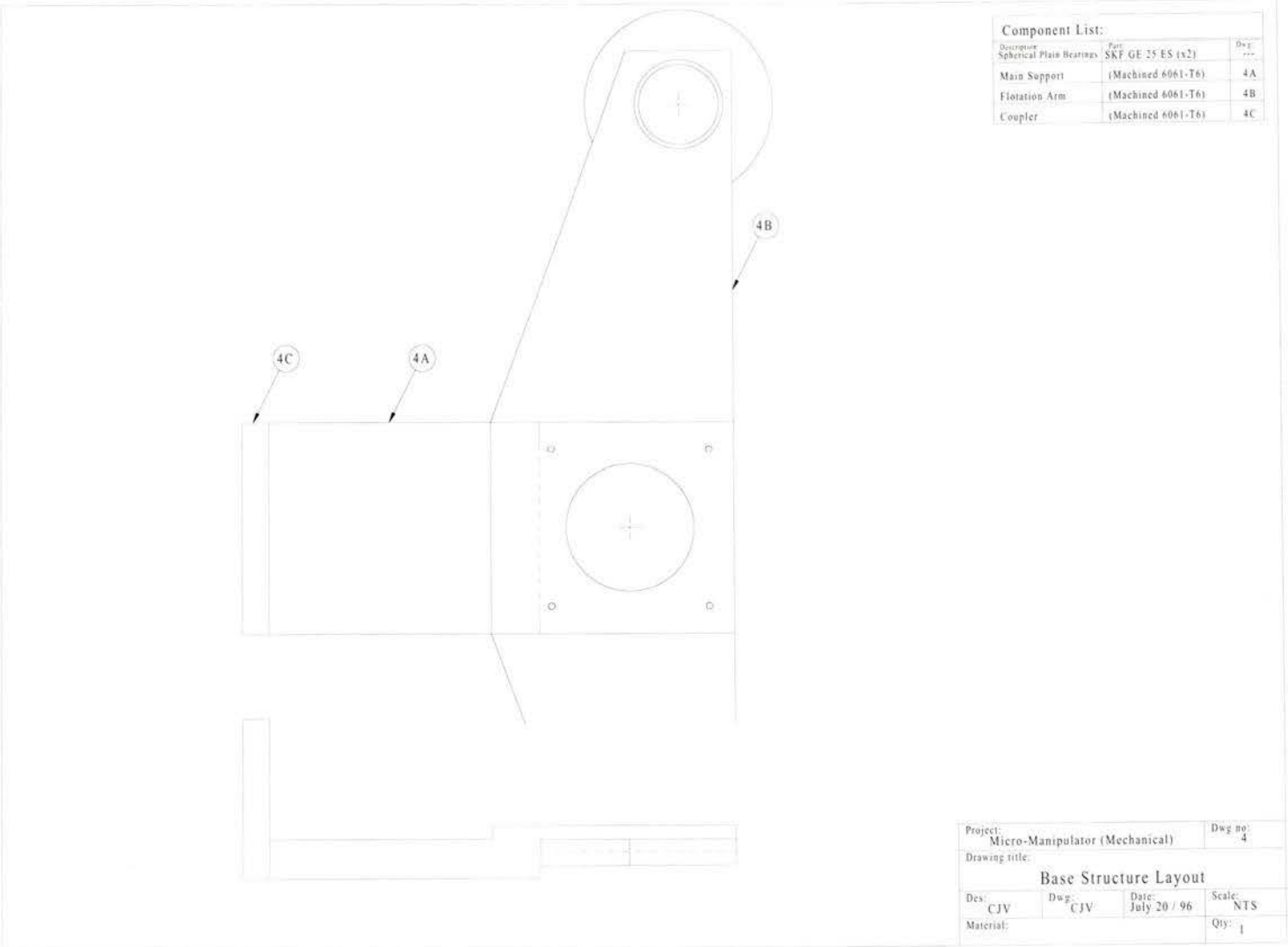
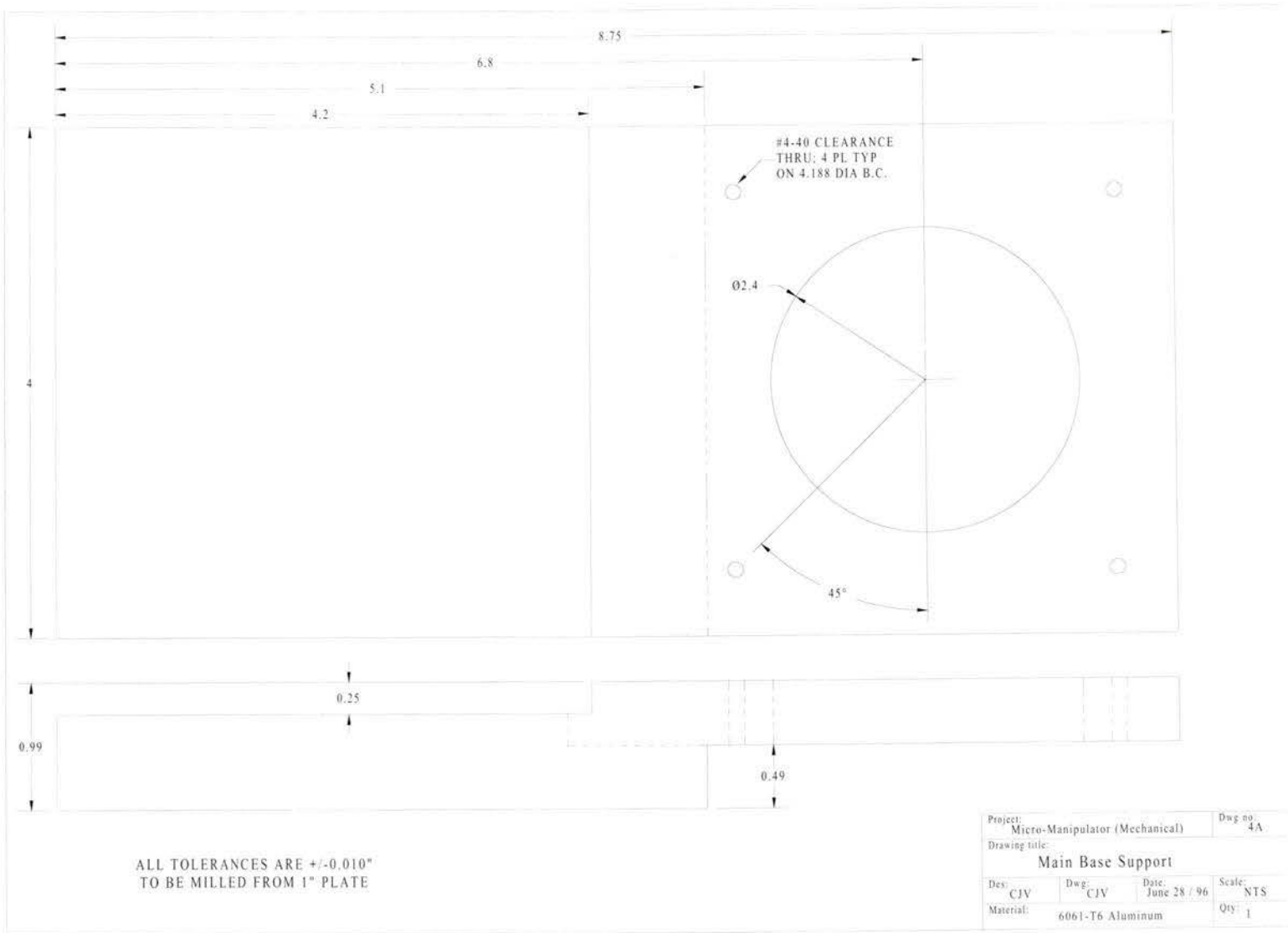


Figure A.11: Assembled SARA Base Assembly

Figure A.12: sARA Base Assembly: Main Base Support



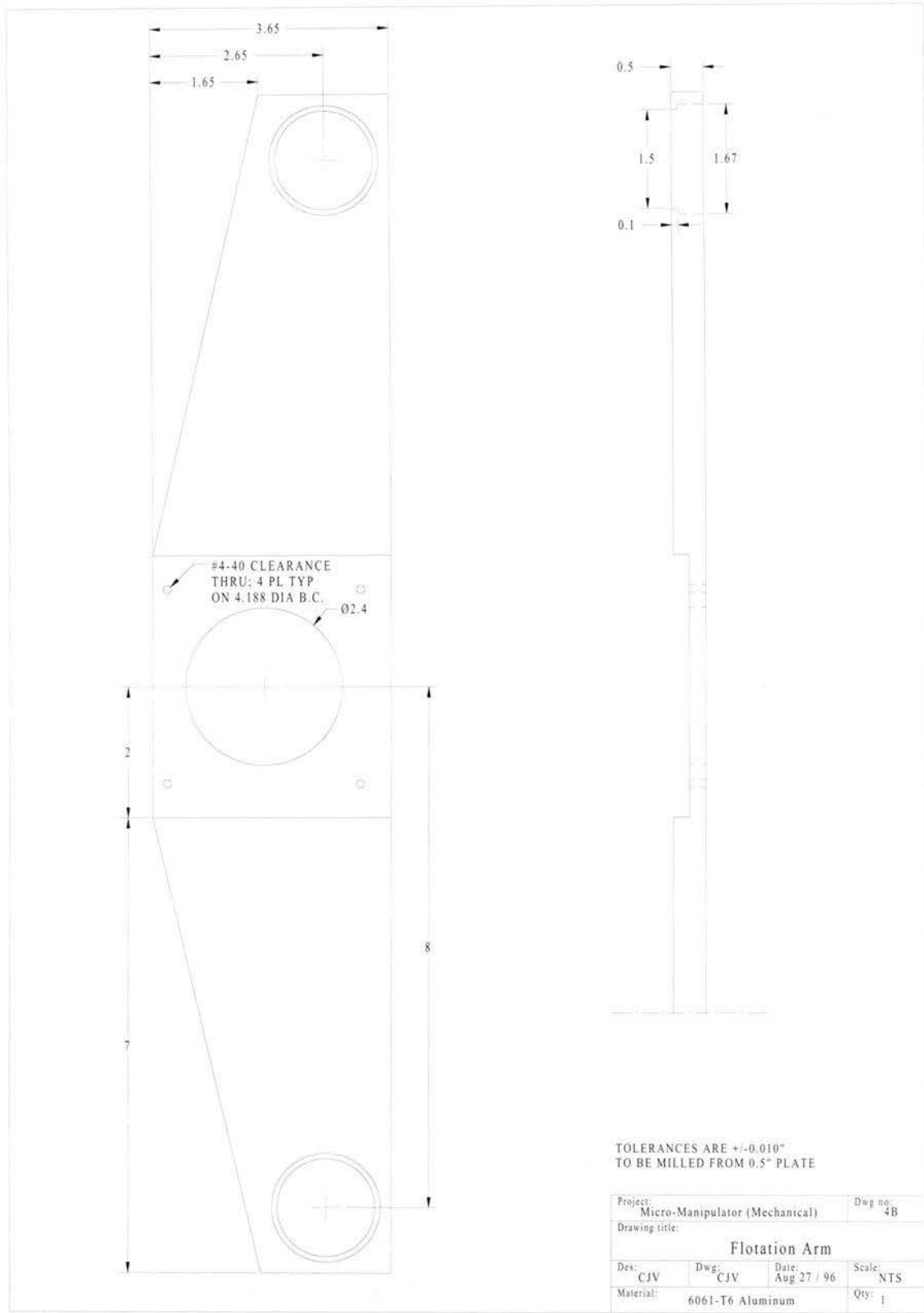


Figure A.13: SARA Base Assembly: Flotation Arm

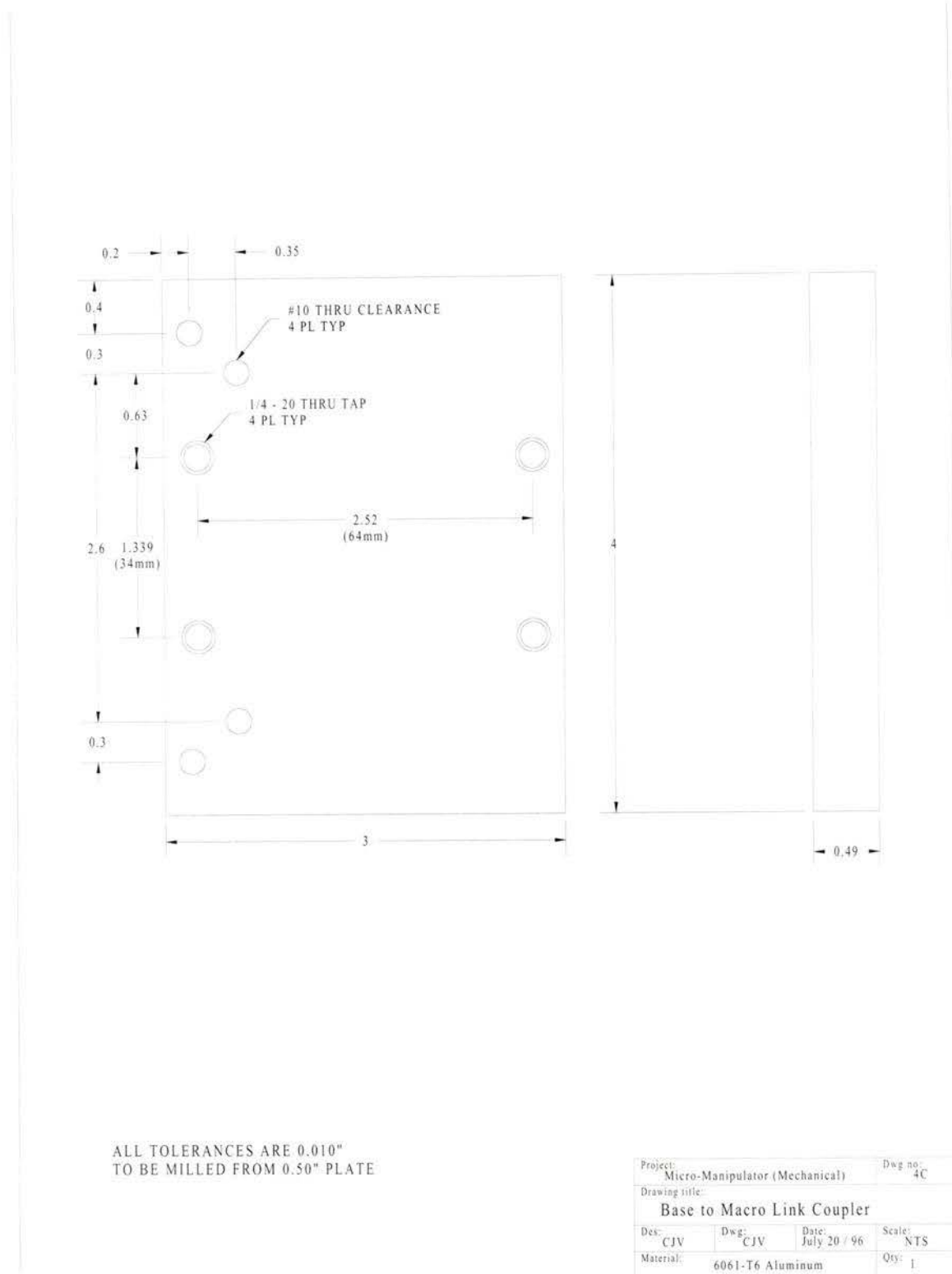


Figure A.14: SARA Base Assembly: Input Coupler

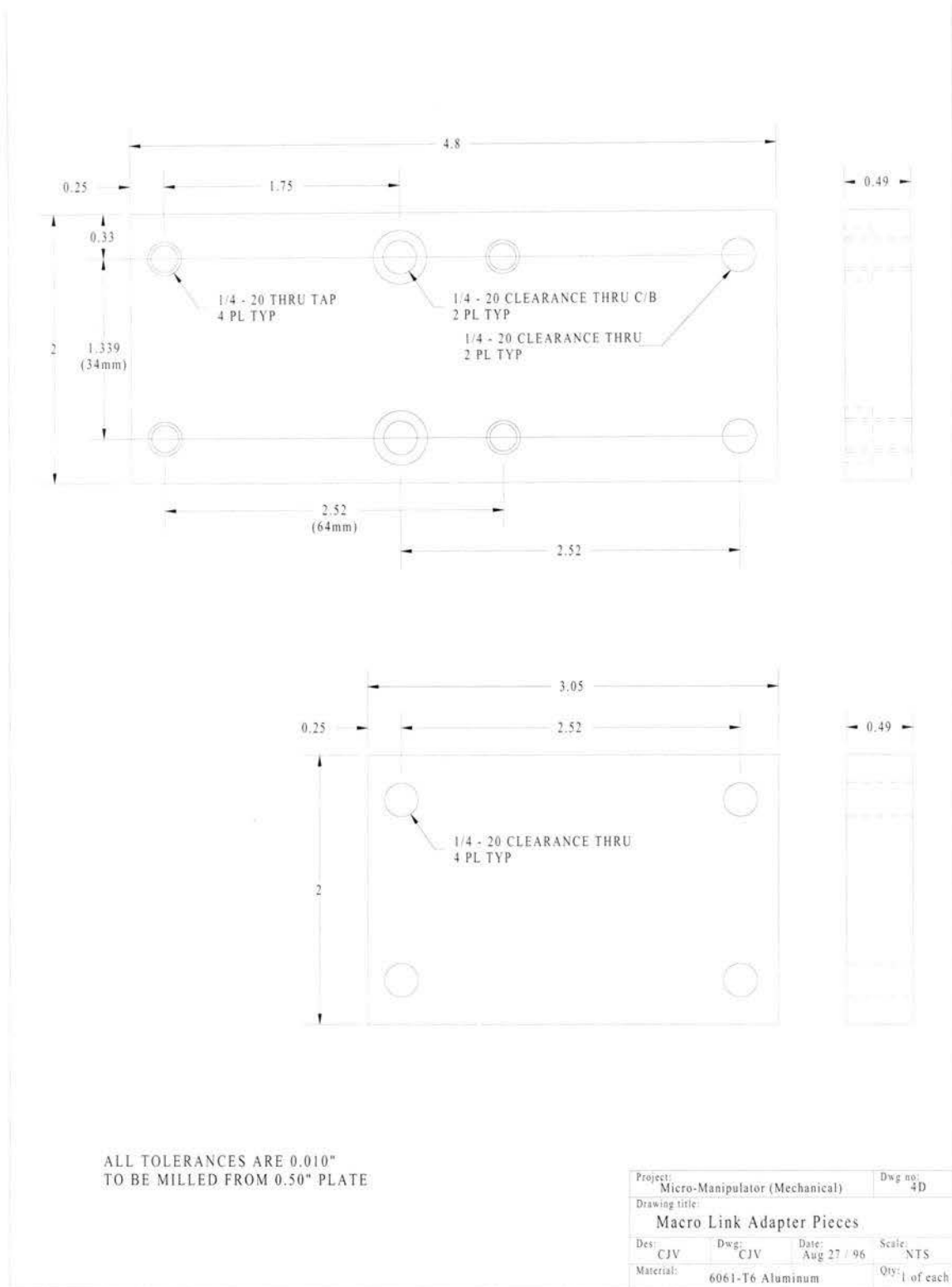


Figure A.15: SARA Base Assembly: Macro-Manipulator Link Adapter

Figure A.16: SARA Shoulder Output Link

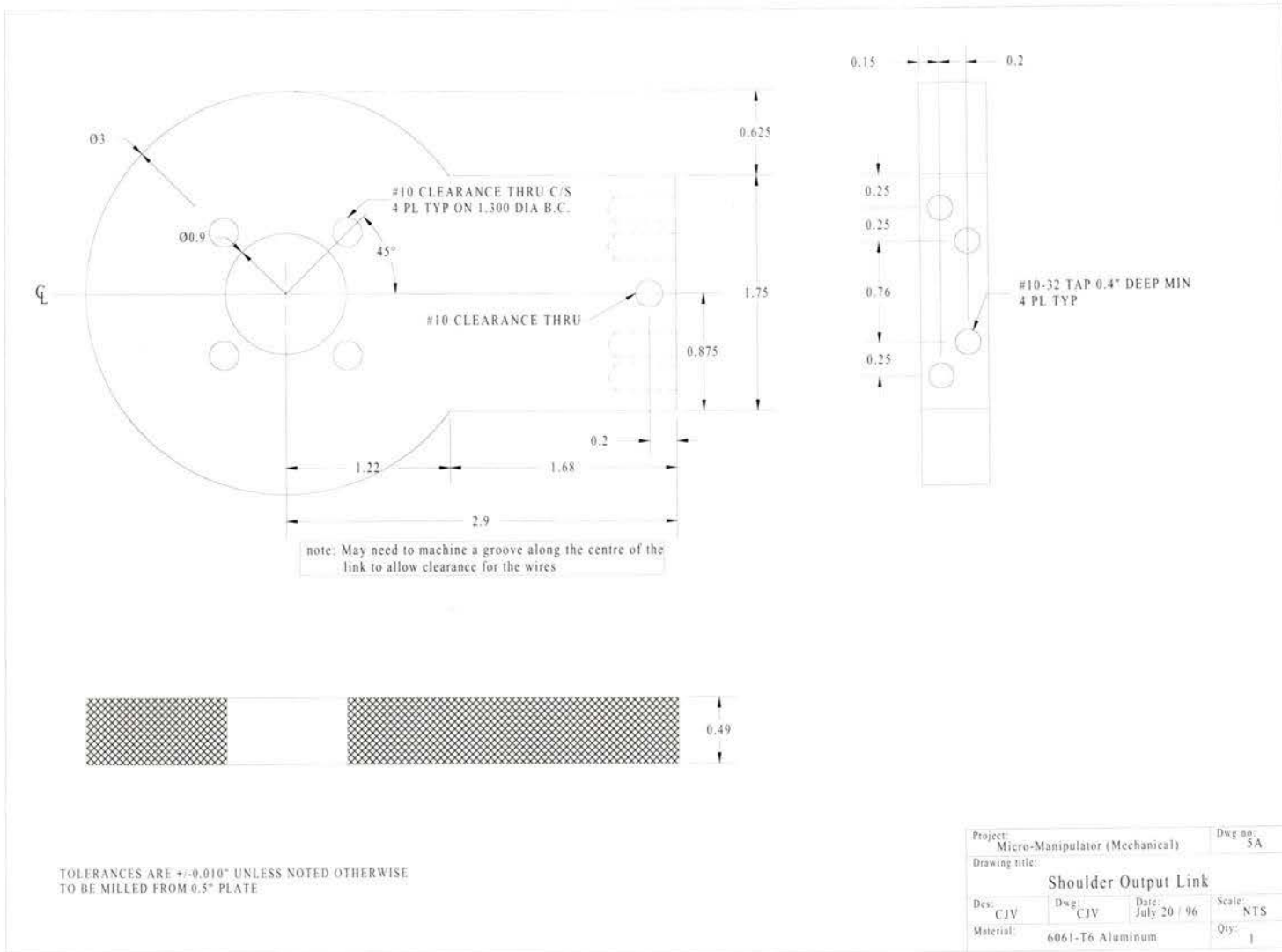
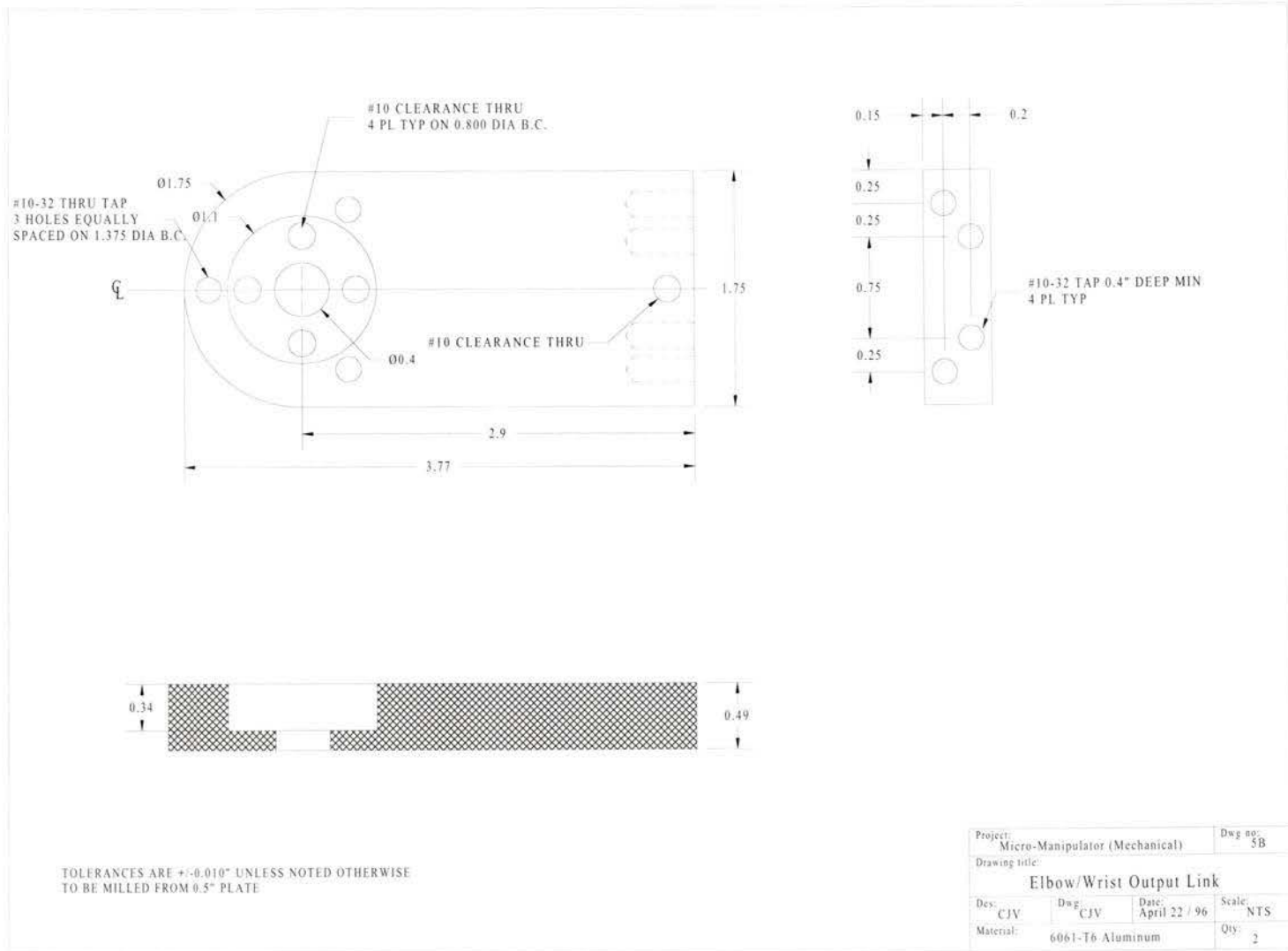
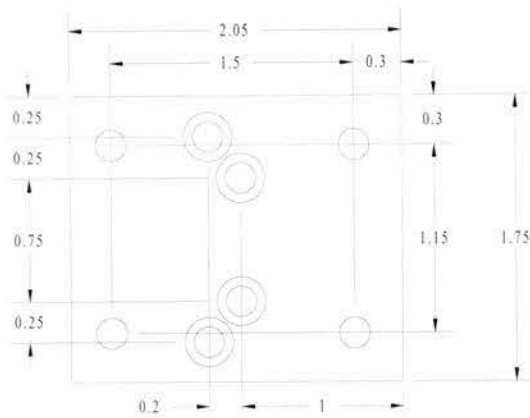




Figure A.17: SARA Elbow/Wrist Output Link

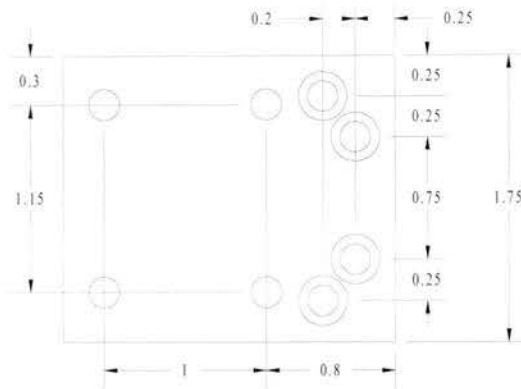




**BASE TO ELBOW COUPLER**



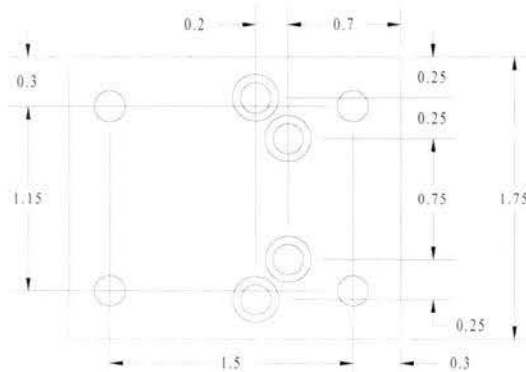
-  #10 CLEARANCE THRU C/B  
4 PL TYP
-  #10 CLEARANCE THRU  
4 PL TYP



**ELBOW TO WRIST COUPLER**



-  #10 CLEARANCE THRU C/B  
4 PL TYP
-  #10 CLEARANCE THRU  
4 PL TYP

**WRIST TO ACCESSORY COUPLER**



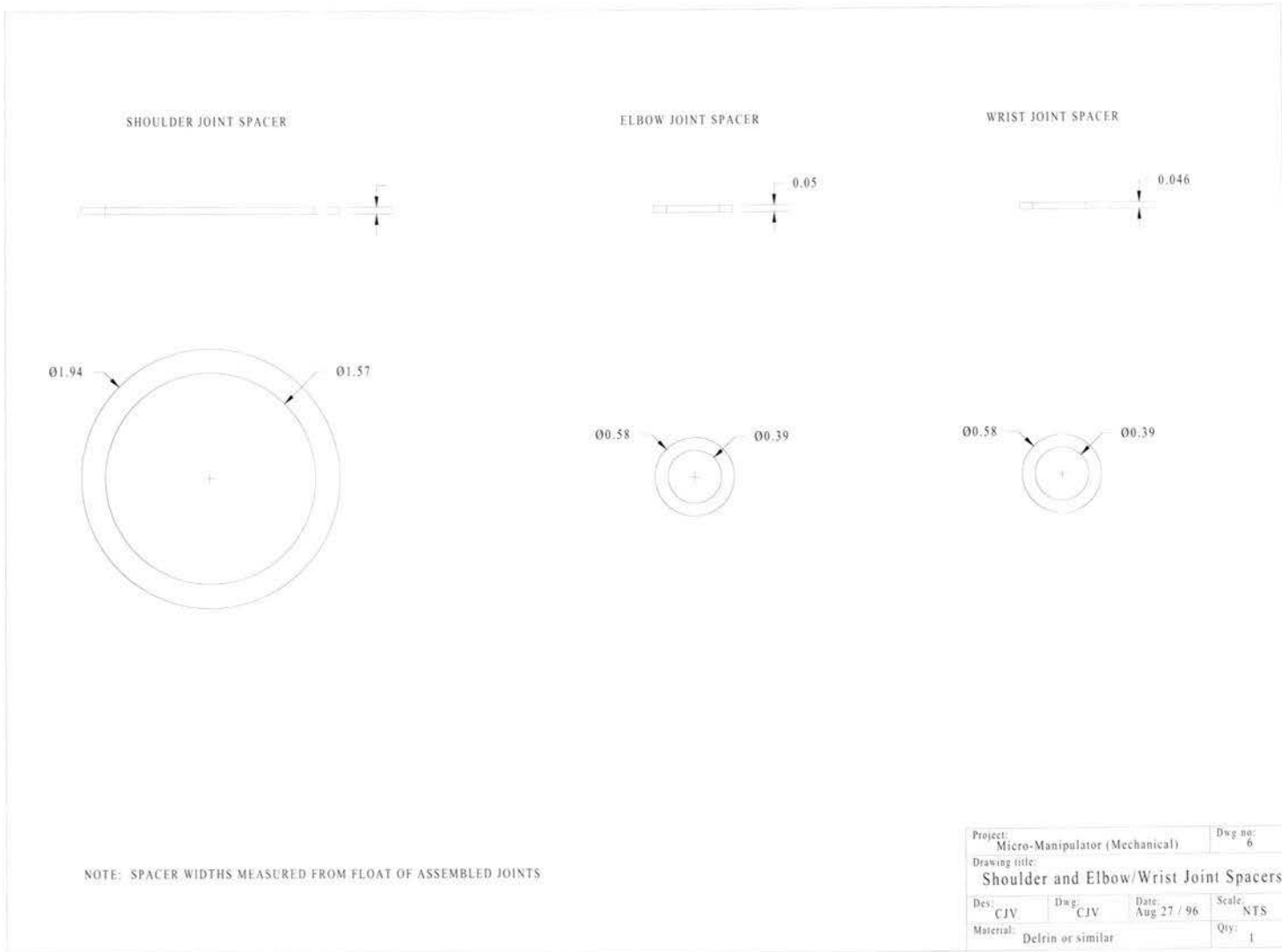
-  #10 CLEARANCE THRU C/B  
4 PL TYP
-  #10 CLEARANCE THRU  
4 PL TYP

TOLERANCES ARE +/-0.010" UNLESS NOTED OTHERWISE  
ALL PARTS ARE 2.05 x 1.75 x 0.50" PLATE

Project: Micro-Manipulator (Mechanical)		Dwg no: 5C	
Drawing title: <b>Joint Couplers</b>			
Des: CJV	Dwg: CJV	Date: July 20 / 96	Scale: NTS
Material: 6061-T6 Aluminum		Qty: 1 of each	

Figure A.18: SARA Link Couplers

Figure A.19: SARA Internal Joint Spacers



## Appendix B

# Optimal Gains for Mass-Spring-Damper Systems

### B.1 Introduction

An essential part of the derivation of P-PED is determining the optimal spring and damper gains,  $k_r$  and  $c_r$ , for a simple mass-spring-damper system. The complete manipulator for which P-PED gains need to be found is represented as a combination of these simple systems.

The optimum spring and damper gains are defined as those which “maximize the damping of the system dominant poles”<sup>1</sup>. Put another way, the objective is to maximize the damping of the least damped pole. If the two poles of the two-DOF mass-spring-damper system are unique, one of them will dominate the system response. It therefore stands to reason that the objective can be achieved by choosing gains such that the poles are identical. Ideally the poles will lie on the real axis (critical damping), but it will be shown that this is not always possible.

---

<sup>1</sup>Miguel A. Torres, Steven Dubowsky, and Attilio C. Pisoni. Vibration Control of Deployment Structures? Long-Reach Space Manipulators: The P-PED Method. In *Proc. IEEE International Conference on Robotics and Automation*, pages 2498-2504, April 1996

## B.2 System Definition

In state-space form, the unforced dynamics of the mass-spring-dampers are represented by the homogeneous differential equation

$$\dot{\mathbf{x}} = \mathbf{A}\mathbf{x}, \quad (\text{B.1})$$

where  $\mathbf{x} = [y_b, y_r, \dot{y}_b, \dot{y}_r]^T$  and  $\mathbf{A}$  is the system matrix given by

$$\mathbf{A} = \begin{bmatrix} 0 & 0 & 1 & 0 \\ 0 & 0 & 0 & 1 \\ -\frac{k_b}{m_b} & -\frac{k_r}{m_b} & 0 & -\frac{c_r}{m_b} \\ \frac{k_b}{m_b} & -\left(\frac{k_r}{m_b} + \frac{k_r}{m_r}\right) & 0 & \left(\frac{c_r}{m_b} + \frac{c_r}{m_r}\right) \end{bmatrix} \quad (\text{B.2})$$

It is noted that  $y_r$  is the relative displacement of  $m_r$  with respect to  $m_b$ .

The pole locations are defined by the characteristic equation,  $|\mathbf{A} - s\mathbf{I}| = 0$ . After expanding the determinant, the characteristic equation is:

$$s^4 + c_r \left( \frac{1}{m_b} + \frac{1}{m_r} \right) s^3 + \left[ \left( \frac{k_r}{m_b} + \frac{k_r}{m_r} \right) + \frac{k_b}{m_b} \right] s^2 + \left( \frac{k_b c_r}{m_b m_r} \right) s + \left( \frac{k_b k_r}{m_b m_r} \right) = 0 \quad (\text{B.3})$$

## B.3 Optimum Gains

It was stated in the introduction that the optimum gains,  $k_r$  and  $c_r$ , will result in repeated poles. The characteristic equation will therefore have the form  $(s - \sigma_1)^2(s - \sigma_2)^2 = 0$ , which expands to

$$s^4 - 2(\sigma_1 + \sigma_2)s^3 + (\sigma_1^2 + 4\sigma_1\sigma_2 + \sigma_2^2)s^2 - 2(\sigma_1\sigma_2^2 + \sigma_1^2\sigma_2)s + (\sigma_1\sigma_2)^2 = 0, \quad (\text{B.4})$$

where  $\sigma_1$  and  $\sigma_2$  are the repeated pole locations. If the system is under-damped or critically damped,  $\sigma_2$  is the complex conjugate of  $\sigma_1$ . For an over-damped system, both  $\sigma_1$  and  $\sigma_2$

lie on the real axis.

Four equations in the four unknowns  $\sigma_1$ ,  $\sigma_2$ ,  $k_r$ , and  $c_r$  are obtained by equating the polynomial coefficients in equations (B.3) and (B.4). Additional constraint that the real parts of  $\sigma_1$  and  $\sigma_2$  be negative are also required to guarantee a unique, stable solution. After some algebraic manipulation, the resulting pole locations are:

$$\sigma_1 = -\sqrt{\frac{2k_b m_b}{(m_b + m_r) \left[ m_r + \sqrt{m_r(m_r - 4m_b)} - 2m_b \right]}} \quad (\text{B.5})$$

$$\sigma_2 = -\sqrt{\frac{k_b}{2m_b(m_b + m_r)} \left[ m_r + \sqrt{m_r(m_r - 4m_b)} - 2m_b \right]} \quad (\text{B.6})$$

It is interesting to note that both mass-spring-damper modes are critically damped when  $m_r = 4m_b$ . When  $m_r < 4m_b$ , the modes are under-damped, and when  $m_r > 4m_b$ , the modes are over-damped.

Equations (B.5) and (B.6) are now used to solve for the optimal spring and damper gains:

$$k_r = \left( \frac{m_b m_r}{m_b + m_r} \right) \sigma_1 \sigma_2 \quad (\text{B.7})$$

$$c_r = -2 \left( \frac{m_b m_r}{m_b + m_r} \right) (\sigma_1 + \sigma_2) \quad (\text{B.8})$$

The gains calculated with equations (B.7) and (B.8) are identical to those found with the original iterative root-locus procedure defined by Torres.

## Appendix C

# Guyan Reduction

The simplified models on which the Coupling Map and Pseudo-Passive Energy Dissipation (P-PED) are based do not match the physical realities of some of the manipulators investigated in this work. Guyan reduction<sup>1</sup> was used as a standard method of reducing the dynamics equations of these manipulators into the framework of the simplified models. The Guyan reduction equations are developed in this appendix, and some results for the LAURA-SARA manipulator are given.

### C.1 Theoretical Development

#### C.1.1 Statics

In the static analysis of a structure or mechanism, considerable computational effort can be saved by considering only degrees of freedom on which external forces act. Consider an arbitrary structure with statics defined by

$$\mathbf{f} = \mathbf{K}\mathbf{x}, \tag{C.1}$$

---

<sup>1</sup>Robert J. Guyan. Reduction of Stiffness and Mass Matrices. *AIAA Journal* 3(2):380, 1964.

where  $\mathbf{f} = [\mathbf{f}_a^T, \mathbf{f}_b^T]^T$ ,  $\mathbf{x} = [\mathbf{x}_a^T, \mathbf{x}_b^T]^T$ , and

$$\mathbf{K} = \begin{bmatrix} \mathbf{K}_{aa} & \mathbf{K}_{ab} \\ \mathbf{K}_{ab}^T & \mathbf{K}_{bb} \end{bmatrix}. \quad (\text{C.2})$$

The coordinates are partitioned such that those with subscript  $a$  are not subjected to any external forces, that is  $\mathbf{f}_a = \mathbf{0}$ . The forces  $\mathbf{f}_b$  can thus be solved for as functions only of the deflections  $\mathbf{x}_b$ :

$$\mathbf{f}_b = \mathbf{K}_b \mathbf{x}_b \quad (\text{C.3})$$

where

$$\mathbf{K}_b = \mathbf{K}_{bb} - \mathbf{K}_{ab}^T \mathbf{K}_{aa}^{-1} \mathbf{K}_{ab} \quad (\text{C.4})$$

is the reduced stiffness matrix. No approximations or simplifying assumptions were required, so that the results of equation (C.3) exactly match those of equation (C.1).

### C.1.2 Dynamics

For a dynamic analysis, the mass matrix must be simultaneously reduced. Consider equation (C.1) with  $\mathbf{f}_a = \mathbf{0}$ . The deflections of the free degrees of freedom,  $\mathbf{x}_a$ , can be found as function of the forced degrees of freedom,  $\mathbf{x}_b$ :

$$\mathbf{x}_a = (-\mathbf{K}_{aa}^{-1} \mathbf{K}_{ab}) \mathbf{x}_b \quad (\text{C.5})$$

Equation (C.5) yields a coordinate transformation between the complete system coordinates,  $\mathbf{x}$ , and the reduced system coordinates,  $\mathbf{x}_b$ , for the static case:

$$\mathbf{x} = \mathbf{T}_G \mathbf{x}_b, \quad (\text{C.6})$$

where

$$\mathbf{T}_G = \begin{bmatrix} -\mathbf{K}_{aa}^{-1} \mathbf{K}_{ab} \\ \mathbf{I} \end{bmatrix} \quad (\text{C.7})$$

is the Guyan transformation matrix.

Potential and kinetic energy considerations are now used to derive the reduced matrices.

In the following,  $\mathbf{M}$  is the complete mass matrix:

$$\begin{aligned} \text{kinetic energy:} \quad T &= \frac{1}{2} \dot{\mathbf{x}}^T \mathbf{M} \dot{\mathbf{x}} \\ &= \frac{1}{2} \dot{\mathbf{x}}_b^T (\mathbf{T}_G^T \mathbf{M} \mathbf{T}_G) \dot{\mathbf{x}}_b \\ &= \frac{1}{2} \dot{\mathbf{x}}_b^T (\mathbf{M}_b) \dot{\mathbf{x}}_b \\ \text{potential energy:} \quad U &= \frac{1}{2} \mathbf{x}^T \mathbf{K} \mathbf{x} \\ &= \frac{1}{2} \mathbf{x}_b^T (\mathbf{T}_G^T \mathbf{K} \mathbf{T}_G) \mathbf{x}_b \\ &= \frac{1}{2} \mathbf{x}_b^T (\mathbf{K}_b) \mathbf{x}_b \end{aligned} \quad (\text{C.8})$$

where  $\mathbf{M}_b = \mathbf{T}_G^T \mathbf{M} \mathbf{T}_G$  is the Guyan reduced mass matrix, and  $\mathbf{K}_b = \mathbf{T}_G^T \mathbf{K} \mathbf{T}_G$  is the Guyan reduced stiffness matrix. After multiplication,  $\mathbf{M}_b$  and  $\mathbf{K}_b$  are written as:

$$\mathbf{M}_b = \mathbf{M}_{bb} - \mathbf{M}_{ab}^T \mathbf{K}_{aa}^{-1} \mathbf{K}_{ab} - (\mathbf{K}_{aa}^{-1} \mathbf{K}_{ab})^T (\mathbf{M}_{ab} - \mathbf{M}_{aa} \mathbf{K}_{aa}^{-1} \mathbf{K}_{ab}) \quad (\text{C.9})$$

$$\mathbf{K}_b = \mathbf{K}_{bb} - \mathbf{K}_{ab}^T \mathbf{K}_{aa}^{-1} \mathbf{K}_{ab} \quad (\text{C.10})$$

It is noted that the above equation for  $\mathbf{K}_b$  is identical to equation (C.4), which was derived from statics alone.

## C.2 LAURA-SARA Results

The first and second modal frequencies of the LAURA-SARA manipulator for the exact and Guyan reduced systems are investigated here. The frequencies are calculated with SARA locked at many different configurations defined by the angles of the SARA shoulder and elbow joints,  $\theta_{S1}$  and  $\theta_{S2}$ . These results are applicable to the Coupling Map calculations.

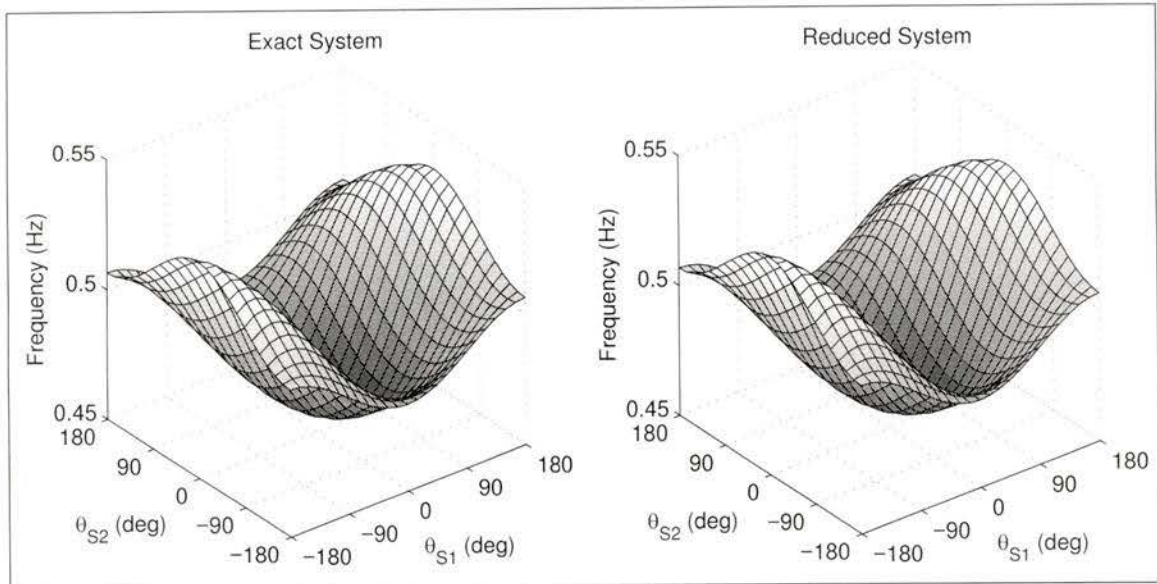


Figure C.1: *First Modal Frequencies for Exact and Reduced Systems with  $\theta_{L2} = 0^\circ$*

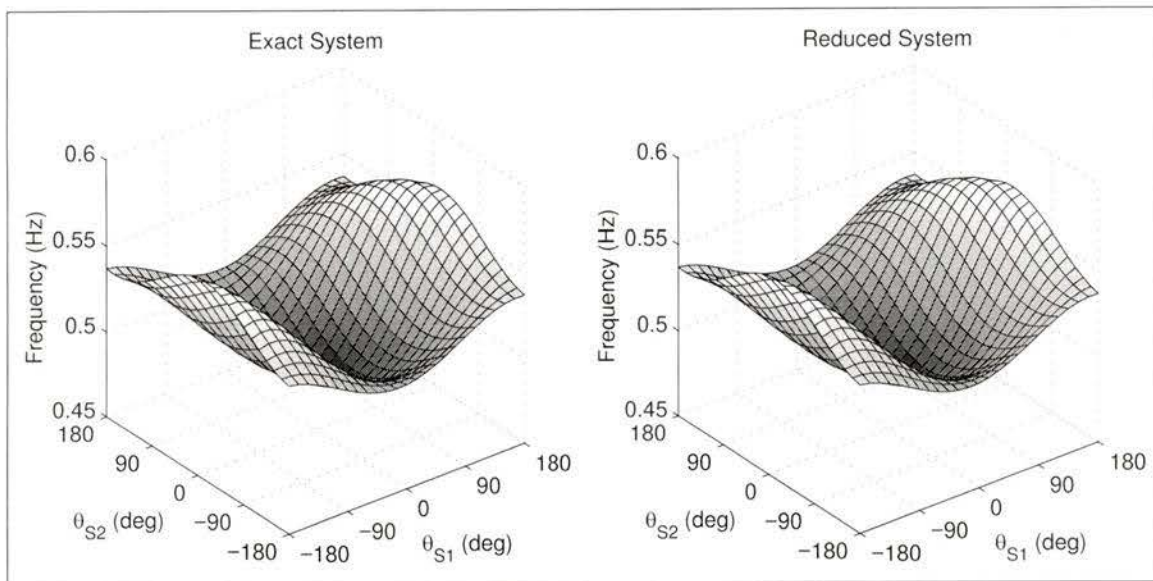


Figure C.2: *First Modal Frequencies for Exact and Reduced Systems with  $\theta_{L2} = 45^\circ$*

For P-PED, only the micro-manipulator base is included in the Guyan reduction procedure.

### C.2.1 First Modal Frequency

The plots in Figure C.1 show the first modal frequency for the LAURA-SARA manipulator using the exact and reduced dynamics with LAURA2 at  $0^\circ$ . The frequencies are nearly identical, although the reduced system frequencies slightly over-estimate the exact frequencies.

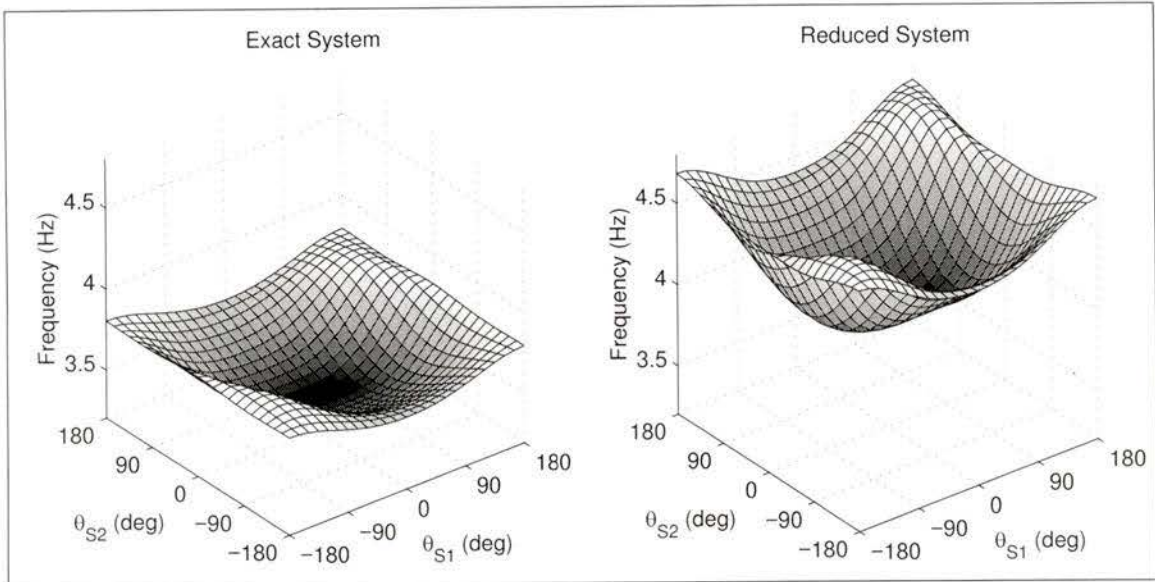


Figure C.3: *Second Modal Frequencies for Exact and Reduced Systems with  $\theta_{L2} = 0^\circ$*

The maximum fractional error is only 0.04%.

The results with LAURA2 at  $45^\circ$ , which are plotted in Figure C.2, are very similar. Again the reduced system frequencies over-estimate the exact frequencies by a tiny amount. The maximum error is 0.02%.

### C.2.2 Second Modal Frequency

Figures C.3 and C.4 show the second modal frequencies for the exact and reduced systems with  $\theta_{L2} = 0^\circ$  and  $\theta_{L2} = 45^\circ$  respectively. The maximum error in the latter is only 0.16%, but in the former the errors are consistently quite large – between 14% and 23%.

Investigation has shown that Guyan reduction breaks down for the second mode in the vicinity of  $\theta_{L2} = 0^\circ$ , where LAURA is axially rigid. This is demonstrated in Figure C.5 which shows a plot of the second modal frequency calculated over a range of  $\theta_{L2}$  angles, all with  $\theta_{S1} = \theta_{S2} = 0^\circ$ . It is noted that the error is very large near  $\theta_{L2} = 0^\circ$ , but rapidly drops as  $|\theta_{L2}|$  increases.

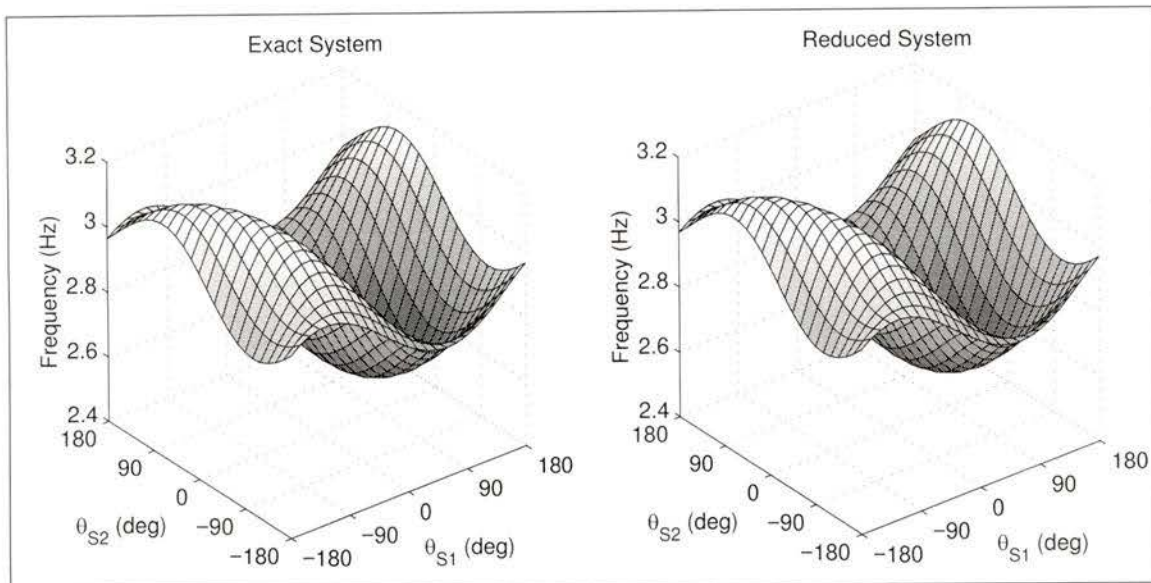


Figure C.4: Second Modal Frequencies for Exact and Reduced Systems with  $\theta_{L2} = 45^\circ$

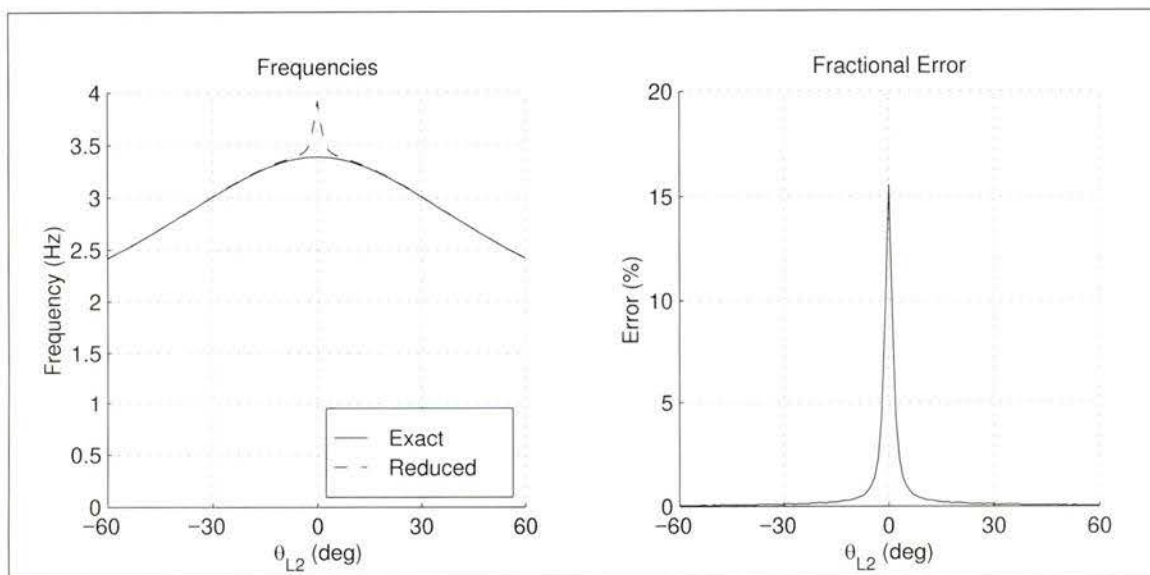


Figure C.5: Second Modal Frequencies for Exact and Reduced Systems with  $\theta_{S1} = \theta_{S2} = 0^\circ$  through a Range of  $\theta_{L2}$  Angles

# Vita

**Surname:** Van Vliet

**Given Names:** Christopher John

**Place of Birth:** St. Catharines, Ontario, Canada

## **Educational Institutions Attended:**

University of Alberta	1990 to 1995
University of Victoria	1995 to 1998

## **Degrees Awarded:**

B.Sc. Co-op (Distinction)	University of Alberta	1995
---------------------------	-----------------------	------

## **Honours and Awards:**

Canada Scholarship	1990 to 1995
Dean's Undergraduate Research Award	1995
Advanced Systems Institute Fellowship	1995
University of Victoria Fellowship	1995 to 1997

## **Publications:**

J. Stanway, J. Wright, J. Van Vliet, C. Damaren, M. Nahon, and I. Sharf. Dynamics Validation and Control with a Dual-Arm Flexible Manipulator Test-Bed. *Proceedings of the 9th CASI Conference on Astronautics*, 72-82, 1996


# Partial Copyright License

I hereby grant the right to lend my thesis to users of the University of Victoria Library, and to make single copies only for such users or in response to a request from the Library of any other university, or similar institution, on its behalf or for one of its users. I further agree that permission for extensive copying of this thesis for scholarly purposes may be granted by me or a member of the University designated by me. It is understood that copying or publication of this thesis for financial gain shall not be allowed without my written permission.

Title of Thesis:

Predicted and Observed Active Damping Performance  
of Macro-Micro Manipulators

Author

  
Christopher John Van Vliet  
February 5, 1997